NOVEL PARAMETRIC PROCESSES FOR QUANTUM INFORMATION PROCESSING USING RUBIDIUM VAPOR BASED PHOTONIC PLATFORMS

A Dissertation

Presented to the Faculty of the Graduate School

of Cornell University

in Partial Fulfillment of the Requirements for the Degree of

Doctor of Philosophy

by

Prathamesh Surendra Donvalkar

May 2017

NOVEL PARAMETRIC PROCESSES FOR QUANTUM INFORMATION PROCESSING USING RUBIDIUM VAPOR BASED PHOTONIC PLATFORMS

Prathamesh Surendra Donvalkar, Ph.D.

Cornell University 2017

Large Kerr nonlinearities are of significant interest for photonic quantum information processing and can be applied towards developing deterministic single photon sources and implementing deterministic quantum logic gates. The required strong nonlinear interaction between photons can be achieved by enhancing the light-matter interaction using alkali vapors interacting with a tightly confined optical mode area, such as that of a waveguide. The guiding properties of the waveguide over long distances helps in achieving a long interaction length while simultaneously increasing the atom-photon coupling by maintaining a small mode area over the entire guiding length. In this thesis, we explore the large effective Kerr nonlinearities (γ) of Rubidium vapor interacting with the optical mode of hollow-core photonic band-gap fibers (Rb-PBGF) and the tightly confined evanescent field of air-clad silicon nitride (Si_3N_4) waveguides (Rb-chip). We have demonstrated efficient and noiseless frequency conversion at low power levels leveraging the large γ for the Rb-PBGF system. As proof of principle, we have also generated spectrally bright quantum correlated photon-pairs in a warm Rb vapor-cell and have proposed an extension of the experiment in the Rb-PBGF platform, which could lead to near unit photon pair generation efficiency. During the course of the study, we have also significantly improved the Rb-PBGF system by attaining an almost continuous operation lasting for several hours (1000$\times$ longer) while generating optical

depths (OD's) ~ 50, which are required to attain single photon-level nonlinearity in the Rb-PBGF system. Developing on-chip CMOS [complimentary metal-oxide-semiconductor] compatible Rb vapor based platforms can not only achieve large γ, but also significantly reduce the footprint of the device and make it more compatible with other chip-based platforms. In our present work, we have demonstrated the feasibility of this approach by achieving extended interaction time-scales for, air-clad Si_3N_4 waveguides coated with aluminum oxide (Al_2O_3) and evanescently coupled to warm Rb vapor. The thin Al_2O_3 layer has greatly helped in preventing corrosive damage caused by Rb to the nitride surface that have improved the operational lifetimes by a factor > 100. During the course of our study, we realized the limitations of known platforms towards generating tunable sources of single photons at near-visible wavelengths; a wavelength regime at which great progress has been made for quantum storage and detection. Towards the end of this work, we have experimentally demonstrated a broadband frequency comb at near-visible wavelengths by engineering anomalous dispersion for higher order waveguide modes in Si_3N_4 microresonators. The underling process of parametric wave-mixing being the same for frequency combs and correlated photon-pair generation; our work opens new possibilities for developing spectrally narrow single photon sources in the near-visible which are compatible with highly nonlinear alkali vapor based systems like the Rb-PBGF and Rb-chip platform.

BIOGRAPHICAL SKETCH

Prathamesh Donvalkar was born on the 11^{th} of July 1988 in Mumbai, India. Since an early age, he developed an avid interest in aircrafts, with his father being involved in the civil aviation industry. Even today you can find him sketch doodles of commercial jets in his free time, with the Boeing-747 being his personal favorite. His interest in physics and mathematics peaked in the 8th grade when he was introduced to the concepts of energy and electricity, and he started imagining these principles at a microscopic level in everyday activities with his own rudimentary models. Upon going through the grind of the joint entrance exam, he joined the faculty of Engineering Physics at the Indian Institute of Technology, Bombay (IITB) in the fall of 2006. At IITB he was exposed to wide variety of courses across different subdivisions within physics and he developed a penchant towards "all things quantum." Through a string of excellent internship opportunities in leading European universities, he decided to continue his academic interests and pursue a PhD in Physics. Upon completion of his Bachelors and Masters program at IITB, he left his hometown and arrived in Ithaca, NY. Here he joined the quantum and nonlinear photonics group of Prof. Alexander Gaeta in the school of Applied and Engineering Physics at Cornell. He was awarded a Masters degree in the Fall of 2014 upon the successful completion of his thesis proposal. For the past five years, he has been pursuing research on novel parametric processes for quantum information processing as a part of his doctoral studies.

To my parents

ACKNOWLEDGEMENTS

I would firstly like to thank Prof. Alexander Gaeta for giving me an opportunity to work in his esteemed research group. Over the years, I have learnt a lot from Alex both academically and professionally and he has been a constant source of inspiration. I have deeply benefited from his astute understanding of the subject and his observations and suggestions have greatly influenced the way I tackle a research problem. Thank you for providing me with such a nice research group and being extremely kind and understanding during difficult times. I am also grateful to Prof. Robert Jarrow and Prof. Frank Wise for agreeing to be a part of my committee and for the insightful discussions we have had over the years. I really learnt a lot from the course on fixed income securities and my research has benefited a lot from the mathematical framework developed during the set of courses recommended by Prof. Jarrow. I am also indebted to Prof. Lois Pollack for helping me ease in to the process of being a Teaching Assistant upon my arrival in Ithaca. I really had a great experience TA'ing for the quantum mechanics course and teaching an enthusiastic batch of juniors at AEP. I would also like to thank Prof. Michal Lipson for the wonderful opportunity I had of engaging with her immensely talented group on several projects. I am grateful to Nate, Bob and Rodney for helping me utilize the machine shop facilities at AEP and build several useful components for all our experiments. I would also like to thank Donna, Renee, Cynthia, Bonni and Sherry at AEP for always being so helpful in every matter related to work or academics.

I am forever indebted to my lab mates for being a family away from home and the countless good times we have had in the past 5 years. I would firstly thank Vivek for being such a great mentor and teaching me all I know about the Rubidium system. Thanks for being so patient addressing my queries through the numerous

phone calls we have had even after you left for Boston. I would also like to thank Kasturi for helping me through all the initial experiments and familiarizing me with the different laser systems and optics. Stephane was instrumental in filling up the void after Vivek left, helping me troubleshoot experiments, one too many. I have learnt valuable lessons of being efficient and thinking out of the box, working with Stef. Thanks Stef for being critical about everything, which has helped me become a better scientist and for encouraging me to keep pushing the limits. I would like to thank Sven for teaching me to be extremely meticulous and methodical about conducting experiments as well as looking at the bigger picture. I dont think there has ever been a time when Sven did not have an answer to any of my experimental hurdles with quantum optics. I would also like to thank Alessandro and Chaitali for the wonderful discussions we have had on quantum optics and "Python." It was really a great experience working with you Chaitali and hope you continue to progress as a scientist. Yoshi, you have been a great support system over all these years mentoring me both professionally and on a personal level. I thank you and Ting for inviting me to your place for all important celebratory occasions, never making me feel homesick during the holidays. I would like to acknowledge and thank all my group members Chaitanya, Sam, Ryan, Henry, Moti, Alexander, Yun, Xiaohui, Gauri, Jared, Jae, Ara, Rees, Ian and Bonggu for the several insightful discussions we have had over the years and for making my stay lively. Avik, you have been a source of inspiration to me for all matters related to work or otherwise, with your continued zeal for excellence. Thanks for being such a gem of a person that you are and for all the wonderful discussions we have had. I would also like to thank Felippe and William for being such great co-workers. Felippe, thanks for the long discussion sessions we have had after you left and I have learnt a lot from you. William, you are the worlds greatest chip fabricator for me.

Outside the lab, I would begin by thanking my room-mate of four years, Rohit Garg. I have enjoyed all the debates and conversations we have had on history, politics, geology and ofcourse physics, to the extent of driving a third person in the room crazy. Had it not been for your chopping skills, I would have never managed to cook so regularly. I am also forever indebted to Garima for making me feel at home in Ithaca and for all the good times, the three of us have shared together. I have sincerely enjoyed all the philosophical discussions we have had over the years, which have also helped me become a better person. I would like to thank Prafull for being there in some of my most difficult times of need and for graciously showing me around upstate New York, upon newly arriving in Ithaca. Ritika and Chaitanya, thanks for hosting all the wonderful chai sessions and parties, and being one of my best friends in Ithaca. Sid, thanks for all the wonderful career advice and for being a mentor figure to me. I would also like to thank Aniket, Gauri, Tanay, Sachin, Pooja, Ajay, Kritika, Abhishek, Juju, Pankaj, Rahul and Ayush for being such lovely friends and making my stay in Ithaca memorable. I am deeply grateful to Air-India for sponsoring my numerous visits to India. The Maharaja is the "true emperor of the skies," period!

I would like to thank the entire Donvalkar family for helping me celebrate every little occasion back home, despite my absence and never letting me feel home-sick. A special thanks to my wonderful cousins Rohan, Manas, Rupali and her husband Pradnyesh. Paresh kaka, Mayura aatya, Agastya and Arnav; thanks for being my family in New York and welcoming me to your home. I am truly grateful to the entire Malankar family for having me over for all the wonderful weddings and thanksgiving parties, making my stay truly memorable in NY. Thanks Jon for being such a wonderful friend. I would also like to thank my best friend Abhishek, his lovely wife Khushboo (a special thanks for introducing me to Kadambari !), and

Anagha for all their support throughout these years. Abhishek you have practically seen all phases on my academic life, so thanks for sharing this wonderful journey and being someone I can depend on for anything. I would like to specially thank Kadambari for all the love and support you have extended and for being with me through thick and thin. Your constant motivation and immense patience have greatly influenced this dissertation. Thanks for making my time beautiful with your presence. All the lovely conversations both on an academic and philosophical level have kept me sane throughout my graduate studies, to which am forever indebted.

Beyond all, I would like to thank my parents, for without their motivation, love and guidance, none of this would have ever been possible. Thanks a lot Aai and Baba!

TABLE OF CONTENTS

LIST OF FIGURES

CHAPTER 1

INTRODUCTION

In the past two decades there has been an increasing focus on the development of quantum computing (QC) platforms [4, 6–15] with the ever rising demand on reducing the transistor size, which is reaching its practical limit [16]. QC not only offers an alternative route to high speed computing, but can also provide a test bed for running quantum simulations [17], which have no classical analogue. One of the biggest challenge in implementing a robust quantum computing device, has been to overcome the relatively short decoherence time-scales which hinder reliable operation [18]. Photons appear as a likely candidate to implement tools required for quantum information processing (e.g. teleportation), as they experience negligible decoherence compared to other quantum systems, even after propagating distances ranging over hundreds of kilometers [19–21]. There have also been some recent efforts to develop quantum resources operating on space based satellites [22, 23].

However, a major challenge of using photons for quantum computing is that, photons interact weakly with each other and hence a medium with a large non-linearity is required for observing measurable changes in the spectral features or polarization states of the interacting photons. Moreover, increasing the bandwidth of quantum information processing (QIP), requires the development of deterministic narrowband photon sources at any given desirable wavelength of operation. To date, the most efficient platforms for generating high fidelity single photons have had a single photon generation efficiency $\sim 10^{-8}$ photons/input photon [24]. Consequently, there has been an increasing focus on developing new platforms for QIP, facilitating single-photon level interaction with high efficiencies.

In our work, we focus on schemes using novel nonlinear optical processes such as Bragg-scattering four-wave mixing (BS-FWM) [chapter 2] and coherent photon conversion (CPC) [chapter (4)], which shall be useful in: (i) interfacing quantum devices, (ii) development of deterministic single photon sources and (iii) implementing deterministic quantum logic operations. Our approach relies on leveraging the large effective nonlinearities of alkali vapor interacting with optical modes in confined geometries which shall be crucial towards building a scalable platform for photonic QIP. In addition, we also explore the possibility of using on-chip silicon nitride (Si_3N_4) microresonators for developing tunable single photons sources which can be compatible with quantum systems like alkali-vapor in the near-visible wavelength range, by dispersion engineering of higher-order waveguide modes.

1.1 Large Kerr nonlinearity for photonic quantum information processing (QIP)

Developing, deterministic logic gates, high fidelity single photon sources and reliable quantum memories are the requirements for advances in optical quantum networks [25, 26]. This would entail performing nonlinear optics at the single photon-level. To date, significant advances has been made for demonstrating large single-photon nonlinearities by achieving a strong atom-cavity coupling [27–31] or by means of Rydberg atoms in cold atomic ensembles [32, 33].

An alternate approach towards attaining interaction with just a few photons in the optical mode would be to engineer platforms having large effective Kerr nonlinearity based on third-order nonlinear optical interaction $\chi^{(3)}$ [refer to appendix A for details] and operating at modest temperatures. The required strong

Kerr interaction can be achieved by: (i) coupling a strongly resonant system like an alkali vapor to a highly confined optical mode of a waveguide [3, 34–36], (ii) confining the light in resonant cavity [37–39] and (iii) giant Kerr nonlinearity via electromagnetically induced transparency [40].

Proposals have been made to implement a Fredkin gate [25] based on the idea that a single photon can impart a phase shift of π radians on another single photon, via a strong Kerr interaction. The Fredkin gate is similar in logic operation to the the universal c-NOT gate in classical computing and a recent demonstration of a $\sim$ 1 milliradian phase shift per photon achieved in a Rb-filled photonic band-gap (Rb-PBGF) system, have proved to be a crucial step towards attaining deterministic gate operation [41]. Measuring the phase shift imparted by a few photons on a classical beam can also serve as an important tool in making an indirect measurement of photon number without having the quantum state collapsed [42, 43]. This scheme, also known as a quantum non demolition measurement (QND), would require a large singe photon nonlinearity for making a realistic phase measurement at short averaging time intervals.

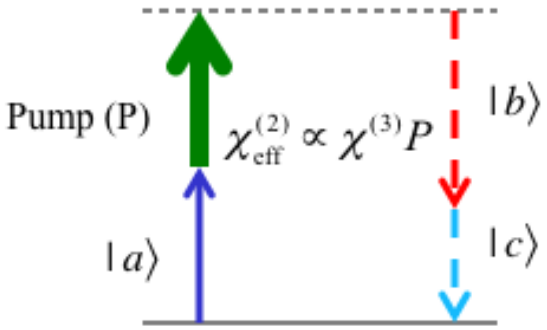

Figure 1.1: Four wave mixing between a strong pump P and three quantum modes $\hat{a}_a, \hat{a}_b$, and $\hat{a}_c$, in a $\chi^{(3)}$ medium, mimicing an effective second order process $\chi^{(2)}_{eff}$, such that $\chi^{(2)}_{eff} \propto \chi^{(3)} P$.

Large Kerr nonlinearity can also play a crucial role in the development of deterministic single photon sources using a recently proposed scheme for coherent photon conversion (CPC) [4]. The CPC process involves a classical pump beam and three quantum modes in a typical four-wave mixing interaction ($\chi^{(3)}$). For a highly nonlinear medium, the process mimics an effective second order nonlinear ($\chi^{(2)}_{eff}$) interaction between the three quantum modes (see Fig. 1.1). The scheme predicts that, if the effective Kerr interaction length of the medium can be made large enough, it would be possible to implement 100% photon doubling, develop a maximally entangling controlled phase gate, and generate high fidelity single photon sources, using the same platform (refer to section 4.2).

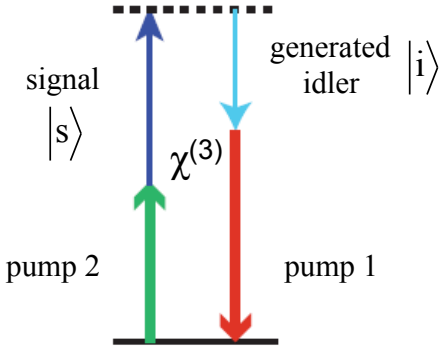

Figure 1.2: Bragg scattering four wave mixing interaction in which two strong pump beams (pump 1 and pump 2) noiselessly frequency translate a signal field $\hat{a}_s$ at frequency ω_s to an idler field $\hat{a}_i$ at frequency ω_i via a $\chi^{(3)}$ nonlinear process. The conversion efficiency depends on the effective Kerr nonlinearity, power of the pump beams and phase difference between the interacting modes.

Systems useful for photonic quantum information processing operate efficiently in different frequency regimes (e.g. the most efficient quantum memories implemented using atoms operate at visible wavelengths [44–47] whereas tunable and narrow-band single-photon sources are most easily implemented at telecom [38, 39, 48–51]). This makes efficient frequency conversion a vital step towards inter-connecting devices operating in different frequency regimes. Such efficient

and noise-less frequency conversion can be facilitated by the process of Bragg scattering four-wave mixing (BS-FWM) which relies on a nonlinear Kerr interaction between two pump fields and two quantum modes [52, 53] (see Fig. 1.2). If the strength of the nonlinearity is large, it is possible to achieve 100% frequency conversion between the two quantum modes. In addition to providing an interconnect between quantum devices, the frequency conversion facilitated by BS-FWM can provide a means to implement frequency qbits [54] which can be be used as a vital resource for QIP.

In this thesis, we demonstrate the use of Rb vapor interacting with confined optical modes, to yield large effective Kerr nonlinearities that can facilitate nonlinear optics at the single photon level. In particular we study Rubidium (Rb) vapor confined to hollow-core photonic band-gap fibers (Rb-PBGF) and Rb vapor evanescently coupled to the optical mode of air-clad Si_3N_4 waveguides. Furthermore, we have also explored the possibility of using dispersion engineered Si_3N_4 microresonators, for achieving broadband parametric wave mixing at near visible wavelengths. Our demonstration of a broadband frequency comb, opens interesting new possibilities towards developing tunable single photon sources in the near-visible which can also be compatible with our highly nonlinear Rb-PBGF or Rb-chip platform.

1.2 Resonantly enhanced Kerr nonlinearities in alkali vapor

Since the development of the laser in the early 1960's [55], alkali vapors have been used to demonstrate strong coherent nonlinear interactions due to their: (i) large

scattering cross sections, (ii) well defined energy levels and (iii) the possibility of attaining large atomic densities at moderate temperatures; a parameter measured by the optical depth (OD). Attaining large single photon-level nonlinearities would require maximizing the atom-photon interaction given by $g\sqrt{(OD)}/\Gamma$, where Γ is the lifetime of the excited state and g is the atom-photon coupling constant. The scattering cross-section A_{sc} for an alkali atom is given by $A_{sc} = 3\lambda^2/2\pi$, where λ is the wavelength at resonance. The coupling constant $g \sim 1$, when the optical mode area A approaches A_{sc}, and hence a system with a dense alkali vapor confined to tiny geometries are a natural choice for attaining strong light matter interactions. This can be further explained by discussing the requirements for a large Kerr interaction. For an alkali vapor, we can write the strength of the effective Kerr nonlinearity γ as [56],

$$\gamma \propto \chi^{(3)} \frac{L}{A} \tag{1.1}$$

and for a two-level system, the above expression can be further simplified to,

$$\gamma \propto N \frac{1}{\Delta^3} \frac{L}{A} \tag{1.2}$$

where, N is the atomic number density, L is length of the medium, A is the optical mode area and $\Delta = \omega - \omega_0$ is the detuning of the laser field ω from the atomic transition frequency ω_0. Thus, smaller the detuning of the laser field from the atomic transition, larger will be the strength of the nonlinearity. This phenomenon is also known as the resonant enhancement of Kerr nonlinearity. In principle, the detuning cannot be made arbitrarily small as the laser field starts experiencing strong linear absorption close to resonance and at high atomic densities. Practical values of detunings are always chosen such that the two opposing effects (resonant enhancement and linear absorption) balance each other.

As seen in equation 1.2, γ can also be enhanced by improving the L/A ratio. A

simple approach for decreasing the optical mode cross-section, is to tightly focus the input laser field in a bulk vapor cell. However, a tightly focused beam also has a smaller confocal parameter; which is a measure of the effective interaction length. For example, focusing a beam at $\lambda = 780$ nm (the D_2 transition of Rb) to a spot size 2.5 μm in radius (w_0), leads to a confocal parameter of $\sim 2\pi {w_0}^2/\lambda = 50$ μm. Alternatively, the L/A ratio can be increased by having the alkali vapor interact with the confined optical modes of waveguides. One possible solution is to have an optical mode interaction with atoms confined to the core of hollow-core PBGF's. The practical implementation of such a system has been described in previous works [3, 41, 57], which demonstrate a dense alkali vapor existing upto a depth of ~ 1 cm in a PBGF with a fundamental mode field area ~ 10 μm^2. The Rb-PBGF system achieves a 200$\times$ improvement in the L/A ratio over the bulk vapor cell with everything else constant.

Similarly, the Si_3N_4 waveguides designed for achieving an evanescent field interaction with Rb vapor (chapter 5), have the optical mode confined in a narrow cross-section, 50 nm away from the waveguide surface. The device dimensions are designed to engineer $\sim 6\%$ of the guided mode in the evanescent region, for a 200 nm tall, 600 nm wide and 1 mm long waveguide. The tight confinement of the evanescent mode could lead to an enhancement by a factor > 600 in the L/A ratio, over those in bulk vapor cells. In the next sections, we shall describe in detail, the methods to build a practical Rb-PBGF and a Rb-chip system.

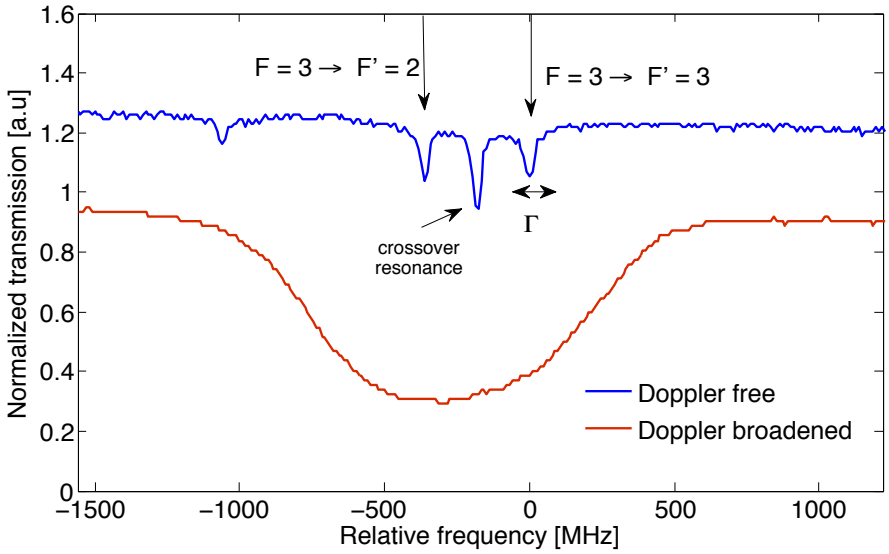

Figure 1.3: Plot of probe transmission versus relative frequency, in a Doppler free setup (blue) [saturation absorption spectroscopy (section 1.3)] and bulk vapor cell (red) to compare the natural linewidth Γ with the Doppler broadened spectrum. The probe frequency is scanned across the $5P_{1/2}, F = 3 \rightarrow 5P_{1/2}, F' = 2, 3$ transition of ^{85}Rb.

1.3 Rubidium

The choice of Rb in our experiments stems from a variety of reasons. Rb is quite readily available and there is extensive literature explaining in great detail, the energy level system and transition strengths for Rb in the vapor form. Secondly, the technology to handle an extremely reactive element like Rb is also quite well established. Rb is the most common element used in cold-atom experiments and hence, highly stable CW lasers are easily available near its ground state transitions (780 nm and 795 nm). Rb can also form a dense vapor (atomic density $> 10^{18}$ atoms/m^3) at modest temperatures which can yield a large value of γ for warm vapors (i.e. T $< 80°$C).

Rb is an alkali element, and lies below Potassium in the periodic table. Commercially, Rb is most commonly available as an isotopic mixture of ^{85}Rb and ^{87}Rb

in the ratio of 7:3. Its ground state is split into two hyperfine sub-levels labeled as $5S_{1/2}$, F = 3 and $5S_{1/2}$, F = 2, which have an energy separation of 3.035 GHz. The ground state is connected to its first excited state at $5P_{1/2}$, F' = 2,3 and $5P_{3/2}$, F' = 1,2,3,4 with transition wavelengths at 795 nm (D_1) and 780 nm (D_2) respectively [58]. These two transitions are used in almost all experiments described in this thesis. An electron in the excited state i.e. $5P_{1/2}$ or $5P_{3/2}$, decays at a rate $\sim 38 \times 10^6$ s^{-1}, which corresponds to a natural line width of $\Gamma \sim 6$ MHz for each transition. In principle, a probe beam propagating through a warm Rb vapor experiences absorption close to the transition wavelength of the atoms. However, if we scan the frequency of the laser across an individual transition, the overall absorption linewidth is much broader than the natural linewidth of the transition. This broadening of transition linewidths can be explained by considering the motion of atoms in a warm atomic ensemble. Atoms moving with a given velocity 'v', experience a Doppler shift in frequency of the incoming photon, due to which different species of atoms in the warm ensemble have a velocity dependent transition frequency. For a warm vapor, the atoms have a velocity distribution given by the well known Maxwell's relation,

$$f(v) = \frac{1}{\sqrt{\pi} v_d} exp(-\frac{v^2}{{v_d}^2}) \tag{1.3}$$

where, $\sqrt{2}v_d$ is the width of the velocity distribution. Individual atomic transitions hence appear broadened due to the Gaussian distribution of the transition frequencies for atoms with different velocities. This is illustrated in Fig. 1.3, where we plot the transmission of a probe beam through a Doppler free saturation absorption spectroscopy setup (blue) [59] and through an isotopically pure bulk ^{85}Rb vapor cell (red). The laser beam is scanned across the $5S_{1/2}, F = 3 \rightarrow 5P_{1/2}, F' = 2, 3$ transition of ^{85}Rb. The Doppler free spectrum reveals the natural linewdith (Γ) of the transition, which is obtained from a counter propagating pump-probe scheme and

is significantly narrower than the Doppler broadened spectrum of a probe in the absence of a pump beam. The pump beam saturates the absorption by transferring population to the excited state, to point that there can be no further excitation at the pump frequency. This spectral region of saturated absorption overlaps with the counter propagating probe beam only for atoms with close to zero velocity. The probe beam experiences no absorption in this narrow transparency window (also coinciding with the natural width of the transition) created by the saturation effect. In practice, the probe is always maintained optimally detuned off the Doppler broadened transition, such that a balance is achieved between resonant enhancement of nonlinearity and linear absorption [60].

1.4 Hollow-core PBGF

The idea of a guiding light in a hollow-core PBGF was introduced in the early 1990's, with the first demonstration of single mode guiding in a silica-air hole PBGF [2]. This has opened up an altogether new dimension in engineering systems with large nonlinearities by introducing, molecules [61–65], atoms at room temperature [3,41,47,66,67], and cold atoms [68,69] in the air-core of PBGF's. As compared to regular solid-core fibers which guide light by the principle of total internal reflection [Fig. 1.4(b)], the guiding of light in a PBGF is through Bragg diffraction which had been proposed in the mid 1970's [70]. When light propagates in a periodic medium like a photonic crystal structure, the transmission properties of light are analogous to that of an electron in a periodic potential well. Light propagates through the periodic lattice at certain allowed wavelengths and is reflected back at a series of forbidden wavelengths (photonic band-gap), both of which are determined by the material refractive indices and periodicity of the lattice. If a defect is introduced

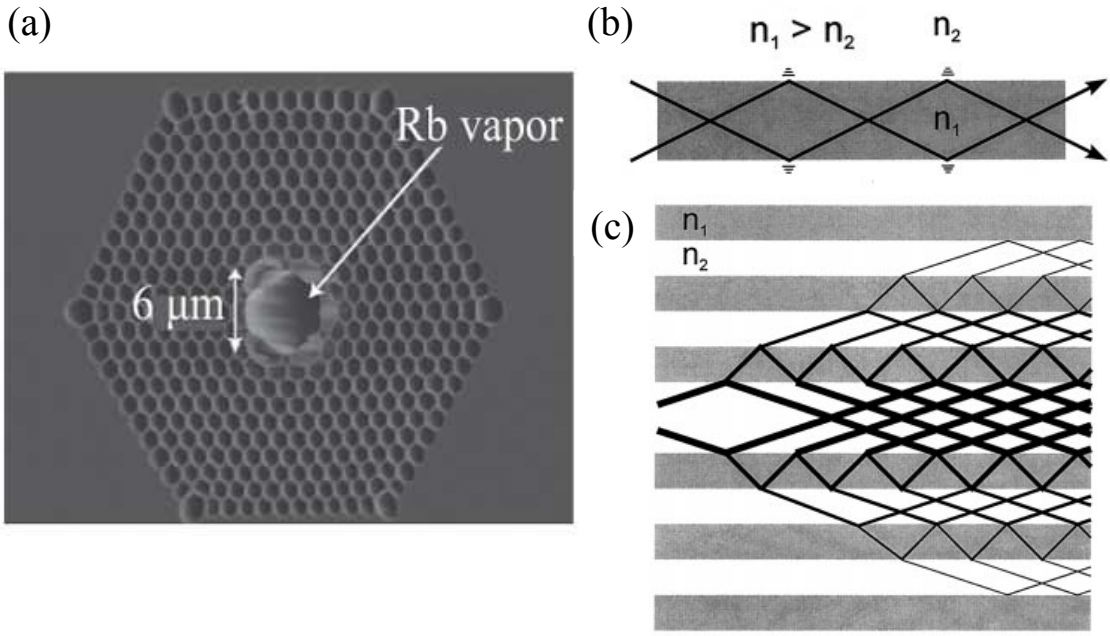

Figure 1.4: (a) Cross section of the 6 μm core diameter PBGF used in our experiments (NKT Photonics AIR 6-800) [1]. The arrows indicates the fiber core where the Rb vapor is present. (b) Guiding of light in a regular solid core fiber by the principle of total internal reflection. (c) Guiding of light in an air-core PBGF, by the principle of Bragg reflection [2].

in the periodic structure, the transmission of light in the defect mode have allowed solutions in the band-gap of the surrounding periodic photonic crystal. This means that, any light originating or coupled into the 'transmission allowed wavelengths' of the defect state will experience reflection from the surrounding periodic structure, and will be confined to the defect region. As seen in Fig. 1.4(a), the air hole in the centre of the periodic lattice acts like a defect state, and hence light coupled into the air hole is guided by the principle of Bragg-reflection from the surrounding periodic lattice structure. The guiding of light confined to the air-core is shown in Fig. 1.4(c). In our experiments, we use a hollow core PBGF, from NKT photonics (AIR 6-800) [1] with a 6 μm core diameter. The fiber has a photonic band gap (PBG) in the wavelength range of 740 nm - 800 nm [See Fig. 1.5]. This wavelength range for the PBG, enables guiding of light (in the core) at the ^{85}Rb ground state

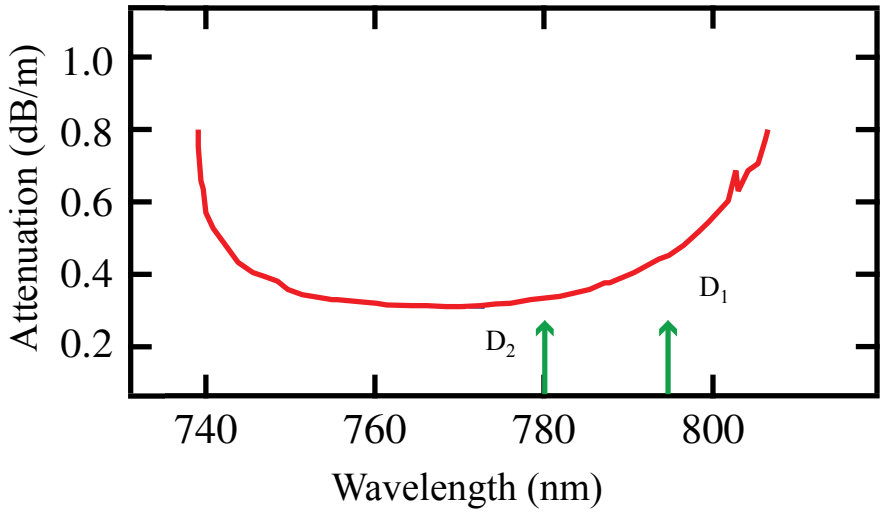

Figure 1.5: Transmission curve of the hollow-core photonic crystal fiber (NKT Photonics AIR 6-800) used in the Rb-PBGF system. Arrows in green indicate high transmission of the PBGF at the D_1 and D_2 lines of Rb [1].

transitions of D_1 (795 nm) and D_2 (780 nm), as well as the excited states transitions at 776 nm and 762 nm, that have been widely used in our present work. Marginal guiding losses for the PBGF over a length scale of a few meters, and a fundamental mode area $\sim 20\ \mu m^2$, make it an excellent choice to achieve resonantly enhanced large Kerr nonlinearity by introducing the Rb vapor in the core.

1.5 Air-clad Si_3N_4 waveguides

To date, traditional systems employing Rb as a source for achieving large nonlinearities (warm ensembles and cold atoms) have been quite large in size, and engineering on-chip waveguide modes evanescently coupling to Rb vapor would significantly reduce the foot-print of the setup. Building a Rb on-chip source with a large nonlinearity would demand the evanescent optical mode to be tightly confined in a narrow cross-section, which would enhance the L/A ratio [refer equation

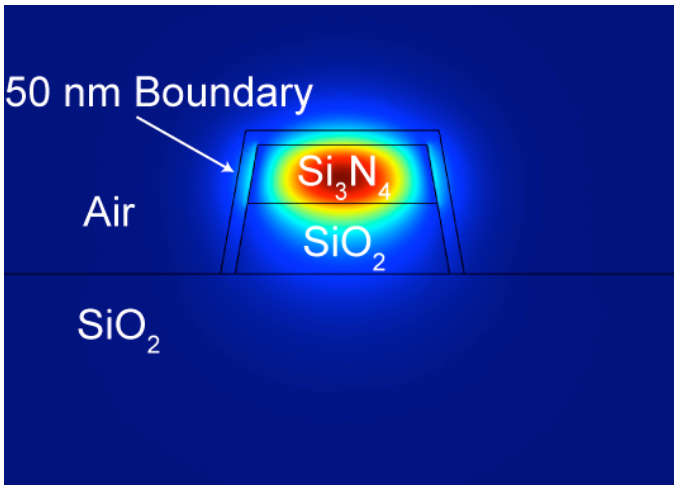

Figure 1.6: Viewgraph showing the simulated cross-sectional of an air-clad Si_3N_4 waveguide used in the Rb-chip system. COMSOL simulation for the TM mode reveals an evanescent mode extending from the waveguide surface, with around 6% of the total guided field in the evanescent region.

1.2]. Secondly, it is extremely challenging to build a high finesse cavity around Rb vapor at moderate temperatures due to the corrosive nature of the alkali, which reacts violently with the reflective coating of cavity mirrors and makes it extremely difficult to attain a strong coupling between the vapor and the cavity. Evanescent coupling of Rb vapor to high-Q air-clad Si_3N_4 microresonators could prove to be a game changer in the field of cavity quantum electrodynamics (QED) and could also potentially replace the bulkier systems implemented using cold atomic ensembles.

Si_3N_4 is one of the most promising platforms for quantum and nonlinear photonics. Recent advances in fabrication technology for CMOS compatible Si_3N_4 devices, have made it possible to obtain large quality factors (Q value) $\sim$ 37 Million for on chip Si_3N_4 based microresonators [71]. As seen in Fig. 1.6, engineering the waveguide dimensions appropriately for an air-clad device (details in chapter 5), makes it possible to have a significant fraction of the guided mode outside the waveguide (evanescent field), and previous demonstrations have shown evidence of interaction between Rb and the evanescent mode of a Si_3N_4 waveguide [5, 72, 73].

Recently, weak atom-cavity coupling has also been reported using a Si_3N_4 microresonator and warm Rb vapor [74, 75], where the coupling efficiency was largely limited due to the low Q values of the reported devices.

The waveguides and microresonators used in this work are 200 nm tall and 600 nm wide, with the microresonators designed for a cavity mode spacing of 200 GHz and have a measured Q $\sim$ 100,000. About 6% of the TM waveguide mode exists as an evanescent field in narrow cross-section, 50 nm away from the surface of the waveguide (see Fig. 1.6). We select a region of interaction slightly off the waveguide surface, to avoid dephasing of the Rb atoms. Interaction of the tightly confined mode with Rb and the high Q values of the microresonator, can greatly enhance the effective Kerr nonlinearity. The waveguides also have a high transmission for wavelengths around the D_1 and D_2 lines of Rb. All devices discussed in this thesis are coated with a thin layer of aluminum oxide (Al_2O_3) for preventing corrosive reaction between Si_3N_4 and Rb at elevated temperatures. In the next section we describe the experimental implementation of Rb-PBGF and the Rb-chip system.

1.6 Vacuum chamber design for the Rb-PBGF and Rb-chip system

Rb being a highly reactive element, requires ultra-high vacuum (UHV) to be released and maintained in the vapor form. The UHV minimizes the interaction of Rb with impurities like water molecules and oxygen which helps in the build up of high vapor densities in a relatively short time frame. It also prevents an undesirable chemical reaction of Rb with any impurity on the surface of the PBGF/chip, which could cause a permanent damage to their guiding properties. A detailed de-

scription of the chamber building procedure and evolution of chamber design used in Rb-PBGF experiments have been elucidated in previous works [76, 77]. The method for building and maintaining a chamber for the Rb-PBGF or a Rb-chip system is exactly the same, except for differences in chamber design. The chamber for the Rb-PBGF system used in the present body of work (see Fig. 1.7) is built on the same lines as the ones that have been previously used in demonstrations of cross-phase modulation [41] and two-photon absorption [57, 60]. We splice a

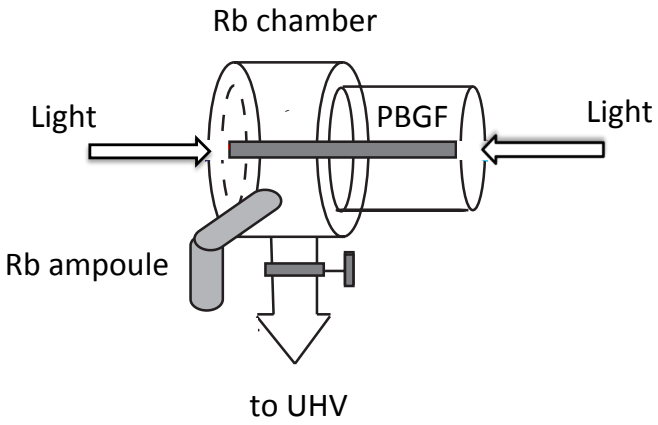

Figure 1.7: A 9-cm long hollow core PBGF with guiding wavelengths in the range of 740 - 800 nm, is mounted on a metallic holder. A Rb ampoule is inserted in a flexible hose attached to the chamber which can be cracked open when the requisite UHV is attained. Light is coupled in and out of the PBGF via sapphire viewports attached on both sides of the chamber. Once the ampoule is cracked, the Rb atoms are released and they diffuse into the core of the PBGF forming metal nanoclusters. A CW vapor generating beam is required to thermally vaporize the clusters and attain the high OD's required for a large γ.

9-cm long PBGF and mount it on a metal holder (length = 8.5 cm). The holder is designed to be only slightly shorter than the PBGF, for minimizing the length of fiber floating outside the holder, which considerably reduces the effect of mechanical vibrations on the coupling. The fibers are glued on to the holder using a vacuum adhesive. We attach sapphire viewports on either sides of the chamber to couple light in and out of the PBGF, as sapphire is resistant to Rb at high temper-

atures. A Rb ampoule is inserted in a small flexible hose attached to the chamber, which allows the ampoule to be cracked open when then the requisite UHV has been attained. In contrast to the fixed chamber design for the Rb-PBGF system, the chamber used for the Rb-chip system allows for 3D rotation and z-translation [see Fig. 1.8], to primarily over-come the unavailability of UHV components that can guarantee a chamber length of 1.5 mm. This is because, the width of the chips available from fabrication is about 1 mm. To reduce the length of free space between the viewports and the chip, a very narrow chamber is required. This narrow chamber design makes it convenient to distinguish between the effect of Rb on the probe beam coupled into the waveguide, versus when it travels in the free space between the chip and both the viewports. We utilize custom-made viewports, with the sapphire windows protruding from a standard conflat (CF) flange such that they form a narrow space of 1.5 mm between them when attached together [see Fig 1.8]. The overall thickness of the CF flange is about 2.5 cm and hence we use high NA long working distance (3-cm) multi-element objectives for coupling light into an inverse-taper with an optical mode 3-μm in diameter. As we have no-precise control over the orientation of chips when they are glued on the copper rod and the precise angle of the chamber when it is mounted, any tiny deviations from the horizontal plane could lead to a large beam displacement at a distance of 3 cm away from the taper for such a confined optical mode. This would risk clipping the beam (beyond the range of optimization via beam walking) and would prevent efficient coupling into the waveguide mode. The 3D rotation allows for a precise horizontal alignment and the z-translation makes it convenient to couple in the waveguide without having to horizontally translate the beam. The rotation and translational degrees of freedom are facilitated by connecting the chamber to the UHV assembly by means of a flexible hose. As see in Fig. 1.8, the chips are

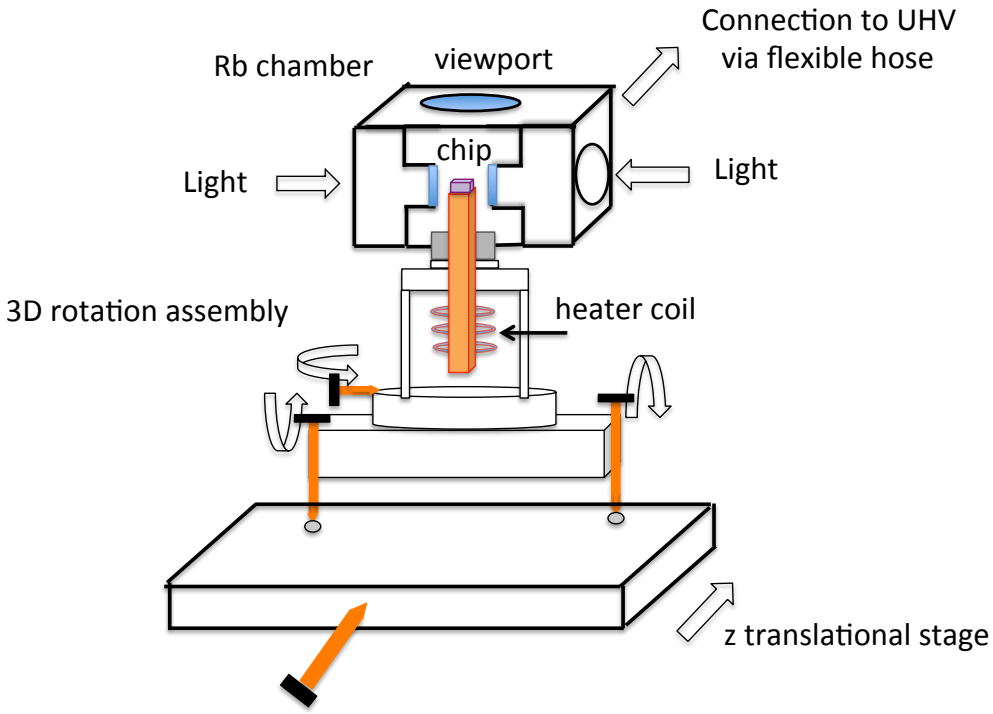

Figure 1.8: Air-clad Si_3N_4 waveguides and microresonators mounted on a copper rod are placed between a thin spacing measuring 1.5 mm between two sapphire viewports. In addition there is a viewport on top of the chamber to image the chip. A Rb ampoule is inserted in a flexible hose attached to the chamber. The copper rod holding the chips is thermally insulated from the chamber, and hence the temperature of the waveguides can be controlled independent of the chamber temperature. The entire chamber is mounted on a 3D rotation assembly to orient the chips in the horizontal plane. In addition, the chamber can also be translated horizontally, which helps in coupling light into the waveguides, without beam steering.

mounted on a copper rod using vacuum glue in the 1.5 mm long space between the sapphire viewports. We also attach a viewport at the top of the chamber to image the chips. The copper rod is mounted on an insulated CF flange which allows for an independent temperature control of the rod (and hence of the chips) from that of the surrounding chamber. The rod is heated using a resistive heater coil; the current through which is stabilized using a proportional-integral-derivative (PID) controller. Independent temperature control of the waveguides shall also allow for tuning the available fixed lasers (mode-hop free tuning range <10 GHz) into

the ring-cavity modes (separated by 200 GHz). As in the case of a chamber for the Rb-PBGF system, we insert a Rb ampoule in a flexible hose attached to the chamber.

A serial assembly of a roughing pump, a turbo pump and an ion pump is used to create the required UHV for both the Rb-PBGF/chip chamber. The roughing pump creates a baseline pressure of $\sim 10^{-3}$ Torr, which is required to operate the turbo-pump. Without this baseline pressure, the thin blades of the turbo pump will be damaged due to intense heat created by friction between air and the blades at high rotational speeds. The turbo pump, further evacuates the chamber to attain pressure $\sim 10^{-8}$ Torr which is finally reduced to $< 10^{-9}$ Torr using the ion pump and by baking the chamber at 150°C for over 3 weeks. Once the required UHV has been attained, the chamber is cooled down to room temperature and the Rb ampoule is cracked open by bending the flexible hose. Thereafter, we maintain the chamber at moderate temperatures of 50°C. Over a period of 1-2 weeks, the Rb atoms initially react with any available oxygen and water molecule or an OH bond adsorbed on the chamber surface and passivates it. Once this initial reaction is complete, the density of the Rb atoms builds up inside the chamber, during which the atoms slowly diffuse inside the core of the PBGF or are available for evanescently interacting with the waveguide mode. The density of Rb-atoms inside the chamber can be set to any desired level by maintaining the ampoule and chamber at a precise temperature, using heater coils regulated by PID controllers. In case for a Rb-PBGF system, the atomic density inside the core builds up over a period of 2-3 weeks after cracking the ampoule, in the form of metallic nano-clusters. A dense Rb vapor is required inside the PBGF core for attaining large effective Kerr nonlinearities. This dense vapor is achieved using a vapor-generation procedure facilitated by a high CW power laser beam which is maintained far off

resonant from any Rb-transition (805 nm). The details of the vapor generation process are discussed in chapter 3, where we also demonstrate a large improvement in the timescale of operation for the Rb-PBGF system.

1.7 Thesis layout

In this thesis, we describe experiments performed in the Rb-PBGF system and Rb vapor cell, facilitating frequency conversion at low powers and a high CPC pair generation efficiency. We also explore the potential of using the Rb-chip platform for large single-photon level nonlinearity. In chapter 2, we demonstrate efficient and noiseless signal to idler frequency conversion via Bragg scattering four-wave mixing at low pump powers $\sim$ 100 uW.

Optical depths lasting for just a few seconds have been a long standing limitation of the Rb-PBGF system and in chapter 3 we demonstrate optical depths lasting for more than an hour, using vapor generation beams with significantly high CW power-levels and a wavelength close to the photonic band edge of the PBGF. Chapter 4 describes the realization of CPC in a Rb-vapor cell, where we generate a pair of photons from a weak input field (200 nW) with a CPC pair generation efficiency exceeding 10 times of the previous demonstration in photonic crystal fiber [4]. We also explain an extension of this experiment in the Rb-PBGF system to obtain near-unit CPC pair generation efficiency, leveraging the large γ of the Rb-PBGF system.

In chapter 5, we discuss improvements in device fabrication and experimentally demonstrate the feasibility of using Rb-vapor evanescently coupled to Si_3N_4 waveguides at high vapor densities. We report quality factors $\sim 100,000$ for air-

clad Si_3N_4 microresonators which could further enhance the nonlinearity by several orders in magnitude and lead to a strong photon-photon interaction. In chapter 6, we demonstrate a new method for achieving broadband anomalous dispersion in the near-visible regime by employing higher-order waveguide modes. This technique could prove extremely useful in the development of narrow band tunable photon sources and sources of squeezed light in the near-visible wavelength regime. Finally in chapter 7, we discuss future experiments that can be performed using the Rb-PBGF and Rb-chip system.

CHAPTER 2

FREQUENCY TRANSLATION VIA BRAGG SCATTERING FOUR-WAVE MIXING IN RB FILLED PHOTONIC BAND-GAP FIBERS

In this chapter we demonstrate for the first time, frequency translation in warm Rb vapor confined to a hollow-core photonic band-gap fiber, using Bragg scattering - four-wave mixing (BS-FWM). We employ a diamond level scheme on the $5S_{1/2} \rightarrow 5D_{3/2}$ two-photon transition in ^{85}Rb for the BS-FWM process. In the presence of pump beams at 780 nm and 795 nm, a weak signal beam at 776 nm is translated to a wavelength of 762 nm, with pump powers as low as 300 μW and a 21% conversion efficiency.

2.1 Nonlinear frequency conversion

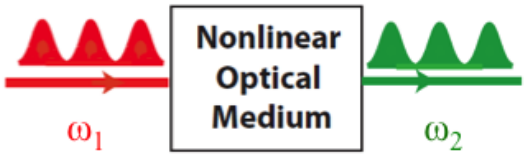

Figure 2.1: Frequency conversion of an input light field at frequency ω_1 to a frequency ω_2 in a nonlinear medium.

Noise-free frequency translation of optical fields [78] has potential applications in quantum information processing [4,79], quantum memories [46,80,81], and high-speed signal processing. Efficient frequency conversion of light can be facilitated by photon-photon interaction in a highly nonlinear medium. For e.g. (see Fig. 2.1), when an input light field at frequency ω_1 enters a nonlinear medium, it exits the medium at a different frequency ω_2. The extent of frequency conversion depends on

the strength of the the nonlinear interaction. In the past, several different nonlinear processes have been employed to demonstrate frequency translation. Frequency conversion can be achieved by the process of Raman scattering [82], where an input photon can be converted into a photon at a higher(lower) frequency by scattering-off the vibrational states of atoms or molecules. The frequency converted photon is also called the Anti-Stokes(Stokes) photon. Secondly, one can have frequency conversion by scattering an incoming photon from an acoustic phonon; a process which is know as Brillouin scattering [83]. Frequency translation has also been demonstrated using a second-order nonlinear optical process ($\chi^{(2)}$) [78], where a weak beam can interact with a strong pump, creating a photon at a frequency which equals the sum(difference) of the input photons.

In our work, we study frequency conversion using BS-FWM, which is a third-order nonlinear process ($\chi^{(3)}$) and is explained in detail in the next section.

2.2 Bragg scattering four-wave mixing

BS-FWM is a promising way to manipulate the frequency of photonic quantum states without adding noise [52, 53]. In this process, two strong pump beams detuned in frequency by $\Delta\omega$ interact with a weak field, and the weak field is then translated in frequency by $\Delta\omega$. The term Bragg scattering is used, to draw an analogy with conventional frequency conversion using a Bragg grating or from periodic planes of solid. We can think of the pump beams to create a periodic modulation of the refractive index due to interference and the weak input photon scatters of this periodic modulation to a photon at a different frequency. In the absence of any losses, the quantum mechanical description for the interaction Hamiltonian [52] of

such a FWM process in the limit of classical pump beams [power(field amplitude) $P_1(A_1)$ and $P_2(A_2)$ for the two pump beams] is,

$$\hat{H} = \delta k(\hat{a}_s^\dagger \hat{a}_s - \hat{a}_i^\dagger \hat{a}_i) + \kappa \hat{a}_s^\dagger \hat{a}_i + \kappa^* \hat{a}_s \hat{a}_i^\dagger, \tag{2.1}$$

where, $\hat{a}_s^\dagger(\hat{a}_i^\dagger)$ and $\hat{a}_s(\hat{a}_i)$ represent the creation and annihilation operators of the signal(idler) photons respectively. For co-polarized, pump, signal and idler beams, the coupling strength $\kappa = 2\gamma A_1 {A_2}^*$, where γ is the strength of the effective $\chi^{(3)}$ nonlinearity. δk represents the total phase mismatch term by taking into account both linear and nonlinear phase matching conditions and is given by $\delta k = k_2 + k_s - k_1 - k_i + \gamma(P_1 - P_2)/2$, where k_j, $j = 1, 2, s, i$ are the propagation vectors for the pumps, signal and idler beams respectively. In the Heisenberg's picture we additionally have,

$$d_z \hat{a}_j = i[\hat{a}_j, \hat{H}], \tag{2.2}$$

where $d_z = d/dz$ and j = s,i. Combining equations 2.1 and 2.2, we get

$$d_z \hat{a}_s = i\delta k \hat{a}_s + i\kappa \hat{a}_i, \tag{2.3}$$

$$d_z \hat{a}_i = i\kappa^* \hat{a}_s - i\delta k \hat{a}_i \tag{2.4}$$

Solving equations 2.3 and 2.4 with the initial condition $\hat{a}_i(0) = 0$, the field operators evolve as,

$$\hat{a}_s(z) = \cos(kz)\hat{a}_s(0), \tag{2.5}$$

and

$$\hat{a}_i(z) = -i\kappa \frac{\sin(kz)}{k} \hat{a}_s(0) \tag{2.6}$$

where the wavenumber $k = (|\kappa|^2 + |\delta k|^2)$. In the limit of perfect phase matching ($\delta k = 0$), we get

$$\hat{a}_i(z) = -i\sin(\kappa z)\hat{a}_s(0) \tag{2.7}$$

Let the input state be given by $|s,i\rangle = |1,0\rangle$. By realizing $\hat{a}_i(z)^\dagger|0,0\rangle_{out} = |0,1\rangle_{out}$ and $\hat{a}_s(0)^\dagger|0,0\rangle_{input} = |1,0\rangle_{input}$, equation 2.7 results in, $|0,1\rangle_{out} = i\sin(\kappa z)|1,0\rangle_{input}$. This indicates that the number of photons in the idler beam $n_i(z) = {}_{input}\langle 1,0|\hat{a}_i(z)^\dagger\hat{a}_i(z)|1,0\rangle_{input}$ evolves as, $n_i(z) = \sin^2(\kappa z)n_s(0)$. For a medium with a large γ, we can achieve $\kappa z = \pi/2$ by varying the interaction length 'z', which implies that a signal photon can be completely converted to an idler photon. Similarly, $\kappa z = \pi$ indicates that the generated idler photon converts back into a signal photon and hence the process is coherent. The intrinsic nonlinearity of optical media such as microstructured fibers and highly nonlinear fibers is relatively low. Frequency translation over a few hundred nanometers by BS-FWM in silica optical fibers has been reported previously with peak pump powers ranging from a few hundred milliwatts [84] to a few watts [85,86], and the fiber lengths used in these experiments range from a few meters [85,87], to a kilometer [84,86]. An alternative approach to achieving low-power frequency conversion is to use Rb atoms confined to hollow-core photonic band-gap fibers (PBGF's). Such a system offers very high effective third-order nonlinearities with an interaction length of a few centimeters [57,60,88,89]. Thus, frequency translation using pump powers several orders lower in magnitude than previously demonstrated is possible with fibers that are only a few centimeters long. As a result, the latency of this scheme is typically 1 ns while that of silica fiber based BS-FWM is in the microsecond regime.

2.3 Diamond level-scheme in ^{85}Rb

Figure 2.2 shows the ^{85}Rb level scheme used in the experiment. We employ the $5S_{1/2} \rightarrow 5D_{3/2}$ two-photon transition in ^{85}Rb for our FWM interaction. Similar

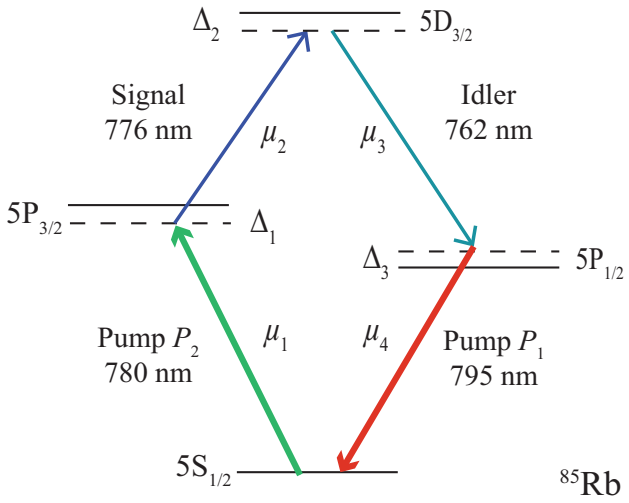

Figure 2.2: ^{85}Rb level scheme used in the experiment. Pump beams at 780 nm and 795 nm are tuned to the D_2 and D_1 lines of ^{85}Rb, respectively. A signal beam at 776 nm is frequency translated to the idler at 762 nm.

diamond like schemes with four distinct atomic transitions have been reported earlier to perform FWM in warm Rb vapor [90–92]. The continuous-wave pump beams P_1 and P_2 are tuned to the D_1 ($5S_{1/2} \rightarrow 5P_{1/2}$) and D_2 ($5S_{1/2} \rightarrow 5P_{3/2}$) lines of ^{85}Rb, respectively. A weak signal beam tuned near the $5P_{3/2} \rightarrow 5D_{3/2}$ transition at 776 nm is translated to a wavelength of 762 nm, corresponding to the $5D_{3/2} \rightarrow 5P_{1/2}$ transition. It may be thought that a second FWM process might occur in which two pump photons at 780 nm and 795 nm are annihilated to create two photons at 762 nm and 814 nm. However the detuning of these wavelengths from the resonant transitions is in the THz regime, and hence the effective nonlinearity of this process is $\sim$ 6 orders of magnitude lower than that of the BS-FWM studied here. Henceforth, we shall refer to the beam at 776 nm as the signal beam while the frequency translated beam at 762 nm as the idler.

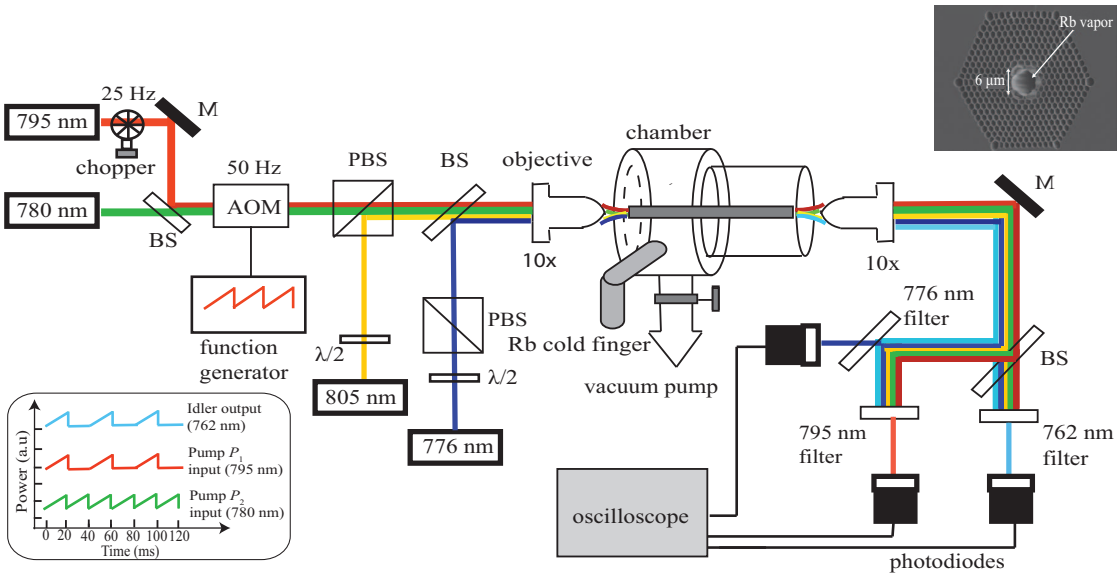

Figure 2.3: Pump beams P_1, P_2 and the signal are coupled into the PBGF in addition to the mW-level vapor-generating beam at 805 nm. Both P_1 and P_2 are modulated using an AOM, set to a sawtooth waveform at 50 Hz. P_1 is also modulated by a chopper at 25 Hz. As seen in the inset, the idler is generated only in the presence of both pump beams and the signal. The generated idler along with all other beams are separated using band-pass filters. The signal, idler, and pump P_1 are then monitored on the oscilloscope.

2.4 Experimental setup

We use a Rb cell containing a PBGF as previously described in section 1.6. The pump and signal beams are sent copropagating into the PBGF as shown in Fig. 2.3 using a 10X objective. The cross section of the fiber is shown in the inset of Fig. 2.3. Rb clusters that form on the inner core walls of the fiber are vaporized using a desorption beam at 805 nm resulting in an optical density (OD) $\sim$ 100. Beams at 780 nm, 795 nm, and 776 nm obtained using external cavity diode lasers are also coupled into the fiber. The power of the signal beam used in the experiment is 30 nW. Both pump waves pass through an acousto-optic modulator (AOM), which is set to a periodic linear ramp at 50 Hz. Additionally, P_1 is further modulated by a chopper rotating at 25 Hz. Thus P_1 is present for only half the time as P_2 which

allows us to monitor the two-photon absorption (TPA) of the signal beam in the presence and absence of the BS-FWM process. The corresponding waveforms are shown in the inset of Fig. 2.3. It can be seen that the idler is generated only when both pump waves and the signal beam are present. At the output port, the output beams are split using a 45:55 beam splitter. Separate photodiodes measure the signal at 776 nm (New Focus 2153) and the generated idler at 762 nm (New Focus 2151). The pump P_1, signal and idler beams are separated using appropriate filters and recorded for a period of 10 seconds.

2.5 Idler generation and effect of two-photon absorption

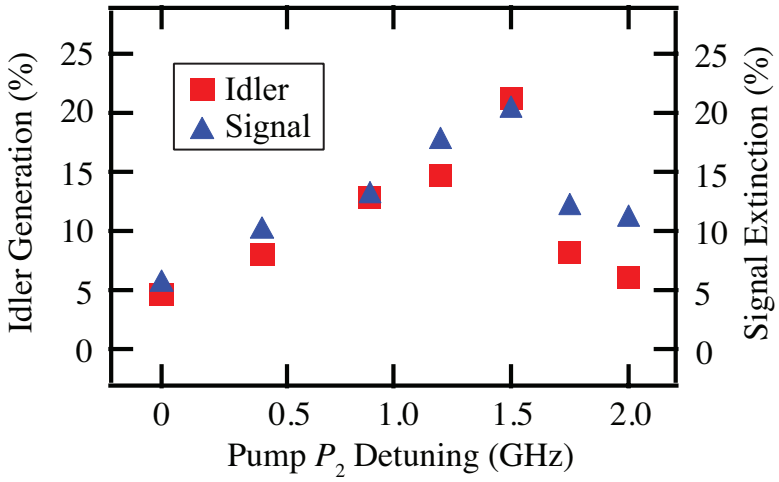

Figure 2.4: Conversion efficiency of the generated idler (red squares) and the extinction percentage of the signal beam (blue triangles) plotted as functions of the detuning of pump field P_2. Data were obtained with the power of pump waves P_1 and P_2 given by 300 μW and 310 μW respectively.

The pump frequencies are detuned sufficiently from the resonance frequency of ^{85}Rb to avoid linear absorption yet still maintain a large nonlinear response. The detunings of pumps P_1 and P_2 are measured with respect to the Doppler broadened resonances, $F = 3 \rightarrow F' = 3$ on the D_1 line and $F = 3 \rightarrow F' = 3$ on the D_2 lines

respectively. The signal beam at 776 nm is detuned from the $5P_{1/2}, (F = 2) \rightarrow 5D_{3/2}, (F' = 1)$ transition. In the absence of pump P_1, the signal beam at 776 nm is absorbed by TPA at the D_2 line. Only when both the pump and the signal beams are present, is the idler waveform generated. In this configuration, the depletion of the signal is due primarily to efficient frequency conversion. Figure 2.4 shows the efficiency with which the signal is converted to the idler as a function of pump P_2 detuning, and it is observed that an optimal detuning (Δ_1 = -1.5 GHz) exists for which the generated idler reaches a maximum conversion of 21%. The strong correlation between the signal depletion and idler generation in Fig. 2.4 indicates

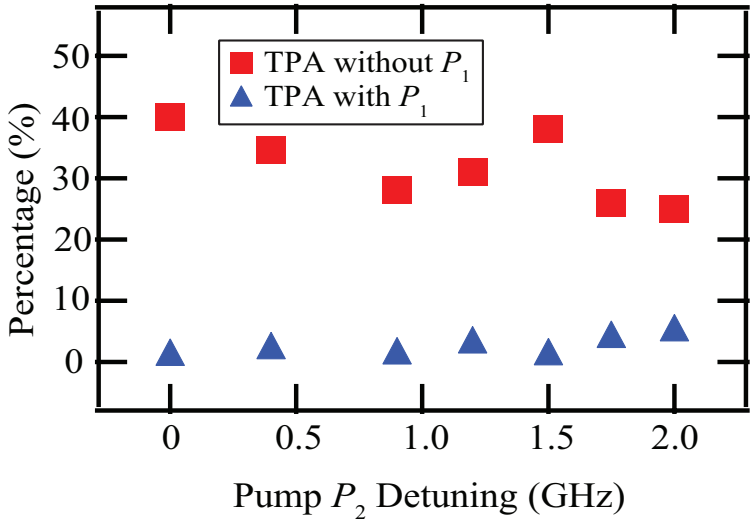

Figure 2.5: TPA in the absence (red squares) and presence (blue triangles) of P_1 is plotted as a function of detuning corresponding to P_2. TPA is seen to be suppressed almost completely in the presence of both the pump beams indicating that BS-FWM is the dominant process.

that TPA of the signal is weaker in comparison to BS-FWM. This is confirmed in Fig. 2.5, where the TPA experienced by the signal beam is plotted as a function of the detuning of pump P_2. For the configuration with pump P_1 absent, the depletion of the signal corresponds to TPA on the D_2 line. For the case in which both P_1 and P_2 are present, TPA on the D_2 line is inferred by subtracting the percentage idler

generation from the signal depletion. It is seen clearly that TPA in the presence of both P_1 and P_2 is suppressed in favor of BS-FWM and similar suppression of nonlinear absorption in the presence of a parametric process has been observed previously [93, 94]. The dominant behavior of BS-FWM with respect to TPA is due to the choice of detunings Δ_1, Δ_2, and Δ_3.

2.6 Theoretical simulation for idler generation

To estimate the third-order susceptibilities $\chi^{(3)}$, we solve the density matrix equations [56,94] by considering only the resonant contributions. The primary nonlinear processes are, FWM generation of the idler, TPA of the signal, and the TPA of the idler, which yield,

$$\chi^{(3)}_{FWM} = N\mu_1\mu_2\mu_3\mu_4/\epsilon_0\hbar\Delta_1\Delta_2\Delta_3, \tag{2.8a}$$

$$\chi^{(3)}_{TPA,D_1} = N\mu_3^2\mu_4^2/\epsilon_0\hbar\Delta_3^2\Delta_2, \tag{2.8b}$$

$$\chi^{(3)}_{TPA,D_2} = N\mu_1^2\mu_2^2/\epsilon_0\hbar\Delta_1^2\Delta_2, \tag{2.8c}$$

where μ_1, μ_2, μ_3, and μ_4 are dipole moments at the four Rb transitions used in our FWM scheme as indicated in Fig. 2.2, and N is the density of Rb atoms in the fiber core. In our experiments pump P_2 is red detuned by $\Delta_1 = -1.5$ GHz and pump P_1 is blue detuned by $\Delta_3 = 256$ MHz. The signal beam is tuned to the $5P_{3/2}, (F = 2) \rightarrow 5D_{3/2}, (F' = 1)$ transition, which yields to $\chi^{(3)}_{TPA,D_1} > \chi^{(3)}_{FWM} > \chi^{(3)}_{TPA,D_2}$ and explains the suppression of TPA of the signal beam in comparison to the generation of idler by BS-FWM. Since $\chi^{(3)}_{TPA,D_1} \gg \chi^{(3)}_{TPA,D_2}$, we can neglect the TPA of the signal beam in the presence of BS-FWM as compared to that of the idler.

For a given optical mode area A of the fiber and normal refractive index n_0,

the effective nonlinearity γ for the FWM process can be defined as [56],

$$\gamma = 3\pi\chi^{(3)}_{FWM}/2A\lambda n_0^2\epsilon_0 c. \tag{2.9}$$

In the ideal case of no other competing processes, the efficiency η (i.e., the ratio of output power of the idler to input power of the signal) is given by [52],

$$\eta = \left|\kappa L \,\mathrm{sinc}\left(\sqrt{|\kappa|^2 + \delta k^2}L\right)\right|^2, \tag{2.10}$$

where $\kappa = 2\gamma A_1 A_2^*$ (A_1 and A_2 are the pump-wave amplitudes), and the phase mismatch $\delta k = (k_2 + k_{signal}) - (k_1 + k_{idler}) + \gamma(P_1 - P_2)/2$. An efficiency of unity is attained if the phase mismatch $\delta k = 0$ and the product $\kappa L = \pi/2$. In the present experiment, an estimate of the refractive index at the wavelengths considered above, give a large phase mismatch $\delta k \gg 1$ for $P_1 = P_2 = 0$. However, for sufficiently large nonlinearity, the nonlinear mismatch term $\gamma(P_1 - P_2)$ can compensate for this linear contribution. In this regime, the conversion efficiency versus the pump power should oscillate rapidly due to the large phase mismatch and at the same time, increase slowly due to the nonlinear phase contribution. Experiments in the Rb-PBGF system show that the atomic density of Rb decays along the length of the fiber. This leads to a variation in refractive index, and hence in phase matching along the fiber core. This can result in the washing out of coherent oscillations, which may explain why we do not observe this behavior experimentally.

We model the effects of TPA on the BS-FWM process using the following set of coupled equations for the idler and signal fields.

$$\frac{\partial A_i}{\partial z} = 4i\gamma P A_i + 2i\gamma P A_s - \alpha P A_i, \tag{2.11a}$$

$$\frac{\partial A_s}{\partial z} = 4i\gamma P A_s + 2i\gamma P A_i, \tag{2.11b}$$

where α is the TPA coefficient at the D_1 line. We assume equal pump powers at both D_1 and D_2 lines (i.e $P_1 = P_2 = P$), and Fig. 2.6 shows the theoretical idler conversion efficiency as a function of pump power P (red curve) for $\gamma = 1.7\times10^5$ $W^{-1}m^{-1}$ and $\alpha = 4.65\times10^5$ $W^{-1}m^{-1}$, which yields excellent agreement between the theoretical curve and experimental data (blue dots). The limited

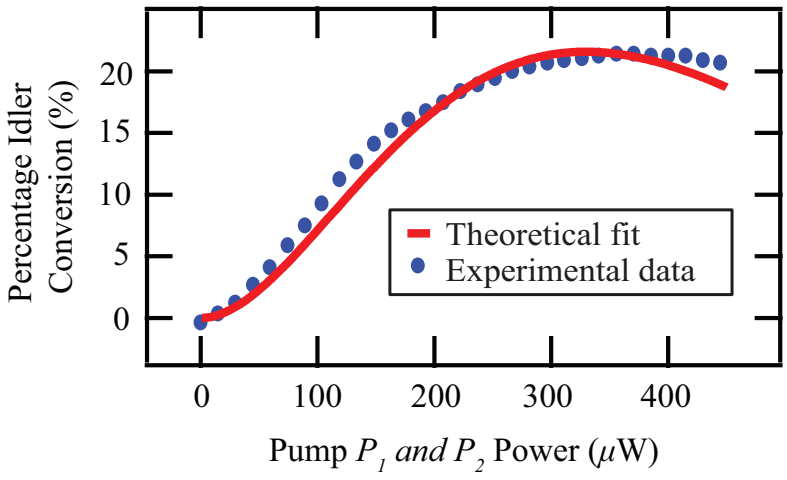

Figure 2.6: Experimental curve (blue) and theoretical fit (red) for idler conversion efficiency as a function of pump power (P_1 or P_2). The idler power increases at first and then saturates because of TPA.

idler conversion efficiency is due to a trade off between TPA on the D_1 line, the BS-FWM process and the varying phase matching conditions along the fiber core. Also from the set of equations 2.8(a) - 2.8(c) and equation 2.9, we observe that $\gamma \propto {\Delta_1}^{-1}$ while the TPA coefficient on the D_1 line is independent of Δ_1. Thus, for a given value of Δ_3, the cross section for BS-FWM decreases with increasing values of Δ_1. On the other hand for extremely small values of Δ_1, the TPA cross section for the signal beam (also proportional to ${\Delta_1}^{-1}$) can be significantly high, thereby limiting the conversion efficiency in that regime. Thus we observe that the frequency translation of the signal beam peaks at a value of Δ_1 = -1.5 GHz in our case [See Fig. 2.4], due to the three competing processes.

2.7 Conclusion

In summary, we achieved 14-nm frequency translation in Rb vapor confined to a PBGF, at a pump power of a few hundred microwatts. To our knowledge, this is the first experimental demonstration of frequency translation in atomic vapors using BS-FWM. We observe that in the presence of both pump beams, BS-FWM is dominant and suppresses TPA on the Rb D_2 line. As a next step, we plan to implement BS-FWM on similar diamond scheme in ^{85}Rb [details in chapter 7], for achieving a frequency conversion from telecom to near-visible with signal-idler separation of 181 THz.

CHAPTER 3

CONTINUOUS GENERATION OF RB VAPOR IN HOLLOW-CORE PHOTONIC BAND-GAP FIBER

In this chapter, we demonstrate high optical depths (> 50) lasting for hours in a Rb-PBGF system which represents a 1000X improvement over operation times previously reported. We investigate the vapor generation mechanism using both a continuous-wave (CW) and a pulsed light source and find that the mechanism for generating the Rb atoms is primarily due to thermal vaporization. Continuous generation of large vapor densities in the Rb-PBGF system should enable measurements at the single-photon level by averaging over longer time scales.

3.1 Introduction

In the previous chapter, we demonstrated frequency translation of light at ultra-low pump power levels by leveraging the large effective Kerr nonlinearity of the Rb-PBGF system. The requirements for achieving such nonlinearities in atomic/molecular vapors are, a high optical depth (OD) [measure of the atomic number density] and a large L/A ratio [section 1.1]. The large nonlinearities of the alkali-filled hollow-core fiber systems has also been a subject of deep investigation in the past works [3, 35, 67, 88, 89], where pioneering studies were performed to demonstrate large cross phase shifts [36, 41], all optical amplitude modulation [60], and quantum memory [47]. A drawback for the warm Rb-filled PBGF platform has been the short time scales of operation, ranging from about a few seconds to a minute. Theories have been proposed to understand the dynamics of Rb atoms inside the fiber core and their interaction with the inner walls of the core [95]. A

detailed analysis suggests that Rb nanoclusters form inside the core of the fibers, and their subsequent vaporization using intense beams is responsible for the high OD. However, the Rb vapor obtained by thermal vapor generation from the loosely bound nano-clusters is quickly lost to the fiber walls and previous studies done in our group [3] clearly show that large OD's in the PBGF core lasts only for a few seconds after exposure to the vapor generating beam (See Fig. 3.1). Furthermore, the system requires an extended duration ($<$ 3 hrs) to re-establish high OD operation [35, 95, 96]. Thus, high OD's that are a key to achieving high third order nonlinearities are available only for a few seconds which largely limited the operation time of the system.

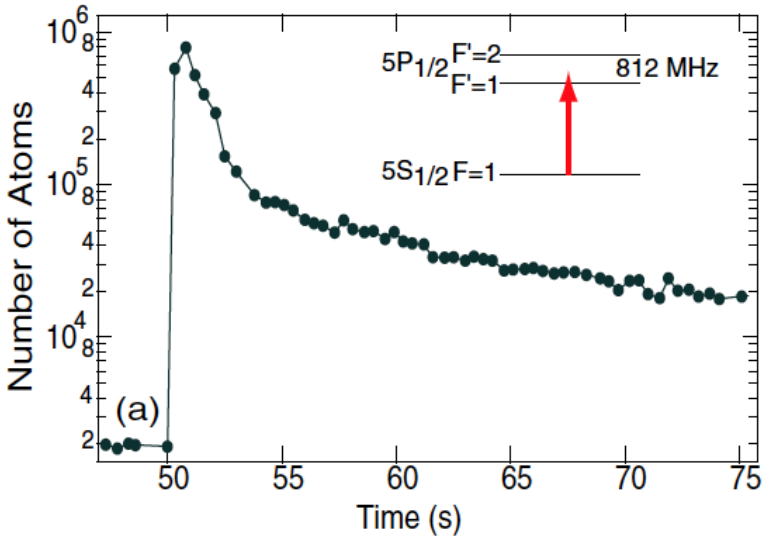

Figure 3.1: Plot of number of atoms measured in the fiber core as a function of time elapsed after exposure to the vapor generation beam [3]. The number of atoms are estimated by measuring the transmission of a probe beam close to resonance on the D_1 transition of Rb (level scheme in inset). The beam is coupled into the PBGF at t = 50 s after which the number of atoms in the fiber-core peak for a few seconds and within 20 seconds settle down to an equilibrium state which is a factor of 100 less atoms than those at the peak.

More recently, high OD's have been observed by loading cold atoms in a PBGF from a MOT [69] and the diffusive loading of a Kagomé-type PBGF with mercury

vapor, capable of achieving high optical nonlinearities in the UV regime [66]. In the follow sections, we shall describe a 1000X improvement in interaction times in Rb-PBGF over those previously achieved in such systems for OD's > 50. Such long operating times were achieved using vapor generation beams with substantially higher average powers and wavelengths close to the band edge of the PBGF. The generated OD's are commensurate with those required for all previous demonstrations of optical modulation using the Rb-PBGF system [41, 57, 60, 88, 89, 97]. This capability greatly facilitates performing experiments related to weak nonlinearity-based quantum computing [98]. Varying the power and wavelength of the vapor generation beam offers further insight into the mechanism leading to sustained OD's. We also investigate vapor generation using mode-locked pulses and compare it with our results using a continuous-wave (CW) beam, from which we conclude that it is the average and not the peak power which facilitates the generation of high OD's.

3.2 Experiment

We study continuous OD generation in the same Rb-PBGF system, which was used to demonstrate BS-FWM described in chapter 2. A standard cleaning procedure for vacuum components was followed, after which we pre-baked the chamber for over a month to achieve ultrahigh vacuum (pressure $<10^{-9}$ Torr) before the Rb vapor was released. The Rb density slowly builds up in the core of the PBGF over a period of two weeks by diffusion of warm Rb vapor from the chamber. We let the fiber-core densely load with Rb atoms over a period of about 18 months during which we periodically monitored the OD generated by the vapor generation beam. An external cavity diode laser (Toptica, TA 100) tuned to the D_1 line of ^{85}Rb and

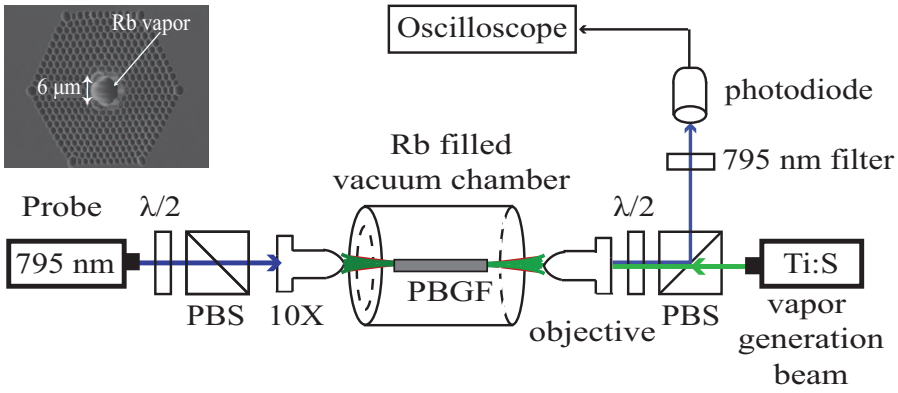

Figure 3.2: A weak probe beam at 795 nm and a vapor generation beam are sent counterpropagating into the Rb-filled photonic band-gap fiber (PBGF) using 10X objectives. The probe is scanned across the D_1 line of Rb. After propagating through the fiber, the probe beam is cleared out using spectral filters from any stray light that originates from the back reflected component of the vapor generation beam. The absorption of the probe beam is measured with a photodiode.

set to a mode-hope-free scan serves as the weak probe. The power of the probe beam is maintained at ~ 1 nW, which is below the saturation power of Rb vapor in the core of the PBGF [58]. The CW output from a home-built Titanium sapphire (Ti:S) laser, tunable from 772 nm to 810 nm is used for Rb vapor generation. For pulsed measurements, the laser is mode-locked to generate 100-fs pulses at a repetition rate of 80 MHz. Both the probe and vapor generation beams are free-space coupled into the fiber using 10X objectives. Including coupling losses, the transmission through the fiber exposed to Rb vapor gradually drops over a month to 23% during continuous operation as compared to 70% for a pristine fiber. Formation of metallic clusters at the core walls make the transmission loss high over a broad frequency range. The transmission of a fully loaded fiber prior to vapor generation can be as low as 10% and the transmission rises gradually to 23% for off-resonant vapor generation as the Rb atoms are released from the core walls. The Rb vapor in the chamber is an isotopic mixture of ^{85}Rb and ^{87}Rb in a ratio of 7:3. As seen in Fig. 3.2, both probe and vapor generation beams are sent

counter propagating into the fiber, so that the weak probe can be easily separated. The probe beam after propagation is separated using a band-pass filter at 795 nm and is measured using a photodiode.

3.3 Optical depth (OD) measurement

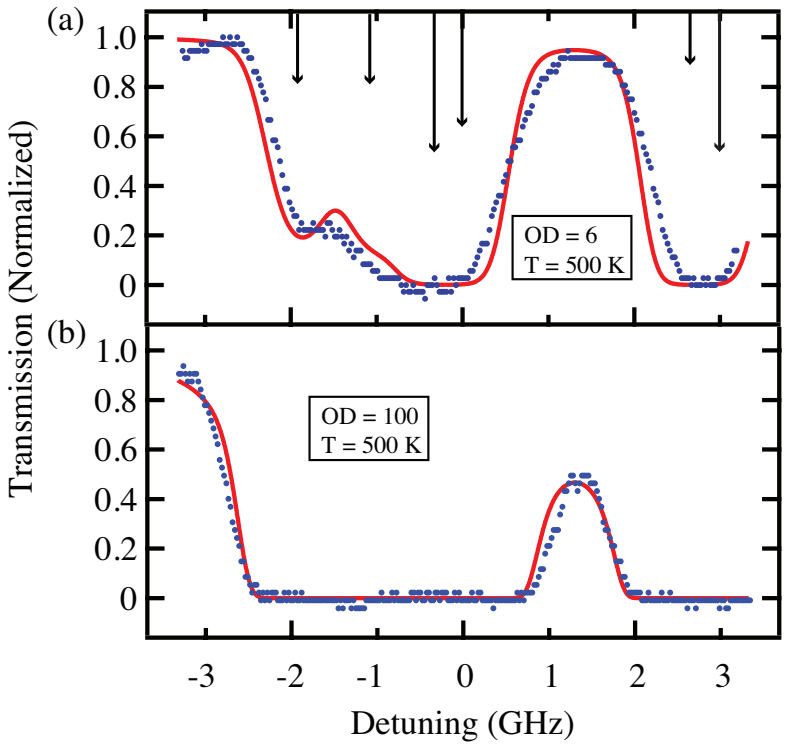

Figure 3.3: The absorption of the probe beam is plotted as a function of detuning, for vapor generation beam at (a) 17.3 mW and (b) 48 mW. The frequency scale is zeroed at the F = 3 $\rightarrow$ F' = 3 transition on the ^{85}Rb D_1 line. Each of the above absorption curves is fit to a Voigt function taking into account the Doppler and transit time broadened hyperfine transition on the ^{85}Rb and ^{87}Rb D_1 line. From the fit, the temperature of the Rb vapor in the core can be estimated to be $T \sim$ 500 K.

We estimate the generated OD by fitting the absorption experienced by the probe to a Voigt function. Figure 3.3, shows the probe absorption (blue points) during a scan across the D_1 line of ^{85}Rb and ^{87}Rb at different powers of the vapor

generation beam. All detunings are measured with respect to the F = 3 → F' = 3 transition on the ^{85}Rb D_1 line. We fit the probe absorption data to a Voigt profile (red curve) which takes into account both the homogeneous (Lorentzian) and inhomogeneous Doppler broadened (Gaussian) line shapes. Since the Rb atoms are confined to a 6-μm diameter core, the interaction time with the optical mode is limited to the time it takes for the atoms to move across the beam and leads to transit-time broadening of the absorption lines, which we take into account while simulating the Voigt function [96,99]. The temperature of the Rb atoms inside the core is inferred to be $T \sim 500$ K from the Voigt function fit in Fig. 3.3(a)-(b). The higher temperature of the atoms (500 K) as compared to the chamber temperature of 373 K appears to be a result of the high kinetic energy of the released atoms [99] which also results in the increased Doppler broadening of the Rb transition lines. We also note that the large OD's are only generated when the vapor generation beam is coupled into the fiber core. Secondly, the OD inside a 2-cm-long section of the chamber is 0.5, which tells us that the 0.5-mm-long air gap region between the fiber tip and the chamber view-port on each side contribute negligibly to the total OD when the vapor generation beam is coupled into the fiber.

3.4 OD using a CW vapor generating beam

We first demonstrate large OD's using a CW vapor generation beam. A strong CW beam at 805 nm is coupled into the fiber, and the generated OD is continuously monitored by measuring the transmission spectrum of the probe beam. Figure 3.4 shows the OD as a function of elapsed time. We observe that high OD's, as large as 200, are generated for a few minutes and thereafter a stable OD = 50±5 is observed for over 100 minutes, which represents a 1000X improvement of operation time of

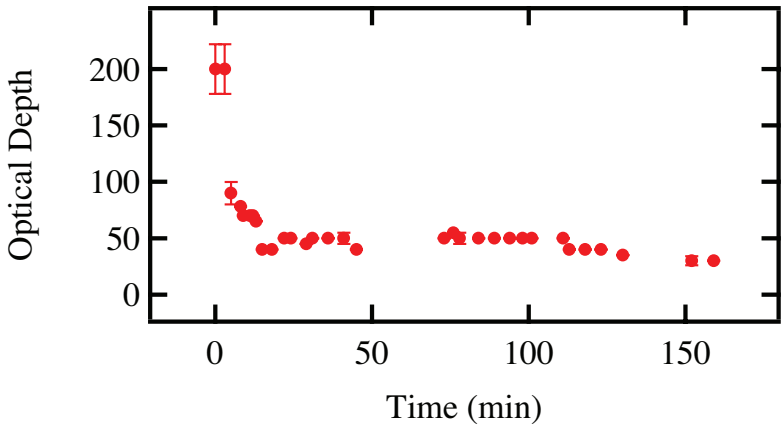

Figure 3.4: Optical depth (OD) generated due to CW vapor generation is plotted as a function of elapsed time. It is observed that high OD's $\sim$ 200 are generated for a few minutes and thereafter the OD stabilizes to 50$\pm$5 for over 100 minutes of operation. The measurement is performed for 35 mW of vapor generation beam power transmitted through the PBGF.

the system over that previously reported [3, 35, 41, 47, 60, 88, 89, 95, 97]. For our Rb-PBGF system, an OD $\sim$ 50 corresponds to an atomic number density $N \approx 10^{19}$ atoms/m^3. The transmitted power of the vapor generation beam through the fiber is 35 mW for 150 mW of power at the input end. The low transmission through the PBGF is due to the presence of Rb at the core walls which increases scattering losses and modifies the guiding properties of the fiber over time after long exposure.

3.4.1 OD vs power for CW vapor generating beam

The generated OD is also measured as a function of vapor generation beam power as shown in Fig. 3.5. Since we observed no evidence of saturation up to vapor generation powers of 48 mW (see Fig. 3.5), we expect that larger OD's can be generated at even higher powers. Currently we are limited by the CW power of the Ti:S oscillator.

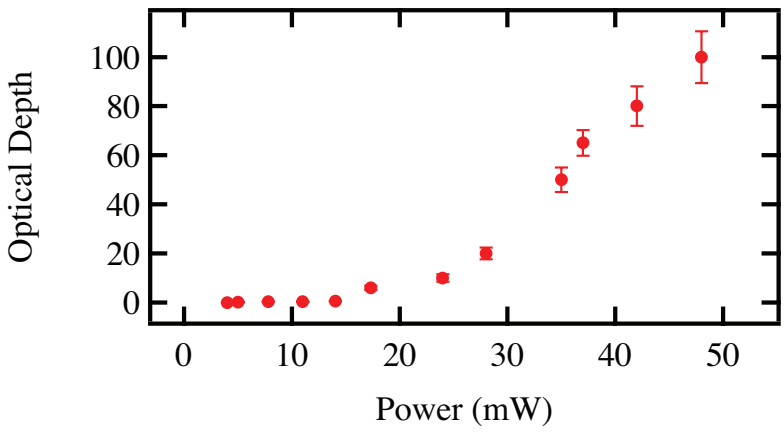

Figure 3.5: The generated OD is plotted as a function of power of the vapor generation beam transmitted through the PBGF. It is observed that at lower powers, the OD increases slowly. However, beyond a vapor generation beam power of 23 mW, the OD continues to increase.

3.4.2 OD vs wavelength for CW vapor generating beam

We also examine the wavelength dependence of the vapor generation beam within the band gap of the fiber. Figure 3.6 shows the generated OD as a function of wavelength of the vapor generation beam (blue points). The green arrows in the figure indicate the D_1 and D_2 transitions of Rb. The OD at each wavelength is measured for 30 mW of power transmitted through the fiber. We also plot the transmission data for the PBGF (red curve) [1]. It is observed that the OD generated from 800 to 805 nm is 3X that generated at wavelengths within the band edge. We find that OD generation decreases as the wavelength of the vapor generation beam is tuned further away from the photonic band gap. We believe this is due to increase in the guiding loss which reduces the power of the vapor generation beam as it propagates along the fiber. Thus, OD's are generated most efficiently when the vapor generation beam wavelength is chosen to be at the band edge of the PBGF. This is as expected since the optical mode would become more delocalized at the edge of the band-gap and more of the light from the vapor generation beam

will be at the core walls. The Ti:S laser used for the experiment is tunable only to 772 nm, and hence we could not acquire data below this wavelength further into

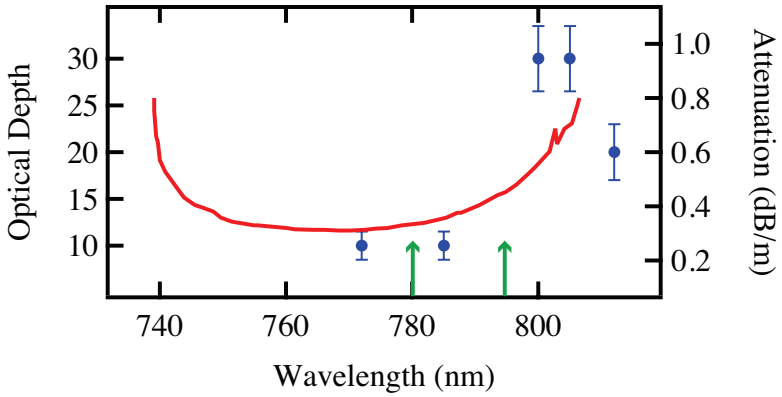

Figure 3.6: Optical depth (OD) generated due to the vapor generation beam is plotted as a function of its wavelength (blue points). The curve in red shows the transmission data of the fiber and defines its band-gap [1]. The green arrows indicate the D_1 and D_2 transition of Rb. It is observed that the OD's generated at wavelengths within the band gap are lower than at wavelengths close to the edge and slightly beyond. As we move further away from the edge, the generated OD's decrease.

the bandgap. Typically for our experiments exploring nonlinear interactions with Rb vapor, we choose a vapor generation beam wavelength of 805 nm, since it is far away from both the Rb D_1 and D_2 lines and hence would not lead to any resonant interaction with Rb vapor or cause significant AC stark shifting of its hyperfine levels at high intensities [96]. Additionally, it is easy to separate a probe tuned to any Rb transition from the vapor generation beam using a spectral filter.

3.5 OD using pulsed vapor generating beam

As a final test of the origin of the Rb vapor in the core, we performed the experiment using a mode-locked Ti:S laser. The pulsed source was used to study the impact of average versus peak power on the vapor generation process. A 100-fs

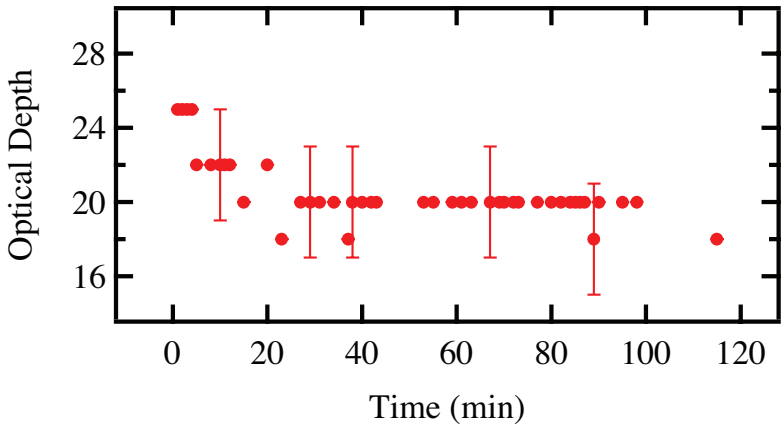

Figure 3.7: OD generated due to pulsed high peak power beam is plotted as a function of elapsed time. It is observed that a stable OD = 20±3 is generated for over 90 minutes of operation. The average power through the core is 22 mW while the peak power is 40 KW.

pulse with a repetition rate of 80 MHz and average power of 100 mW (40 KW peak power) was used to generate the vapor. Figure 3.7 plots the OD generated using a pulsed source, as a function of elapsed time. It is observed that a stable OD = 20±3 is generated for over 100 mins at an average power of 22 mW transmitted through the fiber. It can be inferred that the OD's generated using a pulsed source are comparable to those using a CW beam at similar average powers as shown in Fig. 3.5. This indicates that the density of Rb atoms inside the core of the PBGF depends on the average and not the peak power of the vapor generation beam.

3.6 Model for vapor generation process

Based on our observations, we propose a model that explains the dynamics of Rb atoms inside the fiber core. It has been suggested that the OD inside the core is generated by a fast mechanism and a slow mechanism [95]. The OD's generated by the fast process (i.e., laser desorption of Rb atoms chemically bonded to the

core wall) are usually low (OD $\sim$ 0.5) but require short regeneration times $\sim$ 50 μs [95], while those generated from the slow mechanism are extremely large (OD $\sim$ 1000), and last for only a few seconds [99]. The source for the generation of these high OD's by the slow mechanism are atoms that are contained in Rb nanoclusters that can be thermally evaporated at relatively low average powers of the vapor generation beam. At these low average powers, the vapor quickly dissipates within a few seconds since atoms that are chemically bound to the surface of the core walls require larger powers to be released. Accordingly, as the power of the vapor generation beam is continuously increased beyond those required for the slow mechanism, more and more atoms chemically held to the core walls are released and a state of equilibrium is reached at each power level resulting in a stable and sustained OD for extended time scales ranging up to a few hours. Our results shown in Fig. 3.6, also indicate that the vapor generation efficiency is greater at wavelengths at the photonic band edge of the fiber, which is a result of the corresponding mode of vapor generation beam being pushed into the core walls, increasing the fraction of power at the surface, and assisting in efficient generation of large OD's

3.7 Conclusion

In summary, we demonstrate continuous ODs in the Rb-PBGF system for times that are $>$ 1000X longer than those previously demonstrated. The primary reason for obtaining large and persistent OD's is the use of vapor generation beam with substantially higher average power. Our observations indicate that vapor generation is more efficient at the photonic band edge as the field mode inside the core is more concentrated near the surface which prevents the atoms from sticking to

the core wall. We also establish that the vapor generation process depends on the average and not the peak power. We believe our system will allow us to attain continuous, strong light-matter interactions at the single-photon level. As a next step, we plan to use the continuous OD's in the Rb-PBGF system to demonstrate a high CPC pair generation efficiency as discussed in section 4.7.

CHAPTER 4

SUB-DOPPLER QUANTUM CORRELATED PHOTON PAIRS IN WARM RB-VAPOR; TOWARDS COHERENT PHOTON CONVERSION

In this chapter, we demonstrate the generation of quantum-correlated photon-pairs by spontaneous four-wave mixing using a diamond level scheme on the $5S_{1/2} \rightarrow 5D_{3/2}$ two-photon transition in ^{85}Rb. Photon-pair generation is also realized in the regime of an undepleted pump and a weak input beam, mimicing an effective second order nonlinear process (CPC) [4]. We measure a CPC pair generation efficiency of $6.3\text{x}10^{-8}$ pairs/input photon/kW of the pump beam, which is a 10X improvement over CPC efficiencies reported till date. We further propose an implementation of the above scheme in a Rb-PBGF system that can enhance the pair generation efficiency by a factor of 10^8, which could potentially lead to deterministic quantum logic operation and development of on-demand single photon sources.

4.1 Correlated photon pair generation

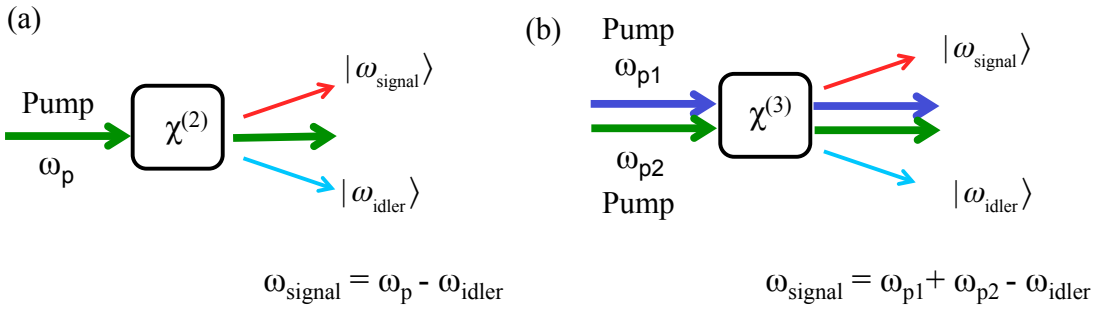

Figure 4.1: (a) Correlated photon pair generation from spontaneous parametric down-conversion in a $\chi^{(2)}$ medium. (b) Correlated photon pair generation from spontaneous four-wave mixing in a $\chi^{(3)}$ medium.

Correlated photon pairs are generated as result of conservation laws governing nonlinear optical process. For example, when a pump beam (ω_p) enters a $\chi^{(2)}$ medium like a PPLN or a BBO crystal [Fig. 4.1(a)]; the original pump photon is converted to a pair of photons [lets call them signal (ω_s) and idler (ω_i)], by the process of spontaneous parametric down conversion (SPDC) [100–102], such that sum of the energies of the photon pairs equal the energy of the input photon i.e. $\omega_s + \omega_i = \omega_p$. More quantitatively, the Hamiltonian for the SPDC process can be written as [103],

$$\hat{H}_{SPDC} \propto \hbar\chi^{(2)}\hat{a}_p\hat{a}_s^\dagger\hat{a}_i^\dagger + h.c, \tag{4.1}$$

where $\hat{a}_k(\hat{a}_k^\dagger)$, $k = \{p, s, i\}$ are the annihilation(creation) operators for the pump, signal and idler modes respectively. Treating the pump beam classically, the resulting quantum state from a process engineered to emit photons in a single spatial and spectral mode can be written as,

$$|\psi_{SPDC}\rangle = \exp[r(\hat{a}_s^\dagger\hat{a}_i^\dagger - \hat{a}_s\hat{a}_i)]\,|0\rangle \tag{4.2}$$

which further simplifies to,

$$|\psi_{SPDC}\rangle = \mathrm{sech}(r)\sum_{n=o}^{\infty}\tanh^n(r)\,|n_s, n_i\rangle \tag{4.3}$$

where, 'r' depends of the strength of the nonlinearity and power of the pump beam and $\mathrm{n_s}(\mathrm{n_i})$ is the number of photons in the signal(idler) mode. For known $\chi^{(2)}$ media, a fundamental limitation of SPDC is that, heralding $|\psi_{SPDC}\rangle$ on the idler photon can lead to a mixed quantum state for the signal photon. The resulting heralded state for the signal photon contains higher order photon components which reduces the purity of the state.

Similar to the SPDC process, correlated photon pairs have been generated in a $\chi^{(3)}$ medium like, nonlinear fibers [104–106] and chip-based platforms [38,

39, 48–51, 107–109] by the process of spontaneous four-wave mixing (SFWM). As seen in Fig. 4.1(b), the interaction between two pump photons [say P1(ω_{P1}) and P2(ω_{P2})] leads to the generation of a pair of photons [signal (ω_s) and idler (ω_i)] by SFWM, such that $\omega_s + \omega_i = \omega_{P1} + \omega_{P2}$. Such photons are strongly correlated in energy. Quantum correlations can also exist in other domains like polarization [92, 110] and time. SWFM in warm Rb-vapor has gained increasing attention recently [110–114] as a robust method to generate correlated photon pairs for quantum communication networks based on quantum memories. A key advantage of this platform is that the photon pairs generated by such means match the bandwidth and wavelength requirements for alkali-vapor-based quantum memories [44–47]. Moreover, due its resonant nature, the effective nonlinearity for pair generation can be very high which allows for spectrally bright pair-generation [110–114]. A critical advantage of using warm Rb-vapor instead of cold ensembles is the reduced complexity of such a system which makes it easier to scale. To date, a number of different level schemes have been used in warm Rb-vapor, including a diamond scheme [110, 111], ladder-schemes [112–114], and a lambda scheme [115], to generate correlated photon-pairs.

As we have seen in earlier chapters, nonlinearities can be greatly enhanced by using warm Rb-vapor inside PBGF's [3, 41, 60], which could be extremely useful in increasing the efficiency of the pair generation. Our recent progress in improving the operation lifetimes of the Rb-PBGF system as explained in chapter 3, could enable continuous generation of spectrally bright photon pairs. One of our primary motivations for generating pairs of photons with high efficiency, is to implement CPC for quantum information processing [4]. In the next section we shall discuss the CPC scheme.

4.2 Coherent photon conversion (CPC)

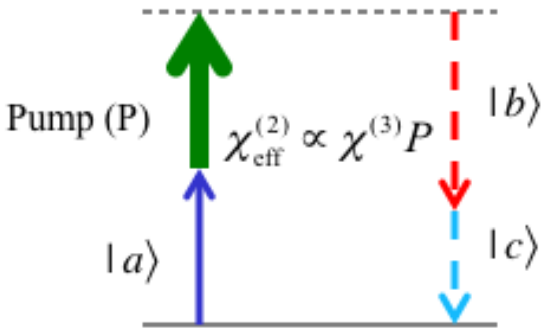

Figure 4.2: Four wave mixing between a strong pump P and three quantum modes $\hat{a}_a, \hat{a}_b$, and $\hat{a}_c$, in a $\chi^{(3)}$ medium, mimicing an effective second order process $\chi^{(2)}_{eff}$, such that $\chi^{(2)}_{eff} \propto \chi^{(3)} P$.

The CPC process is based on FWM (i.e $\chi^{(3)}$ nonlinearity) between a strong pump field (Power = P) that produces an effective second-order nonlinearity $\chi^{(2)}_{eff}$ for three quantum modes with annihilation operators $\hat{a}_a, \hat{a}_b$, and $\hat{a}_c$, as seen in Fig 4.2. To understand the CPC process more quantitatively, we introduce the Hamiltonian for the FWM process as [4],

$$\hat{H} = \hbar\kappa \hat{a}_a \hat{a}_P \hat{a}_b^\dagger \hat{a}_c^\dagger + h.c., \tag{4.4}$$

where, $\hat{a}_P$ is the mode-field operator for the pump beam and κ is the strength of the interaction, which depends on the effective nonlinearity γ of the system and is given as,

$$\kappa = \frac{c\gamma\hbar\omega}{\tau}, \tag{4.5}$$

here, τ is the inverse bandwidth of the optical modes, and as seen in chapter 2,

$$\gamma = 3\pi\chi^{(3)}_{FWM}/2A\lambda n_0^2 \epsilon_0 c \tag{4.6}$$

In comparison to modes a,b and c, we can treat the pump classically and write down the modified interaction Hamiltonian as,

$$\hat{H}_{eff} = \hbar\Gamma \hat{a}_a \hat{a}_b^\dagger \hat{a}_c^\dagger + h.c., \tag{4.7}$$

with,

$$\Gamma = \kappa\sqrt{N_P}, \tag{4.8}$$

where, N_p is the average number of photons in the pump beam, per pulse width τ. From the form of $\hat{H}_{eff}$, Γ can be interpreted as the coupling constant for an effective second order nonlinear process ($\chi^{(2)}_{\text{eff}}$) between modes a,b and c. Unlike the $\chi^{(2)}$ for known materials, the strength for $\chi^{(2)}_{\text{eff}}$ can be engineered to a large value by increasing the pump field intensity and by selecting a nonlinear medium with a large γ. Under the influence of this $\hat{H}_{eff}$, a quantum state with one photon in mode a, i.e. $\psi(0) = |100\rangle_{abc}$ evolves as,

$$\psi(t) = \cos(\Gamma t)|100\rangle_{abc} + \sin(\Gamma t)|011\rangle_{abc}. \tag{4.9}$$

From equation 4.9 we see that, if Γt ~ 1, photons can be coherently converted

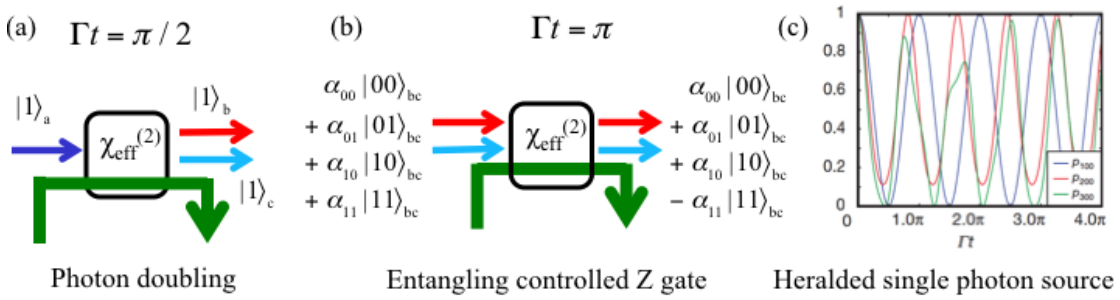

Figure 4.3: (a) Implementation of 100% photon doubling with a $\Gamma t = \pi/2$. (a) Maximally entangling controlled Z gate implemented by having $\Gamma t = \pi$. (c) Evolution of 1 (blue), 2(red) and 3(green) photon Fock states (photon number state) under a CPC scheme, shows that different values of Γt can be used to achieve a single photon by starting of in an arbitrary state and filtering out the higher photon components [4].

between the three quantum modes. For example, consider the case of an input state $|100\rangle_{abc}$ at time t = 0. If the strength of the interaction length $\Gamma t = \pi/2$, $|100\rangle_{abc}$ evolves to $|011\rangle_{abc}$ as per equation 4.9, thereby realizing a 100% photon doubler [see Fig. 4.3(a)]. Secondly, if we set $\Gamma t = \pi$, an input state $|011\rangle_{abc}$ at

t = 0, evolves to -$|011\rangle_{abc}$. Thus an input state $\psi(0) \propto |000\rangle_{abc} + |001\rangle_{abc} + |010\rangle_{abc} + |011\rangle_{abc}$ [see Fig. 4.3(b)], shall evolve to $\psi(t) \propto |000\rangle_{abc} + |001\rangle_{abc} + |010\rangle_{abc} - |011\rangle_{abc}$ for $\Gamma t = \pi$, which is also a maximally entangled state. CPC can thus be potentially used to realize deterministic multi-qubit entangling gates (such as the controlled-phase gate above), generate high-quality heralded single and multi-photon states, and improve single-photon detection efficiencies.

Another feature worth mentioning about CPC is that, the Fock states (photon number states) with different number of photons evolve differently under the CPC interaction [Fig. 4.3(c)], and we can utilize this effect to create single photons states from a weak coherent state by sequential cycling. It is predicted that in just 5 steps, a weak coherent state ($|\alpha|^2 = 1.5$) can be converted to a single photon state with $\sim 56\%$ efficiency [4]. Finally CPC can allow for a $\chi^{(2)}$ interaction with all three modes at comparable frequencies, which is usually not possible in other naturally available or engineered $\chi^{(2)}$ media.

4.3 Level scheme for CPC in warm ^{85}Rb

In this work, we demonstrate for the first time, photon pairs generated with high efficiency using collinear beam propagation and diamond scheme employing the $5S_{1/2} \rightarrow 5D_{3/2}$ transition in a warm ^{85}Rb vapor [Fig. 4.4], by the process of SFWM. The diamond scheme was specifically chosen as all wavelengths involved are compatible with the Rb-PBGF system [97] which has been demonstrated in chapter 2 and this could lead to a further increment in pair generation efficiency by a factor of 10^8. As seen in Fig. 4.4, a weak input field at 780 nm, detuned from the $5S_{1/2}$, F = 3 $\rightarrow$ $5P_{3/2}$, F' = 4 transition and a strong pump beam at 776 nm ($5P_{3/2} \rightarrow$

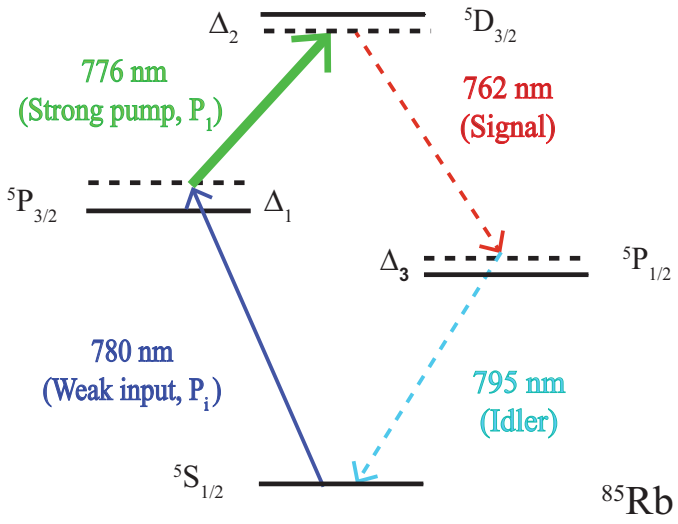

Figure 4.4: A strong pump beam at 776 nm and a weak input at 780 nm, tuned to the two photon transition $5S_{1/2} \rightarrow 5D_{3/2}$, lead to the generation of photons at 762 nm (signal) and 795 nm (idler) via spontaneous four-wave mixing. Maximum pair generation efficiency is achieved with the weak input being blue detuned with respect to the $5S_{1/2}$, F = 3 $\rightarrow$ $5P_{3/2}$, F' = 4 transition by 910 MHz ($\Delta_1 = 910$ MHz) and $\Delta_2 = 0$.

$5D_{3/2}$ transition) lead to the generation of a pair of photons at 762 nm and 795 nm. For maximum pair generation efficiency, the weak input and the pump are maintained at two-photon resonance ($\Delta_2 = 0$) with respect to the $5S_{1/2}$, F = 3 $\rightarrow$ $5D_{3/2}$ transition. We shall hence forth refer to the 762 nm and 795 photons as signal and idler respectively. Previously, this scheme has been demonstrated in a cold atomic ensemble for the generation of correlated pairs [92]. The input field is blue detuned by 910 MHz to prevent linear absorption at the D_2 transition of Rb. To avoid any higher order nonlinear effects and optical pumping of the ground states, the strong pump is chosen at 776 nm and the weak input is at 780 nm.

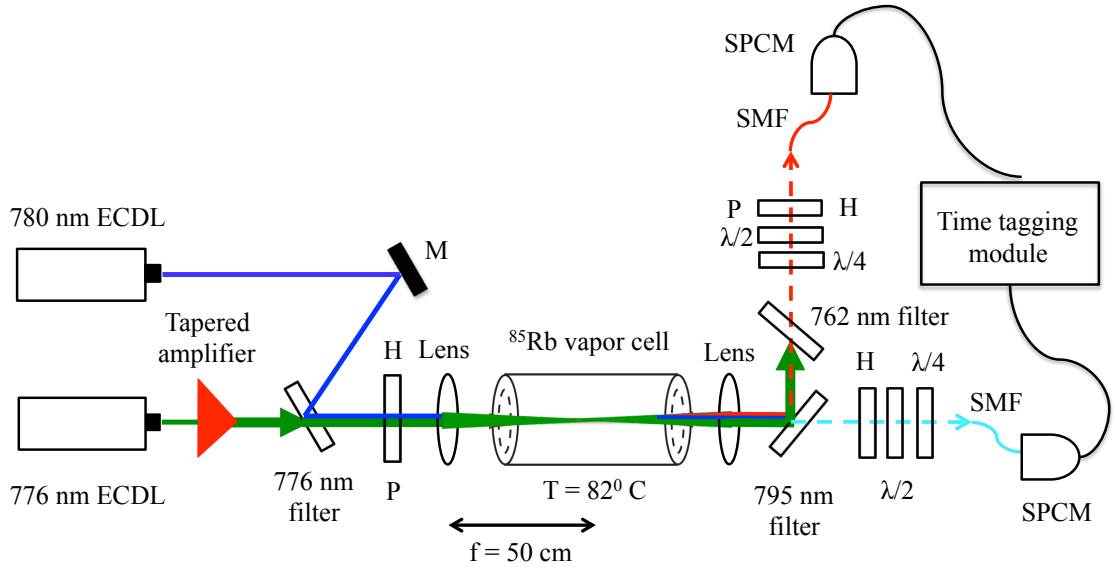

Figure 4.5: A strong pump beam at 776 nm and a weak input field at 780 nm, generated using ECDL's, are horizontally (H) polarized and sent co-propagating in an isotopically pure ^{85}Rb cell. The signal (762 nm) and idler (795 nm) photons generated as a result of SFWM, are spectrally filtered and collected using single mode fibers post selecting on the H polarization. The signal and idler photons are detected using single photon counting modules (SPCM's) and the timing correlation between them is measured using a time tagging module.

4.4 Experimental setup

The schematic for generating correlated photons is shown in Fig. 4.5. Horizontally (H) polarized pump and input beams at 776 nm and 780 nm respectively, generated using external cavity diode lasers (Toptica DL 100) are sent co-propagating and collinear in a 2-cm-long isotopically pure ^{85}Rb vapor cell. A beam waist of 125 μm is achieved at the centre of the vapor cell using a convex lens (focal length = 50 cm), for both the pump and weak input beams, and the cell temperature is maintained at 82°C. Quantum correlated photons at 762 nm and 795 nm generated from SFWM are separated using band-pass filters. Due to the selection rules, generated photons are expected to be either HH or VV polarized, and we post-select the H-polarized photons. Maximum efficiency is achieved with the pump and the input beam being

on two-photon resonance $\Delta_2 = 0$. The photons are collected using single mode (SM) fibers and detected using single photon counting modules (SPCM) [Excelitas SPCM-AQR-16]. The timing correlation between the signal and idler field photons is then determined by measuring the coincidence statistics, facilitated by a time tagging module [AIT-TTM8000].

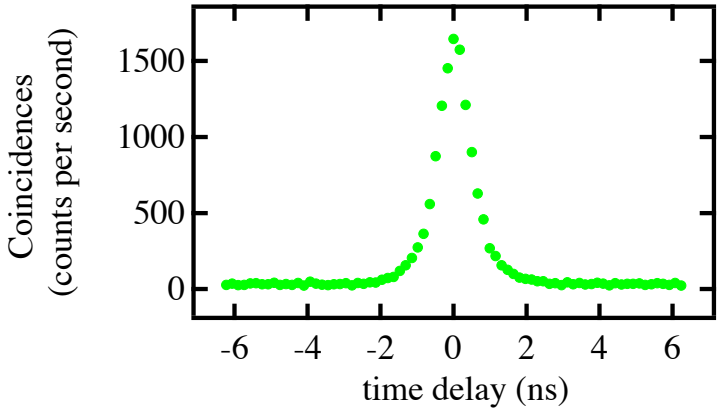

Figure 4.6: Background uncorrected coincidences between signal and idler fields are plotted as a function of time delay with the pump beam at 800 mW and the input field at 500 nW. We see a large signal to noise ratio between the coincidence peak and the background counts, and the observed second order correlation at zero time delay is, $g^{(2)}_{SI}(0) = 49.02 \pm 1.54$.

4.5 Non classical correlations - Cauchy Schwarz inequality

We establish the non-classical nature of the generated photon pairs by showing a large violation of the Cauchy Schwarz (CS) inequality. After correcting for all the loss factors, which include: coupling losses into the SM fibers, detector efficiency and the transmission losses from the spectral filters (all values of coincidences and singles, mentioned throughout the work are corrected for the above loss factors); the background uncorrected coincidences between signal and idler fields (averaged

for 2 hours) are plotted in Fig. 4.6 as a function of time delay. We observe a large coincidence peak over background counts, leading to a second order correlation value of $g^{(2)}_{SI}(0) = 49.02 \pm 1.54$ at zero time delay [refer to appendix B for all calculations performed in this chapter]. The power of the pump beam and input field are maintained at 800 mW and 500 nW respectively. The measured autocorrelation for the idler field yields a $g^{(2)}_{I}(0) = 1.04 \pm 0.063$ and that for the signal results in a $g^{(2)}_{S}(0) = 1.92 \pm 0.09$. For nonclassical correlations [116],

$$R = \frac{g^{(2)}_{SI}(\tau)^2}{g^{(2)}_{S}(0) g^{(2)}_{I}(0)} > 1 \tag{4.10}$$

We measure R = 1203.4 ± 119.2, indicating a > 10-σ violation of the Cauchy Schwarz inequality, clearly showing the nonclassical nature of the observed correlations between signal and idler photons.

4.6 Second order correlation functions - signal and idler

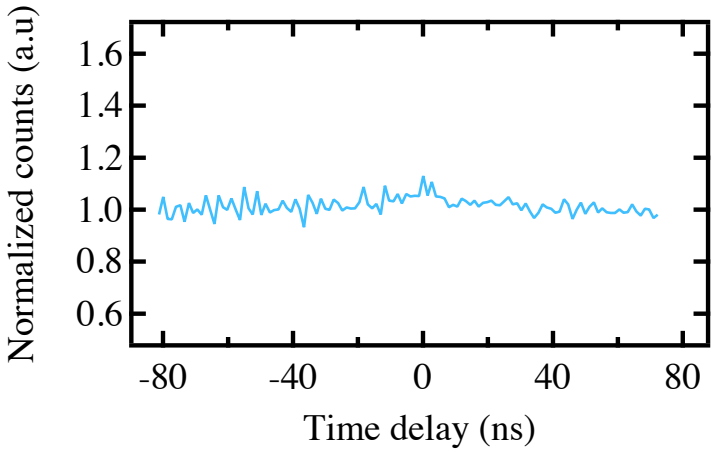

Figure 4.7: The autocorrelation for the idler photon at 795 nm appears like that of a coherent state with a $g^{(2)}_{I}(0) = 1.04 \pm 0.063$. This is due to the multiple scattering of resonant idler photons in the optically dense Rb vapor leading to a narrow autocorrelation function in time, below the resolution of our detectors.

The statistics for the idler photons appear like that of a coherent state ($g_I^{(2)}(0) = 1.04 \pm 0.063$) as seen in Fig. 4.7, as opposed to the expected thermal statistics of photons emitted from a SFWM process. As large optical depths are required for high pair generation efficiency, the idler photons resonant with the D_1 line are absorbed and emitted several times in the dense vapor. These multiple scattering events cause the frequency for the re-emitted photons to spread over the Doppler

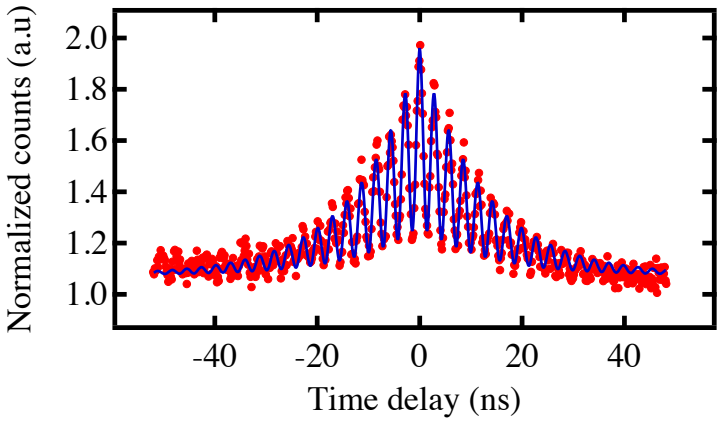

Figure 4.8: The autocorrelation for the signal field (red points) is plotted as a function of time delay. The observed fringes are due to the interference of the photons emitted on the $5D_{3/2} \rightarrow 5P_{1/2}$, F' = 3 and F' = 2 transition separated by 361 MHz. The time period of oscillation from the fit function (blue curve) is 353.98 $\pm$ 1.50 MHz. The narrow band nature of the emitted photons can be attributed to the narrow phase matching condition for the SFWM process.

broadened width of each transition, leading to a narrow correlation function in time which is below the resolution of our SPCM's. Hence the measured second order correlation function yields a $g_I^{(2)}(0) \sim 1$. This effect has also been reported in earlier works of photon-pair generation using SFWM in a diamond-type scheme in Rb [111].

Figure 4.8 plots the second order correlation for the signal photons, with a $g_S^{(2)}(0) = 1.92 \pm 0.09$ which is consistent with thermal statistics. The signal photons could be emitted on either the $5D_{3/2} \rightarrow 5P_{1/2}$, F' = 3 or $5D_{3/2} \rightarrow 5P_{1/2}$, F' = 2

transition, and the observed periodic fringes are due to interference between the two possible path ways. We attribute the reduced visibility of the fringes and the measured value of $g_S^{(2)}(0)$ slightly lower than 2, to the detector jitter which in our case has a FWHM value of 600 ps. By performing a convolution of an exponentially decaying cosine function with 100% visibility [i.e. $A(\exp^{\frac{-|x-a|}{\tau}}\cos^2(\frac{x-a}{T})+1)$], and the detector jitter function (gaussian curve with FWHM = 600 ps), we get a fit which is plotted in Fig. 4.8 (blue curve). The fringe period obtained from the fit parameter is 353.98 ± 1.50 MHz, which matches closely to the energy separation of the $5P_{1/2}$, F = 2,3 hyperfine levels (361 MHz) [58]. In addition, the decay time-

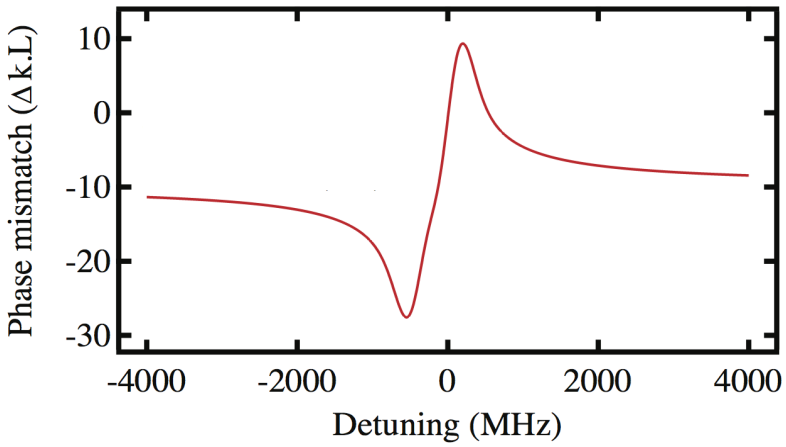

Figure 4.9: The linear phase mismatch is plotted as a function of idler photon detuning Δ_3, with $\Delta_2 = 0$ and $\Delta_1 = 910$ MHz . We observe the phase matching condition i.e. $|\Delta k.L| \leq 1$, to be achieved at a detuning of 540 MHz over a bandwidth of 95 MHz.

constant τ for the fit function is 13.5 ± 1.5 ns, leading to a very narrow spectral width of the signal photons ($\sim$ 20 MHz), which can be explained by calculating the phase matching condition for our FWM process with all beams collinear. To estimate the linear phase mismatch, we model the response function for the real part of the linear susceptibility for a two level system based on [56],

$$\chi_R^{(1)}(\Delta) = \frac{N\mu^2}{3\epsilon\hbar}\frac{\Delta}{\Delta^2+\Gamma^2} \tag{4.11}$$

where $\Delta = \omega_0 - \omega$, is the laser detuning with respect to the atomic transition frequency ω_0, Γ is the natural lifetime of the transition, μ is the dipole moment and N is the atomic density. For the warm Rb system under consideration, atoms moving at a particular velocity 'v' experiences a Doppler shift in the frequency of an incoming photon which is given by $\overrightarrow{k}.\overrightarrow{v}$, where k is the wavenumber. We consider the velocity contribution along the direction of the laser beam and drop the vector notation. At thermal equilibrium, Rb atoms moving with different velocities follow the well known Maxwell's distribution given by,

$$f(v) = \frac{1}{\sqrt{\pi}} exp(-\frac{v}{v_d}^2) \tag{4.12}$$

where v_d is related to the well known width of Doppler broadening 'ω_d' as $v_d = \frac{\omega_d}{k}$. By considering these different atomic species (based on velocity distribution), the real part of the linear susceptibility (subscript R dropped) can be written as a convolution integral,

$$\chi^{(1)}(\Delta) = \int_{-\infty}^{\infty} \frac{N\mu^2}{3\epsilon\hbar} \frac{(\Delta - kv)}{(\Delta - kv)^2 + \Gamma^2} f(v) dv \tag{4.13}$$

The D_1 and D_2 lines of ^{85}Rb have several transitions between their hyperfine levels [58]. For each of these individual hyperfine transitions, we denote, their real linear susceptibilities, relative detunings and transition strengths, by $\chi_i^{(1)}$, Δ_i and s_i respectively. By considering only the most resonant contributions, we can write the complete function for $\chi^{(1)}$ as,

$$\chi^{(1)}(\Delta) = \sum_{i=1}^{n} s_i \int_{-\infty}^{\infty} \frac{N\mu^2}{3\epsilon\hbar} \frac{(\Delta_i - kv)}{(\Delta_i - kv)^2 + \Gamma^2} f(v) dv \tag{4.14}$$

where, n is the total number of near-resonant transitions and Δ is the detuning with respect to the $F = 3 \rightarrow F' = 2$ transition, for $\chi^{(1)}$ measured on the D_2 and D_1 lines. In the limit of $\chi^{(1)}(\Delta) << 1$, we can approximate the corresponding function for the refractive index as,

$$n(\Delta) \approx 1 + \frac{\chi^{(1)}(\Delta)}{2} \tag{4.15}$$

By taking into account the Doppler broadened linear refractive indices for the 795 nm and 780 nm transitions, and assuming a refractive index of 1 for the 776 nm and 762 nm transition (as no population is transferred to the $5P_{1/2}$ and $5P_{3/2}$ levels), we plot in Fig. 4.9, the linear phase mismatch for the FWM process as a function of the idler photon detuning. The phase matching calculation is performed replicating our experimental conditions i.e. $\Delta_1 = 910$ MHz and $\Delta_2 = 0$ using the convention mentioned in Fig. 4.4. The detuning for the idler photon is measured with respected to the $5S_{1/2}$, F = 3 $\rightarrow$ $5P_{1/2}$, F' = 2 transition. As seen in Fig. 4.9, we get a narrow phase matching window of 95 MHz where $|\Delta k.L| \leq 1$, at a detuning of 540 MHz. This of-course, is the upper bound for the phase matching bandwidth and the actual phase matching would be even narrower as suggested by our experimental results. We also see a narrow phase matching region close to resonance (20 MHz) in Fig. 4.9, but the idler photons would be strongly attenuated in this region leading to a lower probability for pair generation.

4.7 CPC pair generation efficiency

To measure the efficiency of pair generation, we plot the coincidences between signal and idler photons by varying the pump power at different power levels of the input field in Fig. 4.10(a). The singles as measured on each SPCM module for the signal and idler photons are plotted in Fig. 4.10(b) and (c) respectively. The detected idler photons are lower by a factor of 5 as compared to the signal photons due to absorption of the idler on the D_1 transition of ^{85}Rb. The coincidences are observed to increase linearly with pump power even in the $\chi^{(2)}_{eff}$ operating regime ($P_i = 500$ nW and pump power = 800 mW), with a CPC pair generation efficiency $\eta_{CPC} = 6.3\text{x}10^{-8}$ coincidences per sec(cps)/input 780 photon measured per kW of

the pump beam. Previous demonstration of CPC have shown an efficiency of $5x10^{-9}$ cps/input photon/kW of pump [4]. As discussed in chapter 1 and 2, the

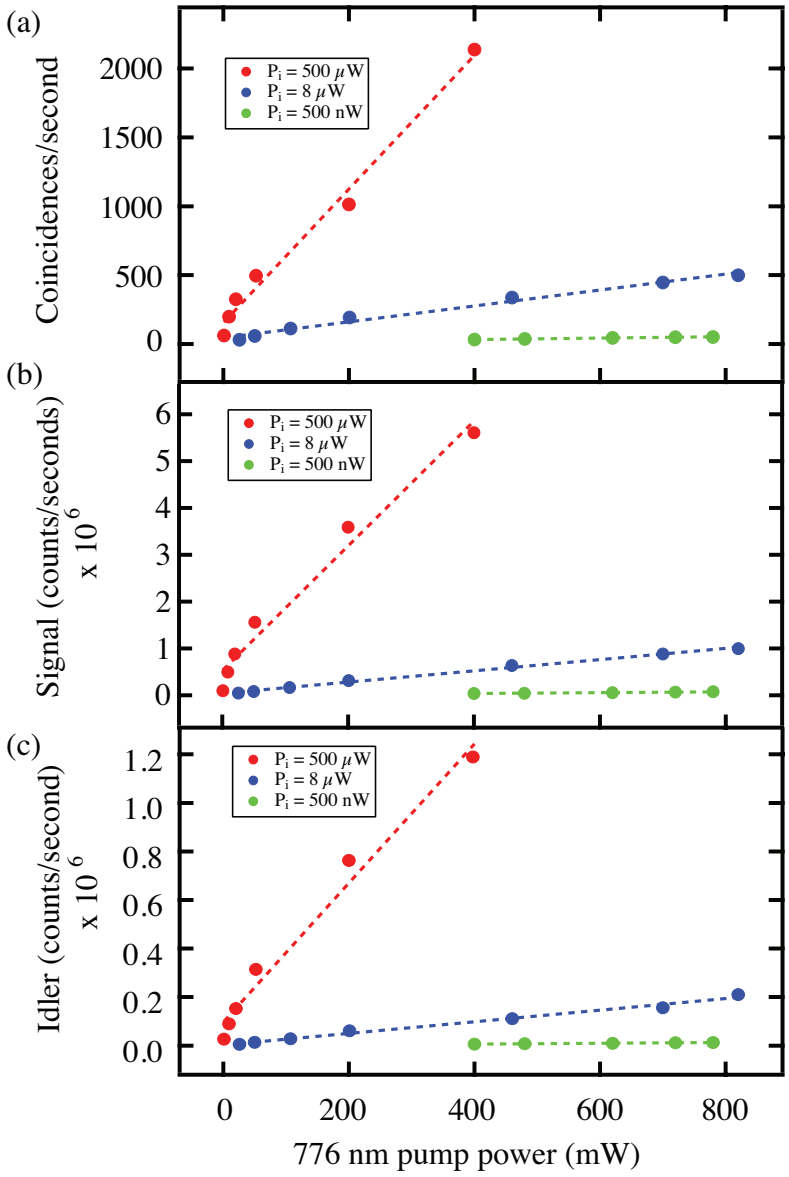

Figure 4.10: Plot of (a) Coincidences between signal and idler photons, (b) SPCM counts of the signal photons and (c) SPCM counts of the idler photons, as a function of pump power, for input field powers of 500 μW (red), 8 μW (blue), and 500 nW (green). We observe the coincidences and singles for both the signal and idler to increase linearly with pump power.

effective third order nonlinearity (γ) of a system is proportional to the number density (N) and interaction length (L), while being inversely proportional to the

optical mode area (A) i.e.,

$$\gamma \propto \chi^{(3)} \frac{L}{A}, \tag{4.16}$$

The atomic number density in our Rb vapor cell maintained at a temperature of 82°C is $\sim 10^{18}$ atoms/m^3 which is obtained by a Voigt function fit to the absorption spectrum. An optical depth of 100 which corresponds to an atomic number density of 2×10^{19} atoms/m^3 [41], can be routinely generated in the Rb-PBGF system. Furthermore the hollow core fiber has a core radius ~ 3 μm and the Rb atoms are known to propagate an overall length of 1 cm in hollow core fiber system [60]. For an interaction length of 2 cm in the vapor cell and a beam waist of 125 μm, we can infer

$$\gamma^{Rb-PBGF} = 2.5\times10^4\times\gamma^{vc}, \tag{4.17}$$

where, $\gamma^{Rb-PBGF}(\gamma^{vc})$ is the effective nonlinearity for the Rb-PBGF system(vapor cell). We know from equation 4.9, the CPC pair generation efficiency $\eta_{CPC} = |\langle 011|\psi(t)\rangle|^2 = \sin^2(\Gamma t)$, which simplifies to $\eta_{CPC} = (\Gamma t)^2$, in the limit $\Gamma t << 1$. From our experiment in the vapor cell, this yields a value of $(\Gamma t)^{vc} = 2.5\times10^{-4}$. Combining equations 4.5, 4.6, 4.8, and 4.17, we can conclude that $(\Gamma t)^{Rb-PBGF} \sim \pi/2$ for 0.25 KW of pump power. This unprecedented increase in CPC pair generation efficiency could help in the realization deterministic photon-pair sources.

4.8 Bandwidth for correlated pair generation

To measure the bandwidth for efficient pair generation, we keep the detuning of the weak input field fixed (910 MHz blue detuned to the $5S_{1/2}$, F = 3 $\rightarrow$ $5D_{3/2}$, F' = 4 transition) and scan across frequencies around the $5P_{3/2} \rightarrow 5D_{3/2}$ transition. As seen in Fig. 4.11, the coincidence counts peak at two photon resonance $\Delta_2 = 0$.

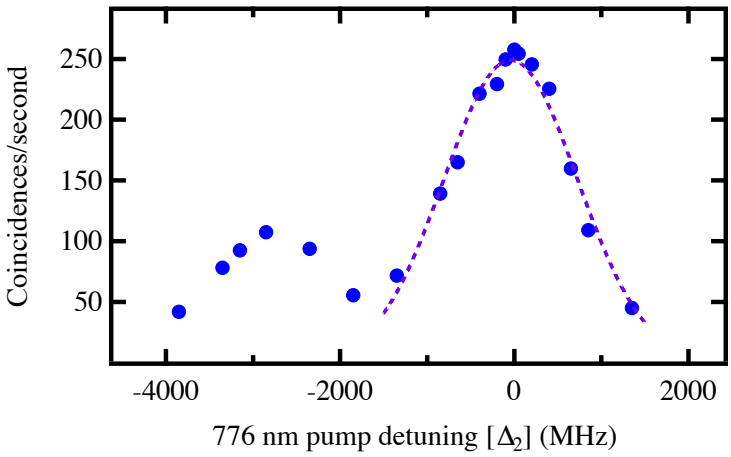

Figure 4.11: Coincidences measured between signal and idler (blue dots) are plotted as a function of two photon detuning (Δ_2) on the $5S_{1/2}$, F = 3 $\rightarrow$ $5D_{3/2}$, F' transition, keeping the weak input field fixed with Δ_1 = 910 MHz. The measured coincidences peak at two photon resonance and a Gaussian fitting function (violet curve) indicates to a bandwidth of 1.5 GHz for the pair generation process. A second peak at $\sim$ -3 GHz, corresponds to pair generation on the $5S_{1/2}$, F = 2 $\rightarrow$ $5D_{3/2}$, F' resonance.

We estimate a bandwidth of 1.5 GHz for the CPC process, which is calculated from a Gaussian fit function (violet curve) to the experimental data. This opens up the possibility of operating with pump pulses about 1 ns long which can be easily implemented using commonly available pulse generators. Operating pulsed should prevent the detection of any noise photons originating from higher order nonlinear process involving the strong pump beam. In addition to the strong peak, we also see a shorter peak feature $\sim$ 3 GHz to the red detuned side. This is due to the two photon resonance condition associated with the $5S_{1/2}$, F = 2 $\rightarrow$ $5D_{3/2}$ transition, as the ground state hyperfine levels $5S_{1/2}$, F = 2,3 have an energy difference corresponding to 3.04 GHz [58].

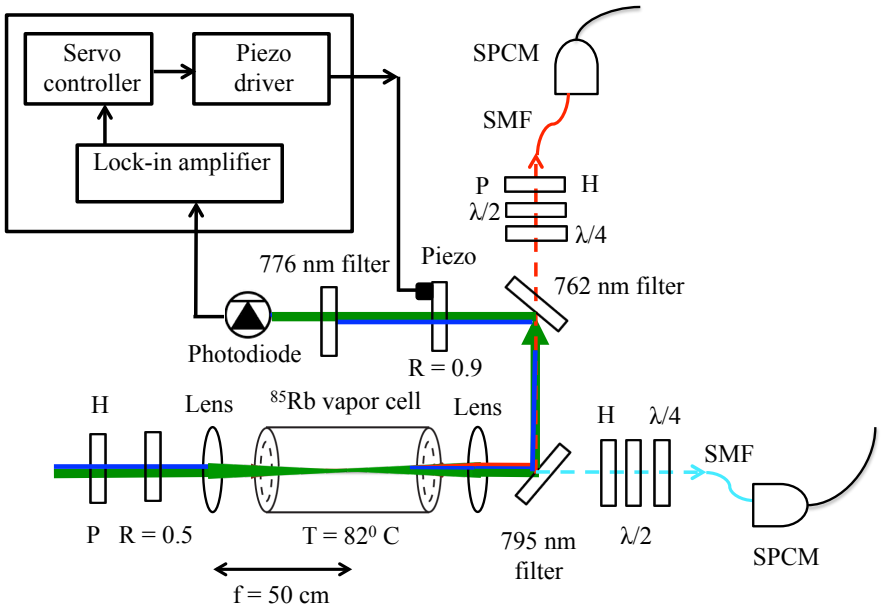

Figure 4.12: A cavity with an input coupling mirror R = 0.5 and an output coupler with R = 0.9 is implemented around the vapor cell. The signal and idler beam are filtered out and only the pump and the weak input are maintained on cavity resonance. The peak of cavity transmission is locked to the pump laser frequency using a lock-in amplifier and a servo controller, which in turn drive the piezoelectric transducer connected to the output coupler. The long term drift of ECDL generating the weak input is small and we manually maintain this laser on cavity resonance.

4.9 Cavity enhanced correlated pair generation

Finally, we explored the idea of increasing the coincidence rates by building a cavity around the vapor cell, resonant with the pump beam and weak input as seen in Fig. 4.12. With a single pass cavity loss of 0.3, we optimized the intracavity power by choosing the input coupling mirror with R = 0.5 and the output coupler with an R = 0.9. The output coupler is mounted on a piezoelectric transducer, continuously modulated by a lock-in amplifier and the resulting error signal is minimized using a servo controller. The cavity is locked to the frequency of the pump beam using active feedback. By leveraging the large bandwidth ($\sim$ 1.5 GHz) of the CPC process and the relative long term wavelength stability of the weak input beam

laser, we manually tune the weak input into cavity resonance till the coincidences between signal and idler are maximized.

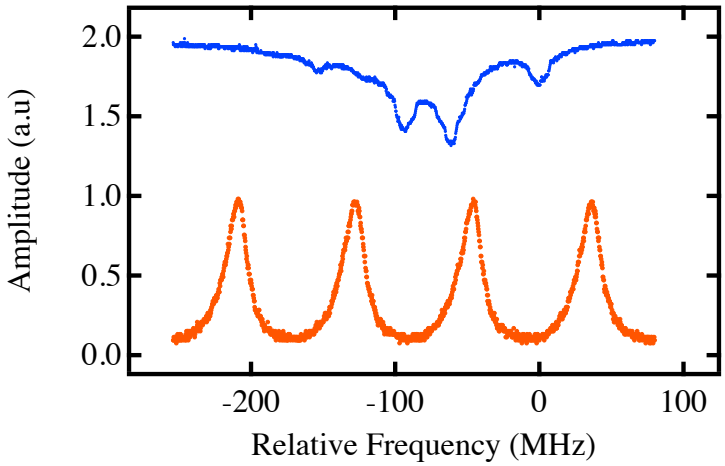

Figure 4.13: We plot the cavity transmission in red as function of input field detuning with respect to the $5S_{1/2}$, F = 3 $\rightarrow$ $5P_{3/2}$, F' = 4 transition. The curve in blue represents the saturation spectrum trace on the D_2 transition and is used for calibration. We measure the free spectral range FSR = 82.3 MHz and a cavity finesse F = 4.5.

Figure 4.13 shows a transmission spectrum of the cavity (red) by scanning across the weak input field frequency, and measured relative to the $5S_{1/2}$, F = 3 $\rightarrow$ $5P_{3/2}$, F' = 4 transition. The saturation spectrum (blue) from a reference Rb vapor-cell on the D_2 transition is also plotted on the same viewgraph for calibration. The experimentally measured free spectral range (FSR) [spacing between adjacent cavity modes] is 82.3 MHz, which is close to the theoretical value of 79 MHz for a 1.9 m long cavity. We measure a cavity finesse F = 4.5 (defined as, F = FSR/Δf, where Δf is the cavity linewidth), which is consistent with the reflection coefficients of the mirrors used. The pump being far off resonance from the D_2 transition, does not suffer any absorptive losses from Rb and the only sources of losses for the pump beam in the cavity are diffraction losses. The losses for weak input are also low, its frequency lying outside the Doppler broadened spectrum (910 MHz blue detuned). With the pump and the weak input on cavity resonance, the observed coincidences

are a factor of 2.3 larger than the case with no cavity for similar power of the pump (800mW) and weak input beam (3 μW). This is consistent with the theoretical prediction of enhancement by a factor of $(\frac{F}{\pi})^2$. In principle, the cavity losses can be reduced by making the cavity smaller in length than the one demonstrated above, which will reduce the diffraction losses and further enhance the coincidences.

4.10 Conclusion

In summary, we report a CPC pair generation efficiency of 6.3x10^{-8} cps/input 780 photon per KW of the pump beam, measured in a warm ^{85}Rb vapor using a diamond level scheme. We also investigate the enhancement in photon-pair generation rates using a cavity and demonstrate a 2.3 times increment in coincidences. Our future work would involve demonstrating CPC with eight orders of magnitude enhancement in pair generation rates, by using the Rb-PBGF system. This would facilitate building efficient quantum logic gates and deterministic photon sources compatible with atomic quantum memories.

CHAPTER 5

ULTRA-LOW POWER NONLINEAR OPTICS WITH RB VAPOR EVANESCENTLY COUPLED TO ON-CHIP SILICON NITRIDE WAVEGUIDES

In this chapter, we demonstrate the interaction between warm Rb vapor and the optical mode of an air-clad silicon nitride (Si_3N_4) waveguide coated with aluminum oxide (Al_2O_3), via evanescent coupling. We observe a greater than 100 times enhancement in device operation lifetime due to the coating which prevents the Rb vapor from corroding the surface. Our results indicate the possibility of using on-chip platforms for performing all-optical modulation at the single photon level, facilitated by the large Kerr nonlinearity of such a Rb-on-chip system.

5.1 Introduction

As explained in chapter 1, optical nonlinearities at the single photon level is a long standing goal in quantum optics. Quantum information processing using photons can be extremely advantageous as, light does not suffer from any appreciable effects of decoherence or propagation losses over large distances, and due to the large carrier bandwidth at optical wavelengths. However, the interaction between photons is weak and any meaningful realization of quantum logic [117], shall require a hihgly nonlinear medium. Our demonstrations in chapters 2 and 4, as well as pioneering experiments in the past [3, 36, 41, 47], have established the feasibility of using alkali vapors confined to the hollow-core photonic band gap structures for quantum computing.

Nanophotonic platforms based on Si_3N_4 waveguides have shown a great po-

tential in developing compact devices for frequency comb generation [118, 119], spectroscopy [120] and quantum information processing [37, 39, 50, 121, 122]. An alternative approach for achieving efficient atom-field interaction, would be to tailor the evanescent field of these nanophotonic structures to interact with alkali vapor [5, 72–75]. If the evanescent field is confined to a very narrow cross-section adjoining the waveguide, the resulting interaction could allow the development of compact and scalable integrated photonic platforms with large Kerr nonlinearities. Furthermore, coupling the warm vapor to the cavity mode of an on-chip micro-ring resonator can lead to operation in the strong atom-cavity coupling regime [27–30], which is otherwise not possible to attain in bulk alkali-vapor cells. In the next section, we shall explain the device requirement and simulations for building a Rb-chip system.

5.2 Device design

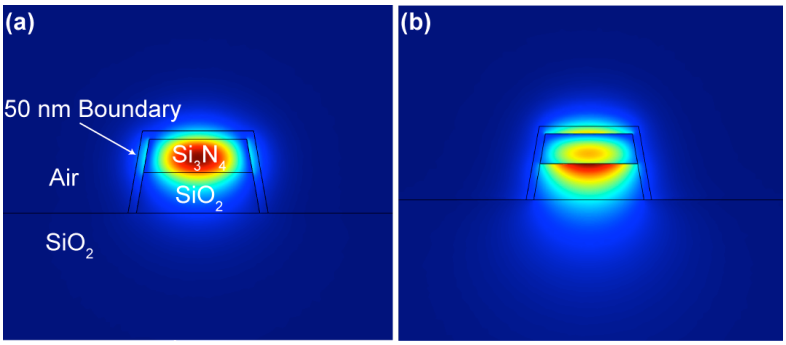

Figure 5.1: Simulations for the Si_3N_4 structures. The waveguides measure 200 nm thick by 600 nm wide with a 10° sidewall angle, and the silicon-dioxide substrate is etched to 250 nm below the waveguide. The 50-nm boundary is an imaginary line included in the simulation for calculation of the confinement of the mode in the air beyond this point. (a) Shows the quasi-TE mode for this structure. The effective index is 1.5933 with a confinement factor of 0.035. (b) Shows the quasi-TM mode for the same structure. The effective index is 1.4728, and the confinement factor is 0.0566.

In order to maximize the optical field interaction with Rb atoms, we design and simulate waveguides over a wide range of dimensions. We use a finite element method (FEM) simulation of various waveguide cross-sections to solve for the waveguide modes at a wavelength of 795 nm (the D_1 transition for Rb). Figures 5.1(a) and (b) show the simulated TE and TM modes for air-clad waveguides respectively. After solving for the modes, we examine the confinement factor [123], which for high index contrast structures gives a value of the intensity in a specified region per unit input power. We look to maximize the confinement factor for the regions beyond 50 nm from the waveguide boundary in order to ensure we are beyond the point where Rb atoms experience dephasing from the waveguide surface. For the supported structures, the minimum thickness of the nitride film that ensures the waveguide supports a quasi-TM mode is 200 nm. We simulate waveguides that have a slight sidewall angle (10°) and are etched 250 nm into the oxide substrate in order to match the fabricated structure. Using a waveguide base width of 600 nm with the aforementioned dimensions, we find that the structure supports the modes shown in Fig. 5.1. The confinement factor in the evanescent region (air) is calculated to be 0.035 and 0.0566 for the TE and TM like modes respectively. We fabricate both straight waveguides and micro-ring resonators based on the above dimensions.

5.3 Chip fabrication

All devices used in this study are fabricated by Prof. Michal Lipson's group at Columbia University. After deposition of a 200 nm thick layer of Si_3N_4, the devices are patterned with electron beam lithography using a maN2403 resist for making the waveguides 600 nm wide, post-exposure bake. Thereafter the devices are etched

in an inductively coupled plasma reactive ion etcher (ICP RIE) using CHF_3/O_2 chemistry. After stripping the resist, we anneal the devices at 1200°C in an argon atmosphere for 3 hours. In order to rectify the mode mismatch when coupling into air-clad device, we clad the tapers with SU-8 2005 resist. After contact lithography, SU-8 is cured in a nitrogen flow oven at 350°C for 1 hour. To prevent corrosive interaction between Rb and the Si_3N_4 surface, we clad the devices with Al_2O_3 and hafnium oxide (HfO_2). Each chip has 5 air-clad straight waveguides and 2 micro-ring resonators. In the next phase, we shall fabricate chips with spiral waveguides, increasing the overall interaction length to about 1 cm.

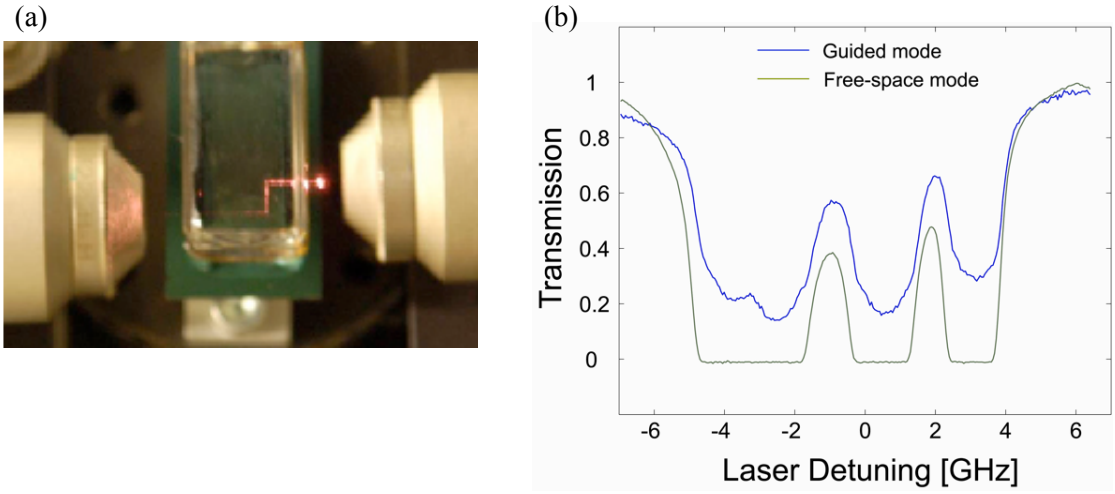

Figure 5.2: (a) View graph of the first generation Rb-chip device, built in our lab, by epoxy bonding a glass dome on top of a large chip. (b) Transmission spectrum of a probe beam evanescently coupled to the waveguide mode (blue) and through the chamber (green). The waveguide mode experiences transit time broadening effects and shifts in the spectrum, due to van der Walls interaction [5].

5.4 Chamber design

The first generation of air-clad devices (uncoated) fabricated with the above dimensions (section 5.2) were tested by releasing Rb vapor in a chamber assembly

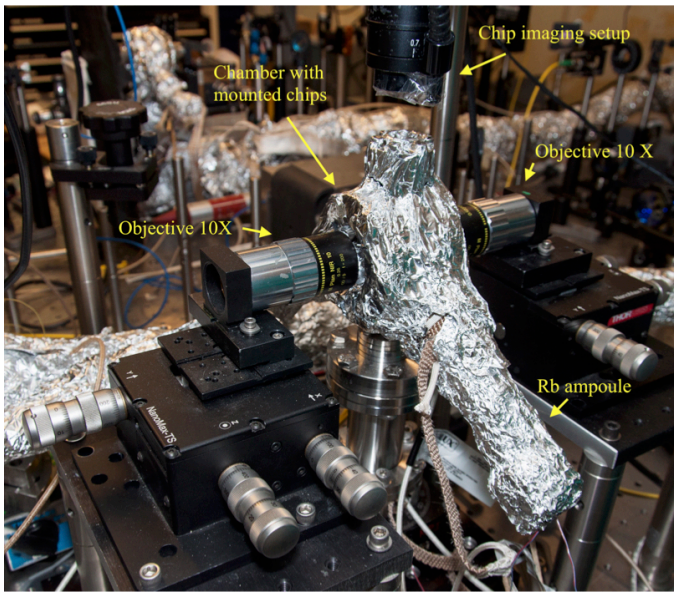

Figure 5.3: A free space probe beam at 795 nm (resonant with the D_1 line of ^{85}Rb) is coupled into the waveguides using 10× objectives. The chips can be imaged from the top viewport using a camera and objective. The chips are mounted on a copper rod inside the chamber, which is insulated from the rest of the chamber using a ceramic sleeve and hence can be temperature tuned independent of the entire chamber. After propagating through the waveguide, the transmission of the probe beam is measured using a photodiode.

developed by epoxy bonding a glass cover slip over the chip surface [Fig. 5.2(a)]. The transmission spectrum for such a device as shown in [Fig. 5.2(b)], demonstrates the interaction of the evanescent optical mode with a dense vapor surrounding the waveguide [5]. The atomic lines appear transit-time broadened due to the narrow waveguide cross-section [124]. A drawback of using these uncoated devices has been the extremely short time scales of operation. After an hour long exposure to Rb vapor, the uncoated devices ceased to function due to a permanent corrosive surface damage caused by the highly reactive Rb vapor. The impurities leaking from the epoxy could also aid the corrosive reaction.

To make a comparative study of the uncoated and coated devices and prevent any leaks in the vacuum, we have characterized our new devices inside a custom

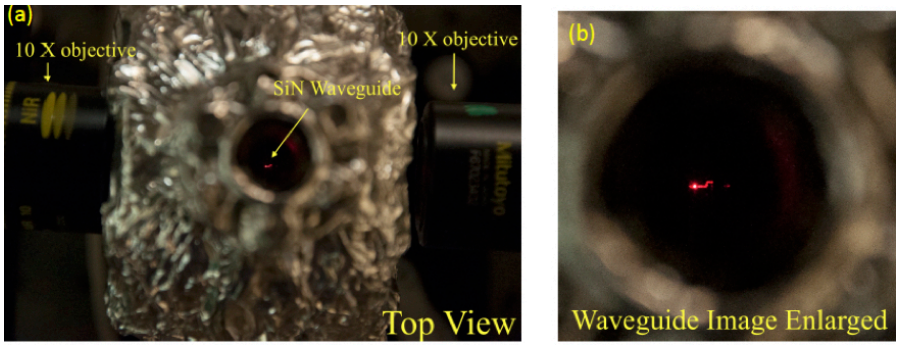

Figure 5.4: (a) Top view of the chamber with the mounted chips. (b) Enlarged image, clearly showing light coupled in a 1 mm long straight waveguide.

vacuum chamber as seen in Fig. 5.3. An ultrahigh vacuum $\sim 10^{-9}$ Torr is achieved by means of an ion pump after baking the chamber for over a month. Once the required vacuum is attained, the Rb ampoule was broken releasing the Rb vapor. The detailed chamber building procedure has been explained in section 1.6. 3 chips (air-clad uncoated, Al_2O_3 coated and HfO_2 coated) are mounted on an insulated copper rod inside the chamber. Light is coupled to the Si_3N_4 straight waveguides and the ring resonators using long working distance Mitutoyo objectives with 10× magnification. The chips can be imaged from top using a microscope and a CCD. Fig. 5.4(a)-(b) shows the top view of the chips as seen from the viewport. In Fig. 5.4(b) we can see light being coupled into the waveguides using the 10× objectives. We achieve an overall coupling efficiency of 11% after accounting for losses. The chamber is maintained at 60°C while the chips are maintained at 100°C, to prevent the Rb vapor from depositing over the waveguide surface.

5.5 Waveguide characterization in a Rb chamber

To characterize the transmission properties of the waveguides, we couple a probe beam scanning across to the D_1 transition (795 nm) of Rb into the waveguide. A

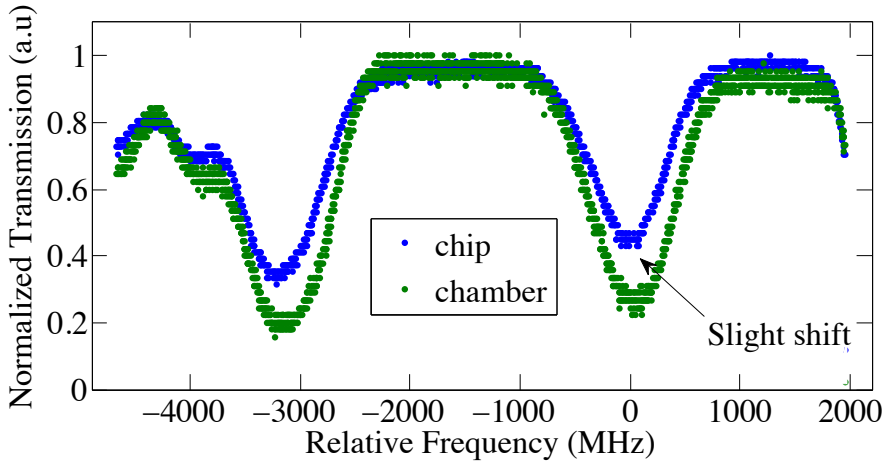

Figure 5.5: Normalized transmission of probe beam coupled into the waveguide (blue) and propagating through the chamber (green). The slight shift in the two spectrum indicates to a van der Walls typer interaction between the Rb vapor and the waveguide surface, which causes a local change of potential and hence a shift in the atomic levels.

reference beam at the same wavelength is sent through the chamber to monitor the density of atoms around the chip. We observe that, uncoated air-clad chips start degrading in the first hour of operation with a drop in transmission from 11% before exposure to around 0.01% after exposure to Rb. In comparison, the chips coated with Al_2O_3 suffer only a $\sim$ 55% attenuation (i.e. 11% $\rightarrow$ 5%) in transmission properties upon exposure to Rb. Furthermore, the Al_2O_3 coated chips last for the entire 15 day period of the study, which represents a $>$ 350 times improvement in operational capabilities over the uncoated chips. Waveguides coated with HfO_2 could not be tested due to the development of a crack during the course of the baking period, and we shall test this coating in future studies. Figure 5.5 shows the transmission spectrum of the probe in the waveguide and chamber. We observe that the spectrum of the probe coupled into the waveguide is slightly shifted as compared to the probe propagating across the chamber [72]. This shift can be attributed to the changes in the energy levels of the Rb atoms caused due to perturbations in local electron potential, by a van der Walls type

interaction between the atoms and waveguide surface. In the above transmission measurement, we were not able to quantify the extent of absorption from atoms interacting with the evanescent field, due to our present chamber design which led to a total vacuum space of 0.5 mm between the viewports of the chamber and the waveguide taper. For a 1-mm long waveguide with only $\sim$ 6% of the total field being evanescent, most of the absorption would result from Rb in the gap region with only a tiny frequency shift seen as a result of van der Wall-type surface interaction. In future Rb-chip chambers, we plan to bond the chips directly to the viewports which shall prevent any free-space between the waveguide taper and the viewport. The measurements performed above, nonetheless do provide evidence for the durability of the Al_2O_3 coated waveguides. Our Rb-chip system with long operational time-scales, shall be extremely useful in the realization of single-photon level experiments which require large averaging times.

5.6 Air-clad micro-ring resonators

We have recently fabricated air-clad micro-ring resonators (ring radius = 115 μm) using the same fabrication procedure as explained in section 5.3 and are coated with a 5 nm thick layer of Al_2O_3 to prevent corrosive damage from Rb. To characterize the transmission properties and measure the Q of the ring cavity at 780 nm, we use a measurement technique as detailed in section 6.5, which employs a commercial Menlo systems comb as a frequency reference. As the source laser at 1560 nm (Toptica continuously tunable diode laser) is scanned between 1530 nm and 1570 nm, the frequency doubled output from a periodically poled lithium niobate (PPLN) crystal scans between 765 nm and 785 nm [poling period optimized for second harmonic generation]. During each instance of the scan, the laser frequency

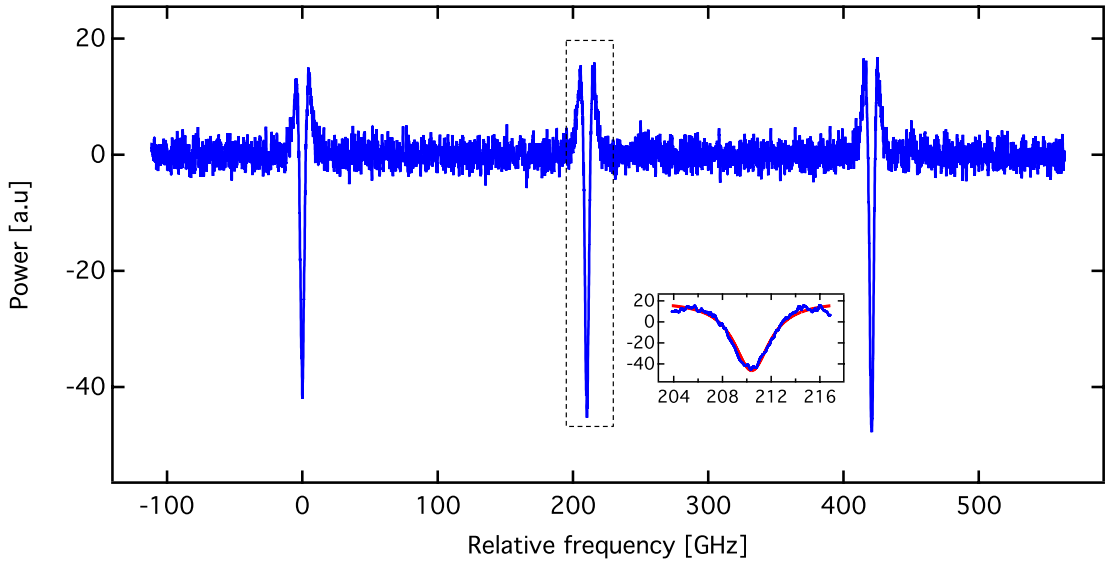

Figure 5.6: Transmission scan of the air-clad ring resonator by continuously tuning the laser across three cavity resonances. This broadband scan is achieved by frequency doubling a tunable laser at 1550 nm and using the doubled output for scanning the ring-cavity at near-visible wavelengths around the Rb D_2 transition. We measure a free spectral range of 210 GHz and a cavity line-width of 3.56 GHz, which leads to high quality factors Q $\sim 107,000$.

is continuously measured using a beat note measurement with the pre-calibrated Menlo comb. Figure 5.6 shows transmission spectrum of the device as a function of relative frequency, by scanning the laser across three cavity resonances at 780 nm. From the transmission spectrum we determine the free spectral range (FSR) [spacing between adjacent cavity modes] of the resonator to be 210 GHz, which is in close agreement to the theoretical FSR for a ring cavity with radius = 115 μm. The sharp bending features close to the zero line for each peak is due to a low-pass filtering effect of processing the raw data, which is limited by sharp interference fringes appearing from back reflections. The microresonator also has a characteristic quality factor 'Q value' which determines the time for which energy can be stored (or rate of dissipation) in the ring cavity. Mathematically this is represented as $Q = f_0/\Delta f$, where Δf is the width of the resonance and f_0 is the frequency about which the mode is centered. As seen in the inset of the transmis-

sion scan shown in Fig. 5.6, we fit a Lorentzian lineshape to the cavity mode in the middle (centered at about 210 GHz) and estimate the line width to be around 3.56 GHz, which corresponds to a Q $\sim 107,000$ for the air-clad ring cavity. The high Q value should play a substantial role in our efforts to demonstrate CPC using the Rb-chip system which has been explained in section 7.2.

5.7 Summary

In conclusion, we have demonstrated > 300 times improvement in Rb-chip device operation lifetime by coating the waveguide surface with a thin layer of Al_2O_3. After the intial reaction between Rb and the chip surface (which reduced the waveguide transmission to 5%), we observed no appreciable degradation in the device transmission properties over the duration of study. We have also successfully fabricated air-clad Si_3N_4 microresonators capable of evanescently coupling to Rb vapor with Q values exceeding 100,000. As a next step we plan to implement all optical modulation at the single photon level [60] and CPC, using Rb vapor coupled to the high Q air-clad microresonator.

CHAPTER 6

BROADBAND NEAR-VISIBLE PARAMETRIC SOURCES USING HIGHER ORDER TRANSVERSE MODES IN SILICON NITRIDE MICRORESONATORS

In this chapter, we discuss a novel method to achieve broadband phase matching for third order nonlinear ($\chi^{(3)}$) parametric processes in the near-visible by engineering anomalous dispersion for higher order modes in Si_3N_4 microresonators. We describe the practicality of our scheme by demonstrating broadband FWM via $\chi^{(3)}$ type interactions (also known as parametric frequency comb generation) spanning over 45 THz at near-visible wavelengths. Our demonstration opens interesting possibilities of developing broadband single photon sources and squeezed states, in the near-visible. Furthermore, achieving a fully mode-locked frequency comb would be a significant step towards building on-chip ultrafast laser sources at visible wavelengths (e.g. analogue of the Ti:S laser) which would have tremendous applications in on-chip ultrafast spectroscopy and precision metrology.

6.1 Introduction

On-chip QIP has attracted significant interest lately, due to the relatively small footprint of the devices and cavity enhanced nonlinear interaction in chip-based micro-resonator devices, which allows for efficient device operation at low power levels and scalability. Secondly, it is also possible to optimize device operation in a particular wavelength regime of interest by dispersion engineering, achieved by accurately optimizing the waveguide dimensions. By designing waveguides with appropriate dispersion parameters, quantum correlated photon pairs have been

demonstrated at telecom wavelengths in a variety of on-chip platforms based on, silicon [48, 108, 109, 125], hydrogenated amorphous silicon [38, 51], chalcogenides [107] and Hydex glass [49].

Silicon nitride (Si_3N_4) has shown promise as a platform for on-chip quantum-photonic applications largely due to, its compatibility with CMOS fabrication process [126], high quality factors (37 million) achievable though recent developments in fabrication techniques [71], and the large effective Kerr nonlinearity. Previously, octave spanning frequency combs have been demonstrated in Si_3N_4 at telecom wavelengths [118,119], leveraging the anomalous dispersion of fundamental waveguide modes leading to broadband phase matching for the underlying four-wave mixing (FWM) process. This broadband phase matching at telecom has also been used to demonstrate ultra-bright quantum correlated photon pair generation [39] and on-chip squeezing [121] in Si_3N_4 microresonators by FWM.

Developing broadband and tunable single photon sources in the near-visible could serve as an important resource for QIP due primarily to the availability of highly efficient and low-cost single photon detectors in the wavelength regime between 400 nm - 950 nm. Secondly, as mentioned in chapter 4, quantum memories required for storing quantum information are also most efficiently implemented using atoms [44–47] which have storage levels in the visible frequency range. In addition, we have also demonstrated in the earlier chapters that alkali vapors in confined geometries (e.g. the Rb-PBGF and Rb-chip system) have a large effective Kerr nonlinearity but are limited in band-width due to narrow atomic transitions. Towards this end, spectrally narrow single photon generation in the visible can be extremely advantageous to achieve single-photon level nonlinear interaction in the Rb-PBGF and Rb-chip system.

A major challenge to extend the range of parametric FWM (the underlying process for both photon-pair and frequency comb generation) to visible wavelengths, has been that conventional dispersion engineering [127] does not produce anomalous group velocity distribution (GVD) which is desirable to achieve phase matching over a large bandwidth. Recently, there have been several approaches for anomalous dispersion engineering in the visible regime. Frequency comb generation via FWM in the near-visible has been demonstrated in a CaF_2 whispering gallery mode resonator using higher order mode excitation [128], and in a thin silica micro-bubble resonator [129]. However, the maximum comb bandwidth achieved was 10 nm [129]. Alternatively, parametric wave generation in the visible have also been observed via, second-harmonic, sum-frequency and third-harmonic generation from a near-infrared comb in Si_3N_4 and AlN microresonators [130–132]. There have also been proposals to achieve anomalous dispersion in the visible by mode coupling between two micro-ring resonators [133], with an experimental demonstration at telecom [134]. In the next sections, we describe the conditions required for broadband four-wave mixing, followed by a detailed description of our approach to achieve anomalous dispersion for higher order modes in the visible regime.

6.2 Dispersion engineering of higher-order waveguide modes

We explore the possibility of utilizing a single CW pump beam for generating correlated photon pairs and a broadband frequency comb at near-visible wavelengths, by the process of FWM in a Si_3N_4 microresonator. The phase matching

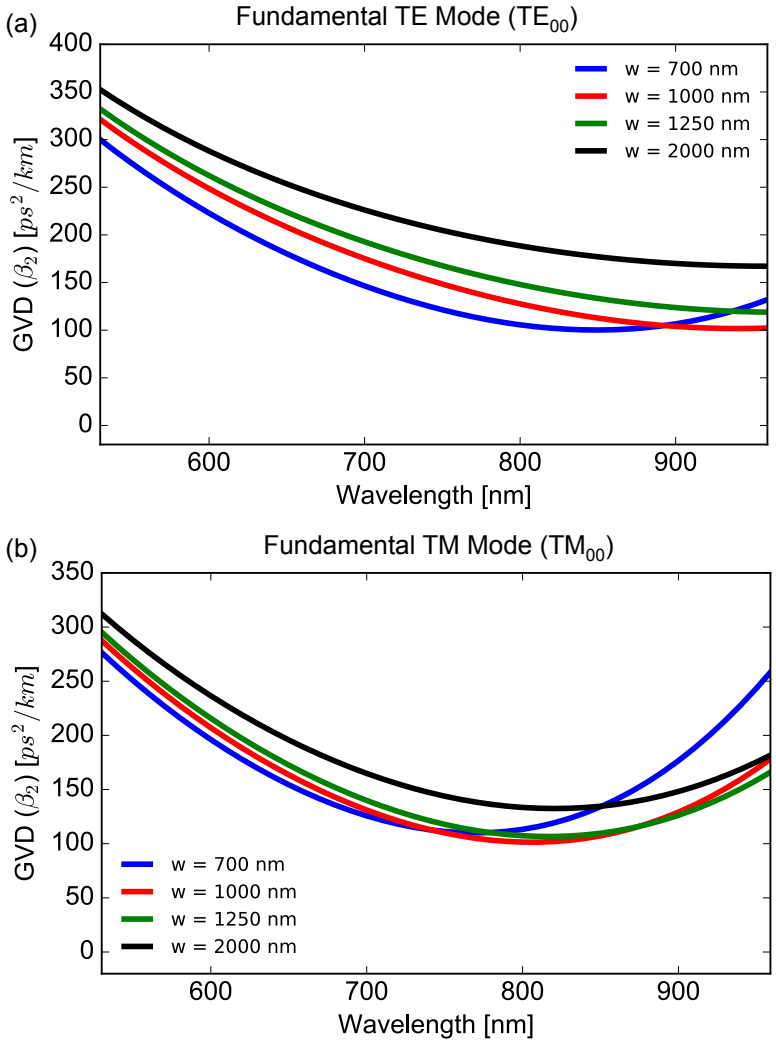

Figure 6.1: GVD for the (a) TE_{00} and (b) TM_{00} mode are plotted as function of wavelength for a 440 nm tall waveguide and widths ranging between 0.7 μm - 2 μm. We observe normal GVD for both TE and TM modes.

condition for degenerate FWM depends on even ordered dispersion parameters evaluated at the pump frequency [135]. The pump must experience an anomalous GVD to achieve a large continuous bandwidth for FWM on either sides of the pump frequency (i.e. $\beta_2 \leqslant 0$) [127, 135, 136]. In addition, optimal performance also requires the fourth order dispersion parameter β_4 to be positive [136–138]. To achieve anomalous dispersion for the ring-cavity modes, we simulate the mode-profile of the guided modes in the bus waveguide and ring using a finite-element

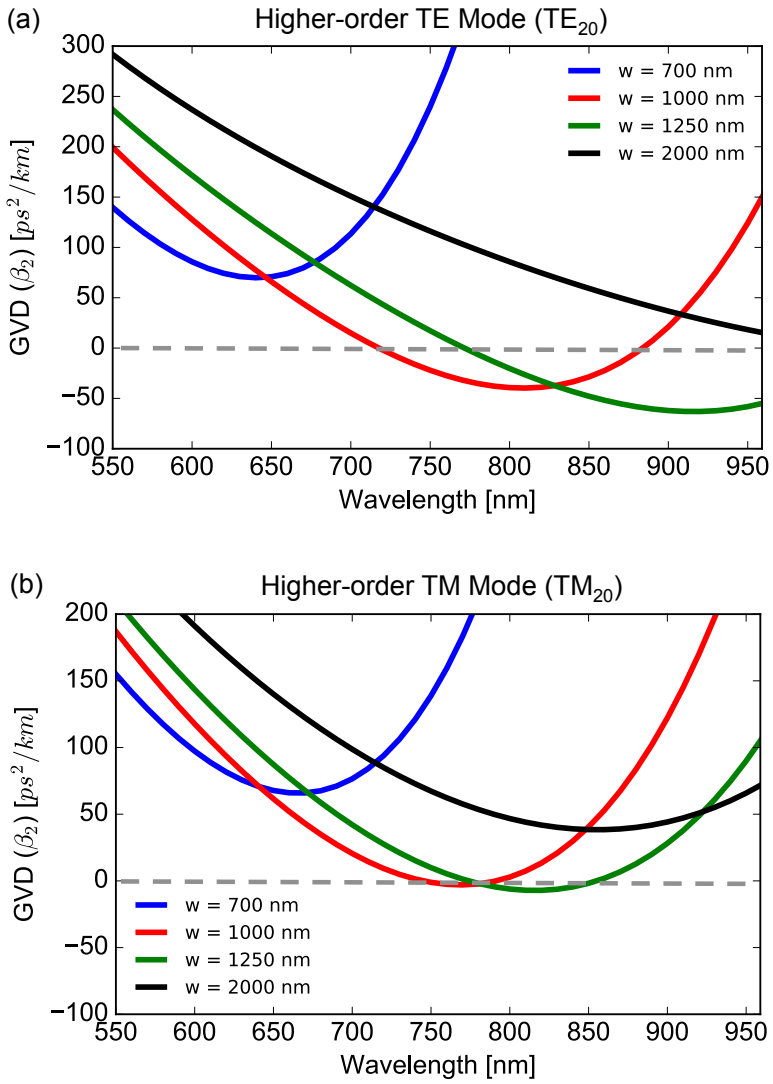

Figure 6.2: GVD for the (a) TE_{20} and (b) TM_{20} mode are plotted as function of wavelength for a 440 nm tall waveguide and widths ranging between 0.7 μm - 2 μm. We observe anomalous GVD for both TE and TM modes for waveguides with widths 1 μm and 1.25 μm in the near visible wavelength range.

method (FEM) implemented with COMSOL multiphysics package to calculate the effective refractive index (n_{eff}) of the optical mode as a function of input wavelength (λ). We numerically estimate the derivatives for n_{eff} and focus on the second and the fourth order derivatives, which correspond to the β_2 and the β_4 terms respectively. We simulate the mode profiles for waveguides with different

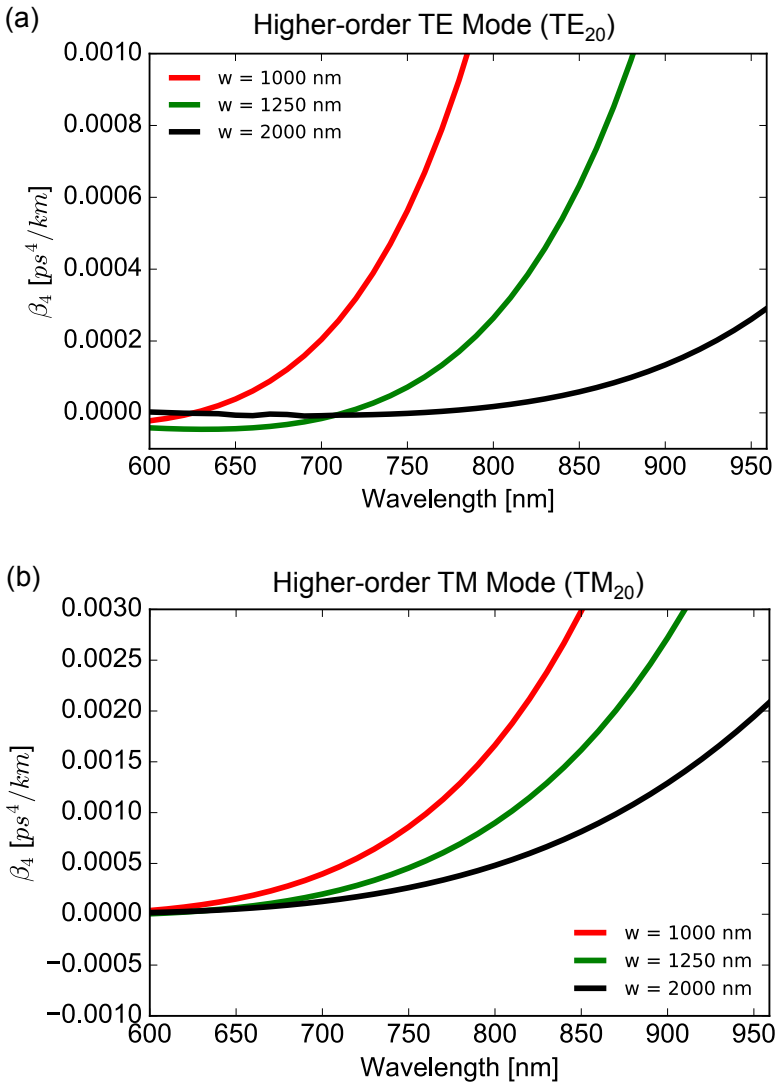

Figure 6.3: Fourth-order dispersion (β_4) for the (a) TE_{20} and (b) TM_{20} mode are plotted as function of wavelength for a 440 nm tall waveguide and widths ranging between 1 μm - 2 μm. We observe the β_4 values for both TE and TM modes to be positive in the wavelength range around 700 nm - 900 nm.

widths and height. Figure 6.1 shows the GVD values as function of wavelengths for the fundamental TE_{00} and TM_{00} modes of a 440 nm tall waveguide at different widths. We clearly observe that the waveguide dispersion is normal in the near visible wavelengths i.e. $\beta_2 > 0$ for both the TE_{00} and TM_{00} modes. In comparison, we observe that the higher-order TE_{20} and TM_{20} modes for waveguides with the same dimensions [those used in Fig. 6.1(a) and (b)], show anomalous dispersion

i.e $\beta_2 < 0$, as is seen in Fig. 6.2(a) and (b). The TE_{20} modes are more anomalous than the TM_{20} over the same wavelength range. In addition, we plot the β_4 values for the TE_{20} and the TM_{20} modes in Fig. 6.3(a) and (b) and observe that $\beta_4 > 0$ for the near-visble wavelength range of 750 nm - 950 nm. The above simulations indicate that higher-order mode excitation in 440 nm tall waveguides with widths between 1 μm - 1.3 μm could lead to broadband phase matching for FWM in the wavelength range around 700 nm - 900 nm, as both the required conditions mentioned in the previous section (i.e. $\beta_2 < 0$ and $\beta_4 > 0$) are satisfied. In our experiments, we have used 440 nm tall and 1.3 μm wide microresonators for generating frequency combs by FWM between 710 nm - 830 nm, to demonstrate the feasibility of our scheme (refer section 6.6).

6.3 Higher-order mode excitation via mode conversion

In the previous section, we saw that TE_{20} mode has the largest anomalous GVD in the near-visible wavelength range. As the input pump laser is chiefly coupled to the TE_{00} mode of the bus waveguide, it becomes necessary to engineer waveguides for coupling pump power in to the TE_{20} mode of the microresonator. We use the principle of mode conversion which was pioneered to obtain mode-division multiplexing on a silicon chip [139], to efficiently excite the TE_{20} mode in the ring-cavity. The concept of mode conversion has also been used to generate entangled photons using coupled waveguides [122]. The conversion is optimal if the modes in both waveguides are phase-matched, i.e. their n_{eff} is the same. Since the n_{eff} is a function of the waveguide dimensions and transverse mode family, we need to have different dimensions in order to match the fundamental mode in the bus waveguide to the higher order mode in the ring. Since the height of the bus

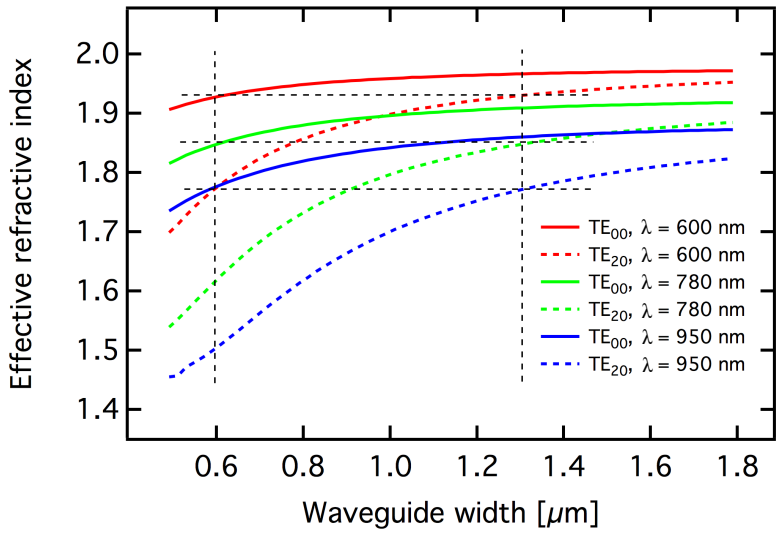

Figure 6.4: We plot the effective refractive index (n_{eff}) for the TE_{20} and TE_{00} modes as function of the waveguide width, with height maintained at 440 nm. It is observed that n_{eff} for the TE_{20} mode of a 1.3 μm wide waveguide matches the n_{eff} for the TE_{00} mode of a waveguide with width = 0.6 μm [where the horizontal dotted lines intersect the vertical], at wavelengths λ = 600 nm (red), 780 nm (green) and 950 nm (blue).

waveguide and the ring-cavity is the same, we use a bus waveguide with a smaller width than the microresonator to achieve the desired phase matching. Figure 6.4 shows simulation results for the effective refractive index plotted as a function of the waveguide width, at input wavelengths of 600 nm (red), 780 nm (green) and 950 nm (blue) for the TE_{00} and TE_{20} modes. In all cases we maintain a constant waveguide height of 440 nm. As indicated by the horizontal and vertical dotted lines in Fig. 6.4, we observe that the n_{eff} for the TE_{00} mode in a waveguide of width = 0.6 μm, matches the n_{eff} for the TE_{20} mode in waveguide of width = 1.3 μm.

The matching of refractive indices is obtained over a broad range of wavelengths spanning 600 nm - 950 nm for the combination of waveguide widths discussed above. Using the same technique, we can select different combinations of waveguide dimensions to obtain efficient mode conversion. Based on our simulation results,

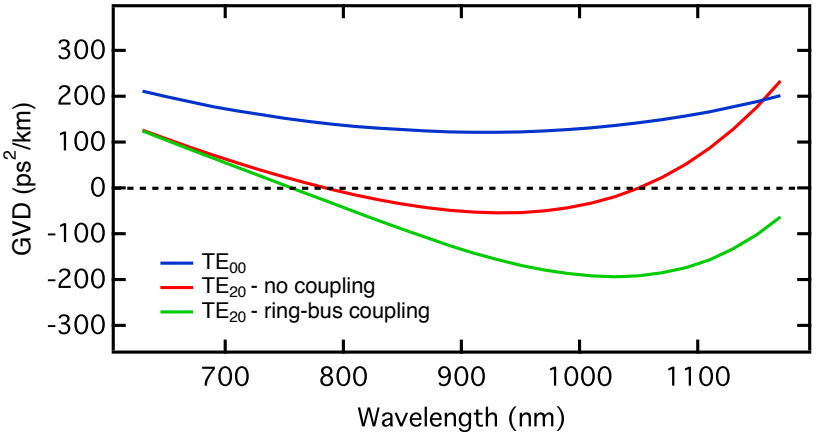

Figure 6.5: GVD simulation for the TE_{00} mode (blue), TE_{20} mode without including coupling (red), and TE_{20} mode by including the mode conversion effect from the bus to the ring (green). In all cases, the microresonator is 1.3 μm wide and 400 nm tall. It is observed that the mode coupling effect broadens the wavelength range of anomalous dispersion for the TE_{20} mode.

we fabricate ring-resonators with widths = 1.1 μm, 1.3 μm, and 1.4 μm and design their corresponding bus waveguides to be $\sim$ 0.6 μm wide. The microresonators with width = 1.3 μm yield the best results for broadband FWM, and henceforth we shall focus on them for all measurements. Taking into account, the effect of mode coupling between the bus waveguide and the ring (coupling gap = 200 nm), lead to further modifications in the GVD. This is shown in Fig. 6.5, where we plot the GVD for the TE_{20} mode, with (blue) and without (green) the coupling effect of the bus waveguide for a microresonator with width = 1.3 μm. In addition, we also plot the GVD for the TE_{00} mode which is normal in the visible regime. The coupling between the bus and the ring leads to a larger anomalous GVD for the TE_{20} mode at near-visible wavelengths which results in broadband FWM over an extended frequency range as demonstrated in our present work.

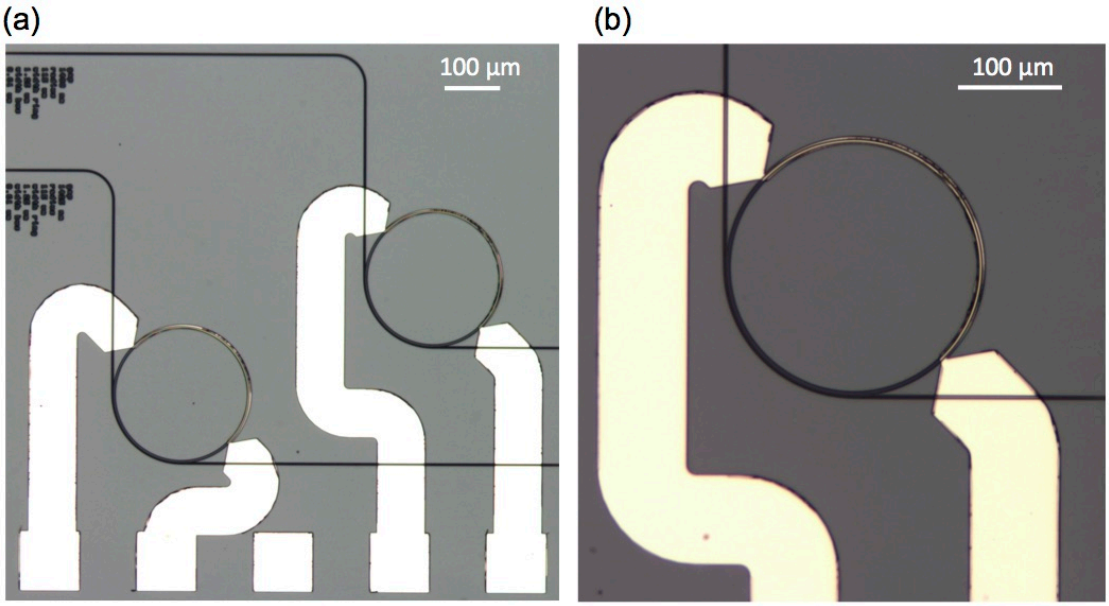

Figure 6.6: (a) Microscope image for the 440 nm tall and 1.3 μm wide Si_3N_4 microresonator. Platinum microheaters (seen as rectangular pads in the image) enable precise temperature control of the ring, which helps in tuning the laser into the cavity mode. (b) Enlarged image of the microresonator shown in (a).

6.4 Chip fabrication and design

All waveguides used in this study were fabricated using a procedure that has been detailed in previous works [71, 140], which achieve ultra-high loaded Q values by improving the quality of the etching process. A 4-μm thick SiO_2 layer is grown on a silicon wafer, which acts as a cladding at the bottom. Thereafter, a layer of Si_3N_4 is deposited on this oxide layer by low pressure chemical vapor deposition (LPCVD). Once the nitride layer is smoothened by chemical mechanical polishing, a hard mask of SiO_2 is deposited using plasma enhanced chemical vapor deposition (PECVD). The devices are patterned using electron beam lithography and the nitride film was etched using CHF_3, O_2 and N_2. To remove any residual N-H bonds in the Si_3N_4 film, the device is annealed in argon atmosphere at 1200°C for about 3 hours. Finally, the devices are clad with a 500 nm thick high temperature SiO_2,

followed by a 2.5 um thick layer of SiO_2 using PECVD. Figure 6.6(a) shows two microresonators used in our work and fabricated with the above method [Fig. 6.6(b) shows an enlarged image]. Platinum microheaters are patterned on top of the microresonator to thermally control the refractive index of Si_3N_4 and hence tune the ring in and out of cavity resonance at a fixed laser wavelength. By using a very precise current control, it is also possible to locally stabilize the temperature of the waveguide against external fluctuations in temperature and air flow, in the surrounding laboratory area.

6.5 Microresonator transmission and GVD measurement

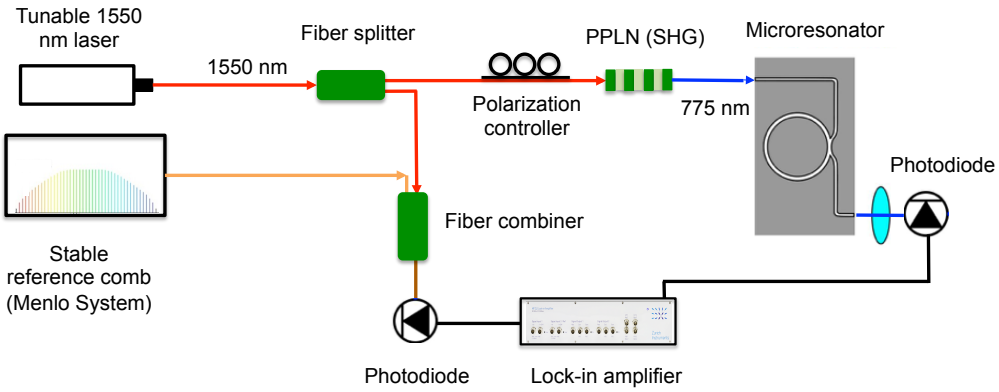

Figure 6.7: A tunable laser at 1550 nm is coupled in to the PPLN waveguide for generating a frequency doubled output in the near-visible by second harmonic generation (SHG). This near-visible output is used as a tunable laser source between 765 nm - 805 nm and is coupled in to the microresonator. A part of the input laser beats with a commercial reference comb system (Menlo systems) and the photodiode response is used to calibrate the wavelength of the laser source as it scans across the cavity modes.

Measuring the GVD for the microresonator, requires a highly accurate measurement of the FSR for the ring cavity modes (precision of $>$ 10 MHz). To measure the absolute wavelength of the laser as it scans across different microres-

onator modes, we use a measurement technique [141] employing a highly stable commercial Menlo systems comb with a 250 MHz spacing between adjacent comb teeth. Our measurement scheme is shown in Figure 6.7. Due to the unavailability

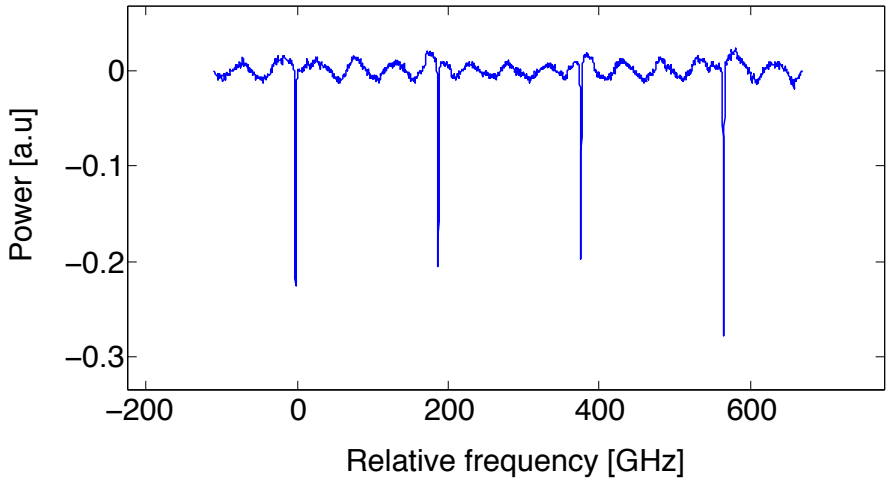

Figure 6.8: Microresonator transmission as the input laser is scanned across four adjacent cavity modes at 780 nm.

of a mode-hop free tunable laser at wavelengths around 780 nm (required tuning range $>$ 20 nm), we build a custom laser source using a 0.5 mm long PPLN crystal (Covesion), with poling periods optimized for second harmonic generation (SHG). The extremely short length of the PPLN makes phase matching requirements less stringent as compared to a longer crystal, which allows SHG over a broad range of wavelengths at constant temperature and by operating in just one waveguide. The short length leads to a rather poor SHG efficiency with only 20 nW of output generated at 780 nm for about 10 mW of input 1560 nm CW power. The nW level frequency doubled laser is detected using a sensitive photodiode (NewFocus 2151). We employ a continuously tunable Toptica laser, which can mode-hop free scan between 1530 nm - 1610 nm. As seen in Fig. 6.7, the output of the laser is split using a 50:50 fiber beam-splitter, with one output port coupled into a PPLN waveguide. The PPLN waveguide frequency doubles the telecom source to wavelengths ranging

between 765 and 805 nm. The second output port is combined with the output of the Menlo comb system and the beat note generated by the photodiode is sent to a fast lock-in amplifier system (Zurich Instruments, 50 MHz). The lock-in amplifier contains two demodulation channels and we set them at a frequency of 25 MHz and 100 MHz respectively. This implies that the beat note (say ω_0) generated by the scanning laser with any given comb tooth, leads to the creation of four side bands at $\omega_0 \pm 25$ MHz and $\omega_0 \pm 100$ MHz. This creates four markers for each comb tooth. The transmission spectrum for the microresonator is recorded as a function of elapsed time for the laser scan. We simultaneously measure the four frequency markers created by the lock-in amplifier for the laser, at the same time-stamps as those used for the transmission scan. We then fit a 5^{th} order polynomial to the individual frequency markers and get an accurate estimate of the actual frequency of the laser at each time stamp. The final processed transmission spectrum for the 440 nm tall and 1.3 μm wide micro-resonator is plotted as a function of relative frequency in Fig. 6.8, for a TE polarized input laser. Four adjacent cavity modes are shown, with the input laser scanning continuously between 765 nm - 805 nm. We measure the difference between successive cavity modes and estimate a FSR

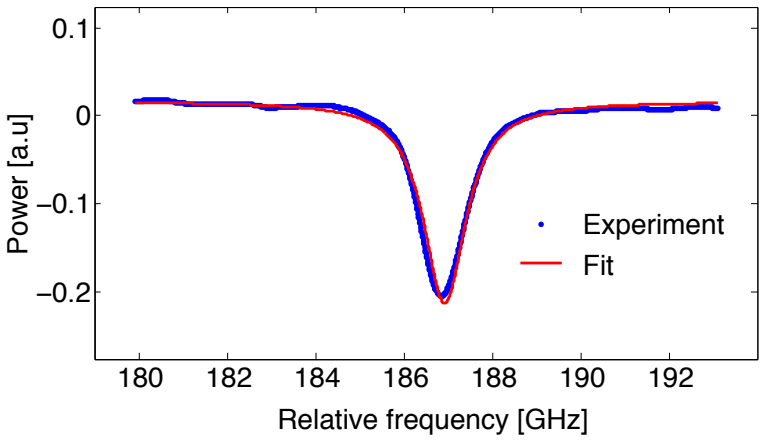

Figure 6.9: Lorentzian fit (red) to the cavity mode at 186 GHz in Fig. 6.8 (blue), indicates a linewdith of 1.2 GHz and a Q value of 330,000.

of 188 GHz, which is consistent for a ring with a 115-μm radius. To measure the cavity line-width, we select the second mode centered around 186 GHz in Fig. 6.8 and fit a Lorentzian line shape to it as seen in Fig. 6.9. The estimated line-width from the fit is 1.2 GHz which corresponds to Q value of $\sim$ 330,000. The GVD for a ring cavity is given by the expression [141],

$$\beta_2 = \frac{-\lambda^2}{2\pi c L} \frac{\delta \frac{1}{FSR}}{\delta \lambda} \tag{6.1}$$

where, L is the length of the cavity and λ is the wavelength of the laser field. To

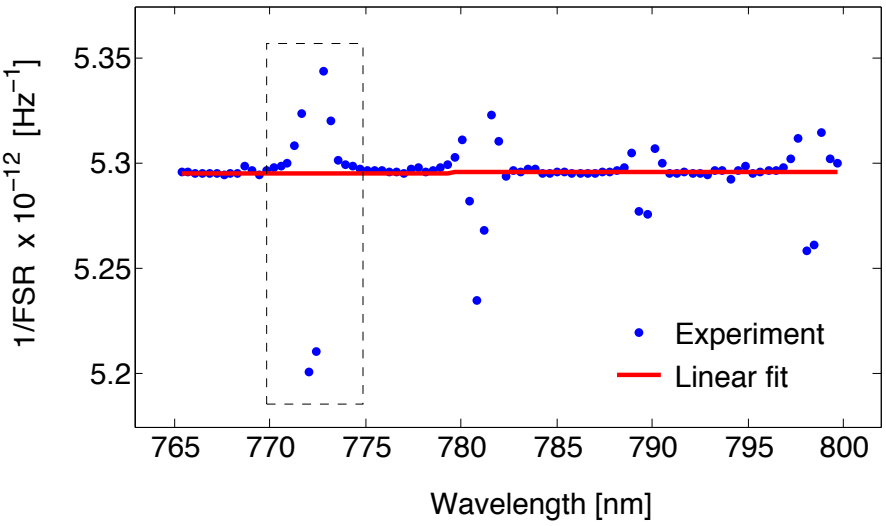

Figure 6.10: Plot of 1/FSR (blue) versus wavelength, for the microresonator, as the PPLN sources scans between 765 nm and 800 nm. The sharp deviations in FSR (dotted box region) show the presence of a local polarization mode-crossing. Excluding the crossings, we can fit a straight line (red) with a positive slope to the rest of the data points, which indicate towards anomalous GVD for the microresonator mode in the near-visible wavelength range.

experimentally calculate the GVD for the microresonator, we used a peak search algorithm to find the FSR as a function of the wavelength. Figure 6.10 plots 1/FSR as function of the wavelength. We observe local kinks in the FSR (e.g the box region in Fig. 6.10) due to polarization mode-crossing [142] which creates local perturbations in the dispersion due to strong modal-coupling, resulting in a strong

pushing (pulling) effect on the interacting modes. This strong mode coupling results in a local FSR change over a narrow spectral range. By excluding the regions of mode crossings, we perform a linear fitting for all the other points which results in a straight line with a positive slope. Inserting the slope of this linear fit in equation 6.1, yields β_2 = -13 ps^2/km which is similar to the value of anomalous GVD predicted by our theoretical simulations in Fig. 6.5 for wavelengths around 780 nm.

6.6 Near-visible comb generation via FWM

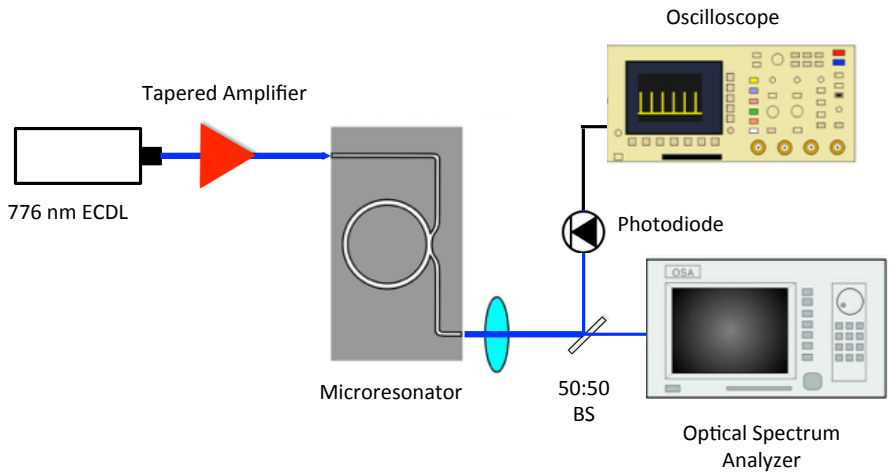

Figure 6.11: TE polarized output from an ECDL (Toptica DL 100) at 776 nm is amplified using a tapered amplifier (Toptica Boost TA pro) and coupled in the bus waveguide using a lensed fiber. The collimated output is split using a 50:50 free space beam splitter and sent to a photodiode to monitor the transmission, and an optical spectrum analyzer to measure the comb spectrum.

To demonstrate broadband FWM, we select a 440 nm tall and 1.3 μm wide microresonator with anomalous GVD for the TE$_{20}$ mode, which has also been experimentally measured in the previous section. The coupling gap between the bus waveguide and the ring-cavity is 200 nm. A strong TE polarized pump laser is

coupled into the bus waveguide using a lensed fiber as seen in Fig 6.11. The pump laser used in this experiment is a Toptica DL-100 ECDL, amplified to 1 W using a tapered amplifier. The laser has a modest mode-hop free tuning range of 10 GHz and hence we use on-chip platinum microheaters [see Fig. 6.6] for tuning the cavity into resonance with the laser. The light from the output taper is collimated using a 0.5 NA objective and is split using a 50:50 beam splitter. The transmission through the cavity is measured on a photodiode, while the spectrum of the output beam is monitored using an optical spectrum analyzer (OSA). By coupling a power of 100 mW in the bus waveguide at a pump wavelength of 776 nm, we observe the

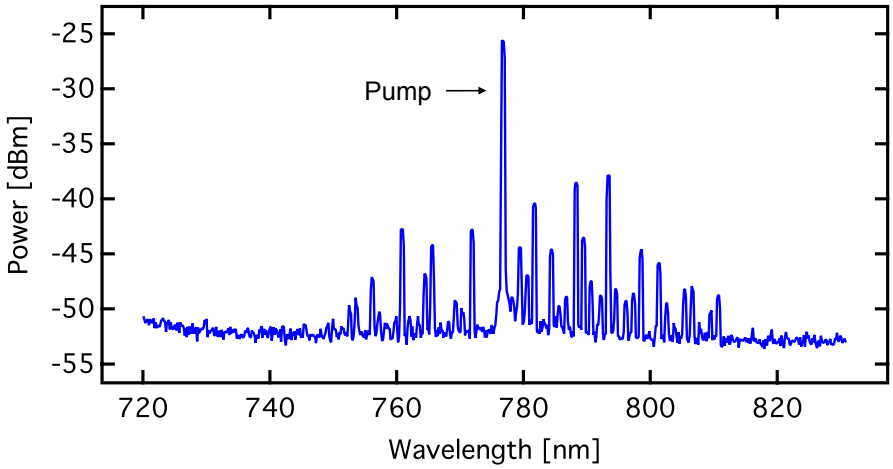

Figure 6.12: Generated comb spectrum, with a pump beam at 776 nm and 100 mW of pump power coupled in the bus waveguide. We observe >40 comb lines in the wavelengths between 730 nm and 820 nm.

generation of > 40 comb lines between 730 nm - 820 nm by FWM. The OSA trace is shown in Fig. 6.12. To our knowledge this the broadest comb demonstrated in the wavelength range around 780 nm, spanning 45 THz. A dense comb exists between 750 nm and 820 nm while comb lines stretch as far out as 730 nm to the blue detuned and 820 nm to the red detuned side of the pump. Additionally, we also show comb spectra from adjacent cavity modes and clearly observe the existence of comb lines at wavelengths as low as 710 nm [Fig. 6.13(b)]. The generation of

comb lines between 710 nm - 820 nm indicates the broad wavelength range over which phase matching can be achieved for FWM in the near-visible. In addition, we also observe that combs lines are generated across the D_1 and D_2 transitions of highly nonlinear alkali elements like Potassium and Rubidium.

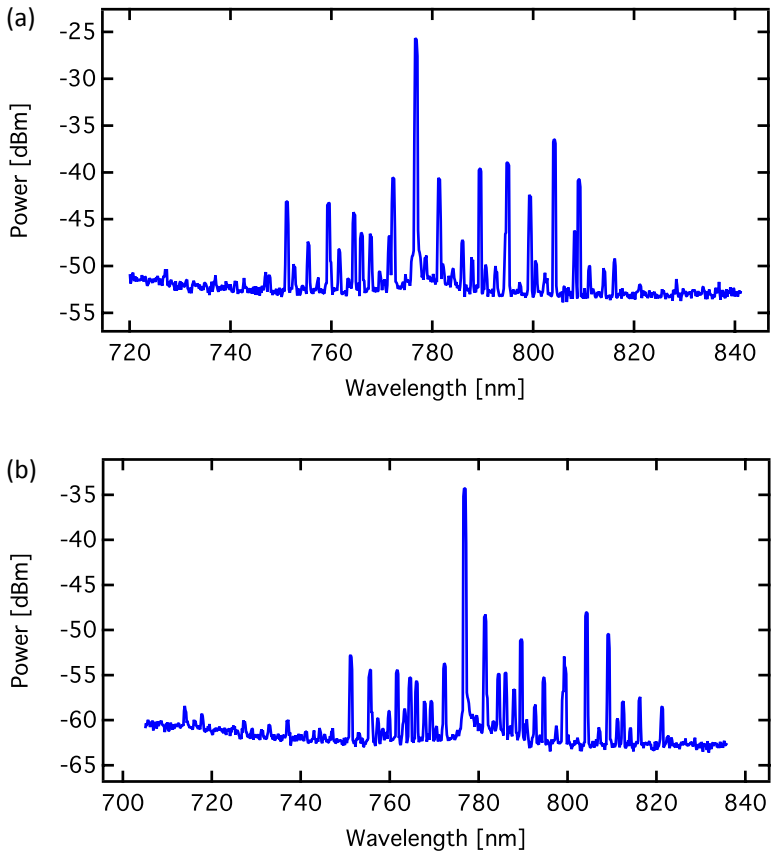

Figure 6.13: Comb spectrum obtained by tuning the laser into cavity modes (a) 188 GHz and (b) 376 GHz away from the cavity mode shown in Fig. 6.12. Greater than 40 comb lines are observed in the wavelength range between 710 nm and 820 nm.

6.7 Comb evolution

As mentioned earlier, comb generation process in the Si_3N_4 microresonator results from FWM (degenerate and non-degenerate) and has been previously used

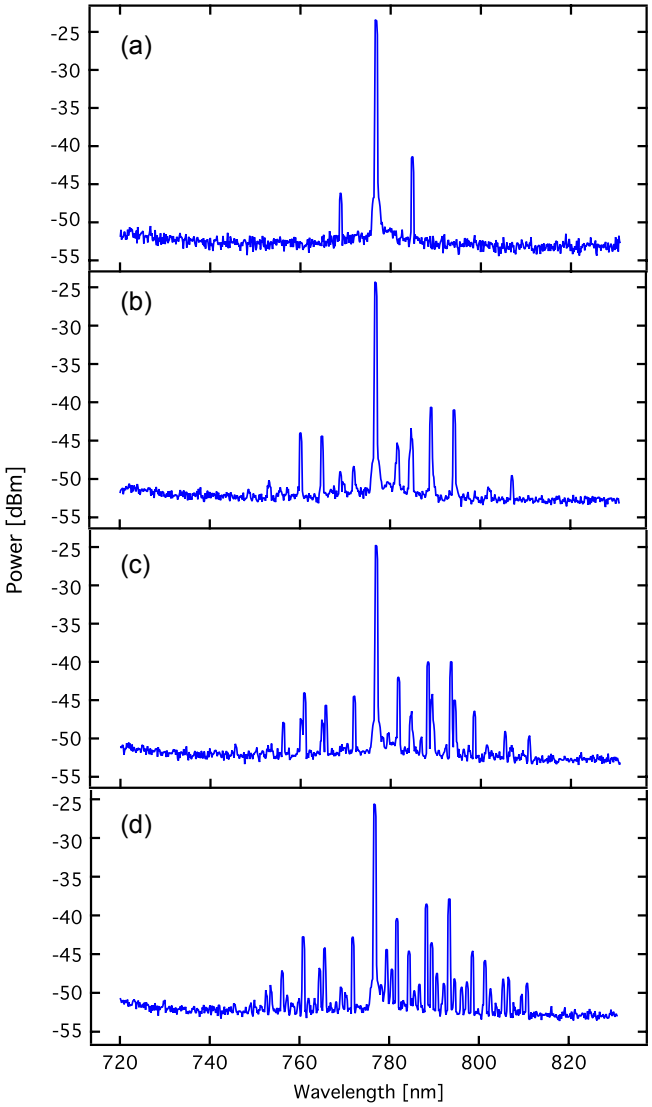

Figure 6.14: Plot of comb spectrum as the laser is tuned into cavity resonance, describing the generation of (a) first sideband due to degenerate FWM [laser detuned from cavity mode]. (b)-(c) more sidebands due to both degenerate and non degenerate FWM (d) minicombs due to FWM between pump and primary sidebands [laser close to resonance with cavity mode].

to demonstrate octave spanning combs at telecom [118, 119] and broad combs at 1 μm [143] and mid-infrared wavelengths [144]. Tuning the cavity into resonance with the pump laser, leads to the build-up of circulating power in the ring cavity and beyond a threshold power (power level at which the gain of the parametric process exceeds the cavity loss) we begin to observe the first sidebands [see Fig.

6.14(a)]. The sidebands at 785.6 nm and 766.6 nm, result from a degenerate FWM process involving the pump beam i.e. $2\omega_p = \omega_{s1} + \omega_{s2}$, where ω_p is frequency of the pump beam and ω_{s1} and ω_{s2} are the frequencies of the red and blue detuned sidebands as seen in Fig. 6.14(a). Operating with pump power below oscillation threshold could also lead to efficient quantum correlated photon pair-generation at the first sidebands. By modifying the coupling strength and GVD for the microresonator, it is possible to tune the frequencies at which the first sidebands appear and could lead to tunable photon-pair generation.

Further tuning the laser into the cavity, leads to generation of more sidebands as seen in Fig. 6.14(b) and Fig. 6.14(c). When the laser detuning from the cavity mode is small, enough circulating power builds inside the resonator, such that each side band acts like a pump and mixes with adjacent sidebands to form minicombs via FWM, as seen in Fig. 6.14(d).

6.8 Threshold for comb generation

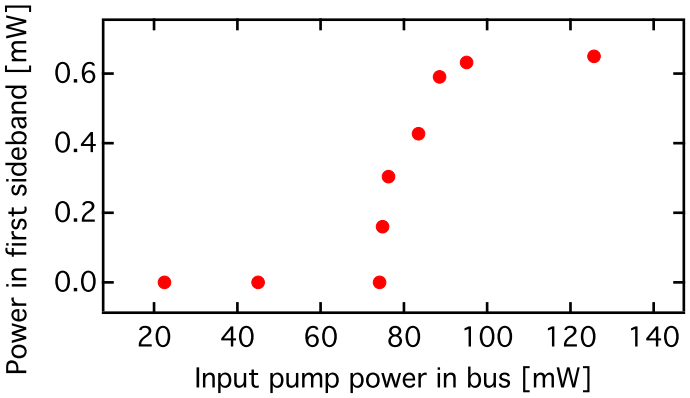

Figure 6.15: Plot of power in the first sideband of the generated comb spectrum as a function of input pump power coupled in the bus waveguide. We observe that the first sideband appear when a threshold power of 74 mW is coupled into the bus waveguide.

To estimate the threshold power of oscillation, we gradually increased the power inside the bus waveguide and tuned the cavity into resonance. The generation of first sidebands was observed at a threshold power $P_T = 74$ mW inside the bus waveguide as seen in Fig. 6.15. Presently, we were limited by the Q value of the resonators and the coupling losses to the bus waveguide, which prevented us from achieving a natively spaced mode-locked comb. As $P_T \propto \frac{1}{Q^2}$, increasing the Q value by a factor of 3 in our future devices would lead to a threshold power of ~ 8 mW for oscillation, which can enable comb generation with line spacing equal to the FSR.

6.9 Mode-locking

We model the comb numerically using the modified Lugiato-Lefever equation [145]. Figure 6.16 shows the simulated spectrum and the temporal profile (inset) pumping at 800 nm based on the GVD in Fig. 6.5. Our modeling indicates that a broadband mode-locked comb [146] can be achieved via higher-order mode excitation in the microresonator.

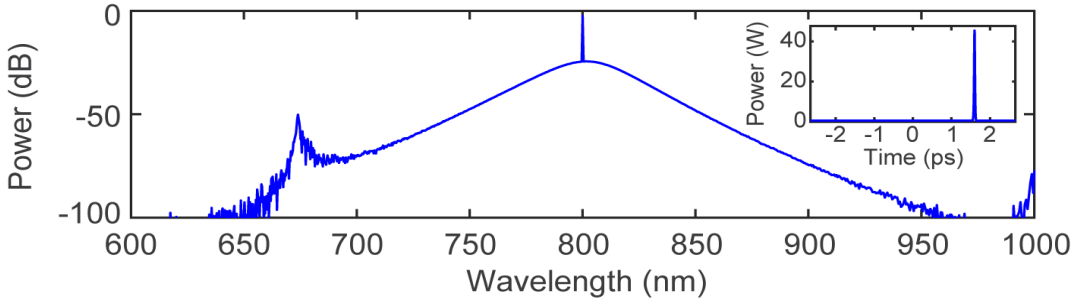

Figure 6.16: Simulated spectrum and temporal profile (inset) for comb generation in a Si_3N_4 microresonator. We use the dispersion profile of a TE_{20} mode of a 0.44×1.3 μm cross section, and take into account mode coupling.

6.10 Conclusion

In summary, we successfully demonstrate broadband FWM in the near-visible range by engineering anomalous GVD for higher-order modes. The higher-order modes are selectively excited by fundamental to higher-order mode conversion between the bus waveguide and microresonator. Using dispersion engineered microresonators, we report for the first time, broadband comb generation in the near-visible spanning 45 THz around 780 nm. Comb lines are generated across the D_1 and D_2 transitions of commonly used alkali like Potassium and Rubidium. Our results open new possibilities for developing broadband and tunable single photon sources in the near-visible which could be compatible with atomic quantum memories and can be efficiently detected. In future experiments, we aim at increasing the Q value for the higher-order modes in the microresonators which could lead to the lowering of threshold power and aid the generation of a mode-locked comb. Mode-locking should greatly facilitate a technological advance in the goal towards building on-chip ultrafast laser sources in the near-visible wavelength regime. The high Q value for the microresonator could also potentially lead to spectrally bright photon-pair generation.

CHAPTER 7

FUTURE DIRECTIONS

In this chapter we explore future experiments that can be performed with the Rb-PBGF and Rb-chip system.

7.1 Quantum frequency translation from telecom to visible using Rb-filled PBGF's

We explore the feasibility of performing quantum frequency conversion from telecom to visible wavelengths using the Rb-PBGF system. This is of particular interest, as there have been great strides in developing tunable single photon sources [38, 39, 48–51] and detectors [147] at telecom wavelengths. However even today, the most efficient quantum memories are implemented using atoms [44–47] and such a long range frequency conversion can be used for interfacing devices operating in regimes with a large frequency difference. Moreover, it becomes extremely difficult to engineer the dispersion for conventional solid-state waveguides for achieving phase matching over such a large wavelength range (1550 nm - 800 nm). Recently, BS-FWM in a Si_3N_4 microresonator has been used to demonstrate quantum frequency conversion from 1550 nm - 980 nm (112 THz signal-idler separation) [37].

As explained in chapter 2, efficient frequency conversion can be achieved at low pump powers by leveraging the large effective Kerr nonlinearity of the Rb-PBGF system. Figure 7.1 shows the diamond level scheme in ^{85}Rb that can enable this broadband telecom to near-visible frequency conversion. In the presence of Pumps

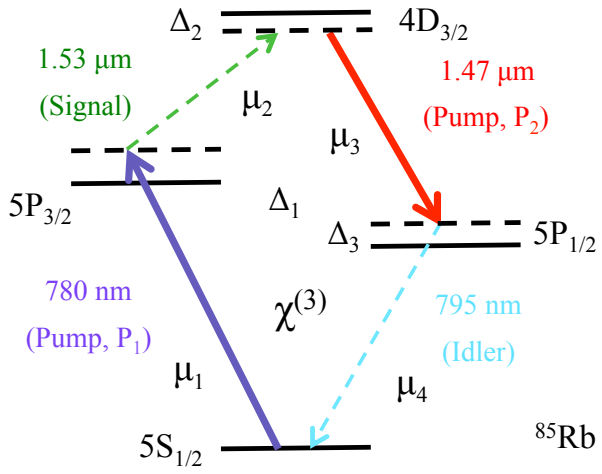

Figure 7.1: ^{85}Rb level scheme used in the experiment. Pump beams at 780 nm and 1.47 μm are tuned to the D_2 and $4D_{3/2} \rightarrow 5P_{1/2}$ transitions of ^{85}Rb respectively. A signal beam at 1.53 μm is frequency translated to the idler at 795 nm.

P_1 and P_2 tuned to the $5S_{1/2} \rightarrow 5P_{3/2}$ (780nm) and $4D_{3/2} \rightarrow 5P_{1/2}$ (1475 nm) transitions respectively, a weak signal beam photon at 1529 nm (telecom S-band) can be converted to an idler photon at 795 nm (near-visible) via noiseless frequency conversion using BS-FWM. The frequency difference between the signal and idler is 181 THz. The detunings Δ_1, Δ_2 and Δ_3 are maintained with respect to the $5S_{1/2}, F = 3 \rightarrow 5P_{3/2}$, F' = 4, $5P_{1/2}, F = 3 \rightarrow 4D_{3/2}$, F" = 3, and $5S_{1/2}, F = 3 \rightarrow 5P_{1/2}$, F' = 3 transitions respectively. To guide wavelengths covering such a large spectrum in frequency, we propose to use a Kagomé type PBGF filled with Rb vapor which has been discussed in previous demonstration of cross-phase modulation [36] and quantum memories with cesium atoms [47].

To demonstrate the feasibility of the scheme, we have recently performed a preliminary experiment in a warm Rb vapor-cell. The schematic for our experimental setup is shown in Fig. 7.2. Pump beams P_1 and P_2 along with the weak signal beam at 1529 nm are sent co-propagating, collinear and horizontally polarized (H) into a warm (82°C), 2-cm long, isotopically pure ^{85}Rb vapor-cell. A beam waist of

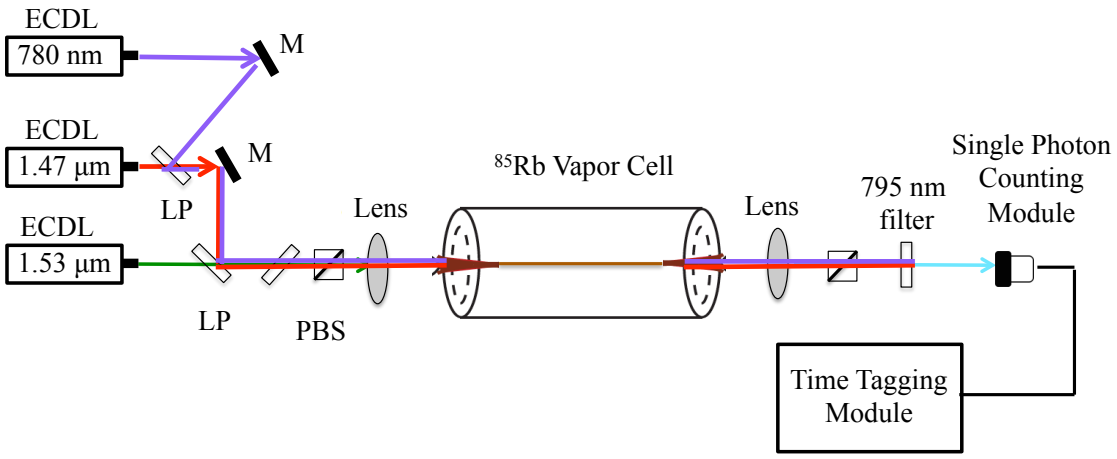

Figure 7.2: Pump beams at 780 nm and 1.47 μm ($\sim$ 1 mW each), and a weak signal beam at 1.53 μm (200 pW), are horizontally polarized and sent co propagating and collinear in an isotopically pure ^{85}Rb vapor cell maintained at 82°C. The generated idler at 795 nm is spectrally filtered using band-pass filters and measured using a single photon counting module.

80 μm is maintained for the overall length of the cell by means of a focusing and a collimating lens (f = 15 cm). The generated idler at 795 nm is spectrally filtered using a band pass filter and is measured using a single photon counting module. A time tagging module is used to trigger the counter and also record the counts. At first, we set each input pump beam at a CW power of 1 mW and maintain a signal beam power as low as 200 pW. By frequency tuning the pumps and the signal beam, we obtain a maximum energy conversion efficiency of 0.15 % from signal to the idler at detunings of $\Delta_1 = 900$ MHz , $\Delta_2 = 250$ MHz, and $\Delta_3 = 880$ MHz. To the best of our knowledge, this 181 THz signal-idler separation is the largest that has been demonstrated in a BS-FWM experiment compared to all previous works [37, 86]. As seen from equation 2.7, in the limit of perfect phase matching and negligible linear or nonlinear losses experienced by either of the pump or the signal beams, the idler generation depends on the pump power and propagation lengths as,

$$P_{idler}(z) = P_{signal}(0)\sin^2(2\gamma\sqrt{P_1 P_2}z) \tag{7.1}$$

where γ is the effective nonlinearity of the system. The expression for γ with wavelengths far separated by 181 THz, is not so straightforward and would entail writing separate expressions for γ's around each field. Nevertheless, in the limit of $\gamma\sqrt{P_1 P_2}z << 1$, we can approximate the idler power as,

$$P_{idler}(z) = 4P_{signal}(0)(\gamma z)^2 P_1 P_2 \tag{7.2}$$

and we expect idler generation to linearly vary with each pump power (with the

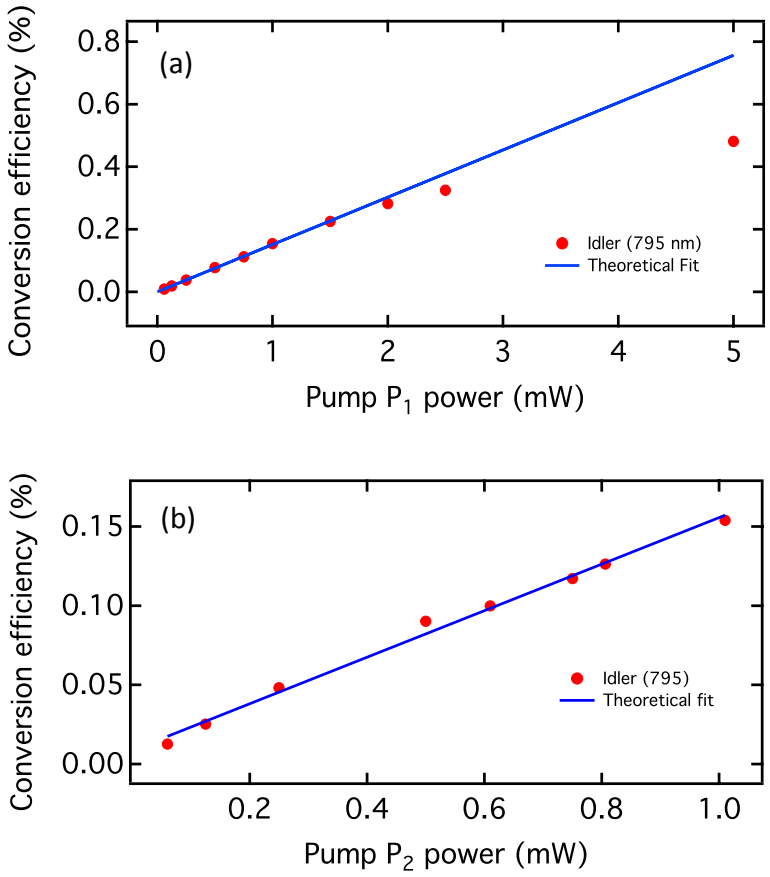

Figure 7.3: Plot of energy conversion efficiency versus pump power for (a) P_1 (780 nm) and (b) P_2 (1.47 μm). We observe the counts to scale linearly with each pump upto 1 mW of pump power. As we increase the power of P_1 further [as seen in (a)], the counts saturate due to nonlinear phase mismatch induced by the significant difference in the two pump powers and the large nonlinearity.

second pump constant) in this regime of operation. Figures 7.3 (a) and (b) show the power dependence of the BS-FWM conversion efficiency measured as a function of

pump powers P_1 (P_2 constant at 1 mW) and P_2 (P_1 constant at 1 mW) respectively. We observe a linear dependence at P_1 power levels less than 1 mW and the idler counts seem to approach a saturation level at higher powers. The saturation effect can be explained by the resulting nonlinear phase mismatch created by a significant imbalance in the pump power levels and the large γ, which can be rectified by increasing the power of P_2 correspondingly. In our present experiment we could

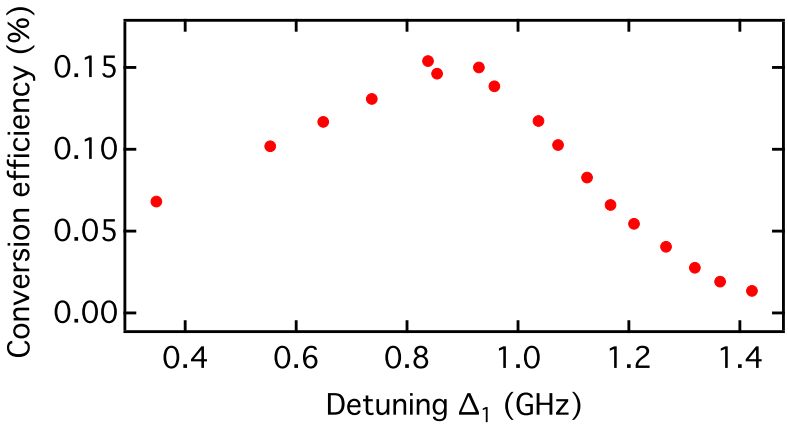

Figure 7.4: Energy conversion efficiency of the idler beam as function of pump P_1 detuning. We measure a bandwidth of 700 MHz for energy conversion efficiency of the BS-FWM process.

not exceed a power level of 1 mW on the pump beam set at 1.47 μm and hence did not observe the saturation effect while increasing the P_2 power. We also estimated the bandwidth for idler generation by varying the detuning Δ_1 of pump beam P_1, while keeping all other parameters constant. As seen in Fig. 7.4, we observe a Gaussian lineshape for the signal-idler energy conversion efficiency by varying Δ_1 and estimate a bandwidth of 700 MHz for the BS-FWM process.

The Rb-PBGF system is known to have a large γ [3, 41], and we have previously demonstrated a BS-FWM conversion efficiency of 21% for a signal-idler wavelength separation of 14 nm in the near-visible regime, as described in chapter 2. Leveraging the large nonlinearities of the Rb-Kagomé fiber system, it shall be

possible to achieve a large conversion efficiency (approaching near unit conversion) for the telecom to visible BS-FWM described above. From equations 2.8(a) and 2.9 we know,

$$\gamma \propto N/A \tag{7.3}$$

where, N is the atomic number density and A is the optical mode area. In the above experiment, a cell temperature of 82°C, would correspond to N $\sim 10^{18}$ atoms/m^3. Based on previous demonstrations [36, 47], we assume that an atomic number density of $\sim 10^{19}$ atoms/m^3 can be routinely achieved in a Kagomé fiber with a core size of 15 μm radius, for an interaction length of 10 cm, and can conclude from equation 7.3,

$$\gamma^{PBGF} = 280 \times \gamma^{vc} \tag{7.4}$$

where, 'vc' refers to the value in the bulk vapor-cell. In the regime of equal pump powers i.e. $P_1 = P_2 = P$, attaining a unit conversion efficiency in the Rb-PBGF system would require a pump power given by,

$$P^{PBGF} = \frac{\pi}{2}\sqrt{\frac{1}{\eta^{vc}}}\frac{L^{vc}}{L^{PBGF}}\frac{\gamma^{vc}}{\gamma^{PBGF}}P^{vc} \tag{7.5}$$

where η^{vc} is the energy conversion for BS-FWM in the bulk vapor cell and L is the interaction length of the medium. For BS-FWM performed in the vapor cell, we achieved a conversion efficiency $\eta^{vc} = 0.15\%$ at pump powers of 1 mW for each beam. Combining this with equations 7.4 and 7.5, yields a pump power requirement of ~ 30 μW in the Rb-PBGF system for achieving a unit signal-idler energy conversion efficiency over a frequency range spanning 181 THz.

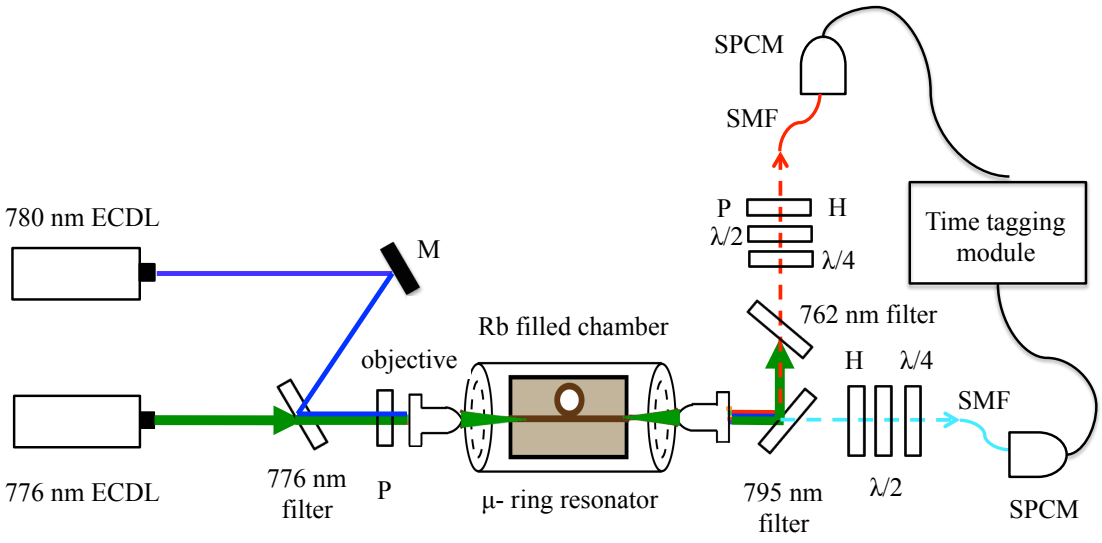

Figure 7.5: Horizontally polarized pump (776 nm) beam and a weak input beam (780nm) are coupled in the bus waveguide of the air-clad Si_3N_4 microresonator mounted inside a UHV chamber. Pairs of photon at 795 nm (idler) and 762 nm (signal) generated from the evanescent interaction of Rb with the microresonator mode, are separated using bandpass filters and measured using single photon counting modules.

7.2 CPC using Rb vapor evanescently coupled to air-clad silion nitride microresonator

We plan to implement CPC in the Rb-chip system using the diamond level scheme shown in Fig. 4.4, such that the presence of a strong pump at 776 nm, can convert a single photon at 780 nm to a pair of photons at 762 nm and 795 nm. To have maximum pair generation efficiency, we plan to use an air-clad Si_3N_4 ring resonator; the evanescent field of which would be cavity enhanced and coupled to the warm Rb vapor in the vicinity of the chip. A schematic for the experimental setup is shown in Fig. 7.5. The pump beam at 776 nm and the weak input at 780 nm are coupled into the bus waveguide using a high numerical aperture (N.A) and long working distance objectives. The pairs of photons at 762 nm and 795 nm

generated from the $\chi^{(2)}_{eff}$ CPC process [refer to sections 4.4 - 4.8 for more details], can be separated using appropriate band pass filters and are detected using single photon counting modules (SPCM's). By adding suitable time delays using a time tagging module, we can test the timing correlation between the generated photon pairs. As explained in section 4.2, complete conversion requires Γt $\sim \pi/2$, and in previous experiments a Γt of 10^{-4} was demonstrated using photonic crystal fibers with $\gamma = 0.1$ $\mathrm{W^{-1}m^{-1}}$ and peak pump powers of 2 kW [4]. After taking into account the appropriate scaling factors for the Rb-microresonator system, the modified expression for the coupling constant is,

$$\Gamma t = \frac{2\chi^{(3)}}{{n_0}^{3.5}\epsilon_0}\sqrt{\frac{\pi P_{ring} h\omega}{cA_{ring}}}\frac{Q}{\sqrt{V_{ring}}} \tag{7.6}$$

where, $\chi^{(3)}$ is the third order nonlinearity for the evanescently coupled Rb-microresonator system, ω is the angular frequency of the laser field, $\mathrm{A_{ring}}$ and $\mathrm{V_{ring}}$ are the effective mode area and the mode volume for the evanescent field respectively, while Q and $\mathrm{P_{ring}}$ are the quality factor and power inside the ring cavity respectively. The intracavity power is given by $P_{ring} = P_{WG}\frac{F}{\pi}$, where P_{WG} is the power of the input beam coupled in the waveguide and F is the Finesse of the ring cavity (defined as, F = FSR/Δf, where Δf is the cavity linewidth). By invoking expressions 4.4 - 4.8 and 7.6, we can compare the effective CPC interaction lengths in the Rb-microresonator and Rb-vapor cell (similar to the one used in chapter 4) systems as,

$$(\Gamma t)^{ring} = (\Gamma t)^{vc}\frac{4}{3\pi}Q\lambda\frac{\chi^{(3)}_{ring}}{\chi^{(3)}_{vc}}\frac{A_{vc}}{A_{ring}}\sqrt{\frac{F\eta}{2\pi Rc\tau_{vc}}}\sqrt{\frac{P_{WG}}{P_{vc}}} \tag{7.7}$$

where, η is the fraction of input mode evanescently coupled with Rb, τ_{vc} is the mode interaction lifetime and A_{vc} is the effective mode area in the vapor cell. In the limit of $\Gamma t << 1$, photon pair generation efficiency is proportional to $(\Gamma t)^2$. We know from section 4.7, $(\Gamma t)^{vc} = 2.5 \times 10^{-4}$, per kW of pump beam. By assuming

vapor densities in the Rb-chip chamber, comparable to those in the vapor cell and maintaining detunings as explained in section 4.3 (i.e $\Delta_1 = 910$ MHz, $\Delta_2 = 0$ MHz), we can assume equal $\chi^{(3)}$'s for the two systems . The bandwidth for pair generation in the vapor cell is 1.5 GHz, which gives $\tau_{vc} \sim 10^{-10}$ s^{-1}. To prevent dephasing of Rb atoms from the waveguide surface, we conservatively consider the mode field in a narrow cross-section of width = 50 nm, about 50 nm away from the waveguide surface which also corresponds to $\sim 2\%$ of the guided TM mode. We refer to this effective interaction area for the evanescent mode 50 nm away from the waveguide surface as A_{ring}. In section 5.6 we measured a Q value of 100,000 which also corresponds to F = 50 for the air-clad ring cavity with FSR = 210 GHz. This implies, achieving unit CPC pair generation efficiency [i.e. $(\Gamma t)^{\text{ring}} = \pi/2$], would require only ~ 1 mW of power in the pump beam. We would thereby realize $\chi^{(2)}_{eff}$ for a CPC process, orders of magnitude larger than those previously reported and at much lower pump powers.

Appendices

APPENDIX A

NONLINEAR OPTICAL RESPONSE

When light interacts with matter, the electric field of light exerts a force on the electron cloud bound to the nuclei of the atoms. This force changes the distribution of the electron cloud about the nuclei resulting in the polarization of the material. As electrons accelerate back and forth under the influence of the oscillating field of light, they radiate energy in the form of electromagnetic radiation as suggested by Maxwell's relations. The polarization $\mathbf{P}(\mathbf{t})$ induced in the medium is proportional to the electric field $\mathbf{E}(\mathbf{t})$ and can be expressed as [56],

$$\mathbf{P}(\mathbf{t}) = \bar{\chi}\mathbf{E}(\mathbf{t}) \tag{A.1}$$

where, $\bar{\chi}$ is the tensor for electric susceptibility. In general, $\bar{\chi}$ is a function of electric field and we can follow a Taylor expansion of the susceptibility, expressed as,

$$\bar{\chi} = \bar{\chi}^{(1)} + \bar{\chi}^{(2)}E(t) + \bar{\chi}^{(3)}E(t)E(t) + ... \tag{A.2}$$

where, $\bar{\chi}^{(i)}$ refers to the i^{th} order correction to the linear behavior. For materials symmetric at the atomic/molecular level (also called centrosymmetric materials and includes the Rb vapor and Si_3N_4 waveguides), $\bar{\chi}^{(2)}$ vanishes and the most dominant term in the nonlinear response is $\bar{\chi}^{(3)}$. This third order nonlinearity ($\bar{\chi}^{(3)}$) is also called the Kerr nonlinearity and has been widely discussed in our work. From equation A.2, it is clear that, larger the strength of the electric field, larger is the contribution of the higher order nonlinear terms to the total electric field response of the system.

APPENDIX B

VAPOR-CELL CPC PARAMETER ESTIMATION

For a function f, which depends on response variables x_1, x_2, ... x_n, the total error in measuring 'f' can be estimated by the principle of propagation of uncertainty which is given by,

$$\Delta f = \sqrt{(\frac{\delta f}{\delta x_1})^2 {\Delta x_1}^2 + (\frac{\delta f}{\delta x_2})^2 {\Delta x_2}^2 + ... + (\frac{\delta f}{\delta x_n})^2 {\Delta x_n}^2} \tag{B.1}$$

where, Δx_i is the uncertainty in the measured value for the response variable x_i, for $i = 1, 2...n$.

B.1 Measurement of coincidences/second between the signal and idler photons

The coincidences between the signal and idler photons are determined by performing a gated measurement between the two single photon counting modules (SPCM's), by binning the detectors clicks over a finite range of time delay. We hence measure the counts on the SPCM for the idler photons (say I) conditioned on the arrival of a photon at the SPCM measuring the signal photon (say S), giving us the necessary second order correlation between the two. As seen in Fig. B.1, this also results in the measurement of background counts/sec/bin (N_{b0}) due to accidental coincidences measured from the singles N_I and N_S, recorded on detectors I and S respectively which is given by,

$$N_{b0} = N_I N_S \Delta t \tag{B.2}$$

where, Δt is the width of each bin measuring the time-delay. Let 'n' be the total number of bins within the coincidence window and N_i be the counts measured in

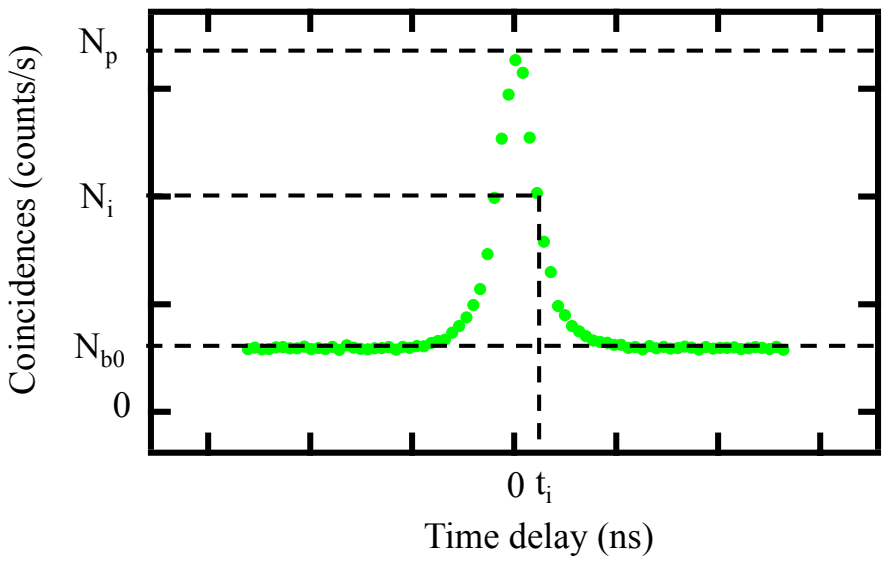

Figure B.1: Viewgraph indicating a coincidence measurement between signal and idler photons. N_{b0} refer to the accidental coincidences measured per second in each bin and N_p refers to the counts measured in the bin at zero time delay [peak of the cross correlation measurement]. N_i represent the counts in the bin at time delay t_i.

the i^{th} bin at a time delay t_i as shown in Fig. B.1. This leads to an overall number of coincidences called N_c such that,

$$N_c = \sum_{i=1}^{n} (N_i - N_{b0}) \tag{B.3}$$

Due to the gated measurement, the measurement on each bin is only shot-noise limited, which leads on an error per bin $\Delta N_i = \sqrt{N_i}$. From equations B.1 and B.3, the total error in measuring the coincidences is given by,

$$\Delta N_c = \sqrt{(\sum_{i=1}^{n} N_i) + (n\Delta N_{b0})^2} \tag{B.4}$$

where, ΔN_{b0} is the error in measuring N_{b0}. In the experiment we average the counts recorded in a total of 'k' bins away from the coincidence peak so that they accurately represent the background, and measure $N_{b0} = \frac{\sum_{n=1}^{k} N_n}{k}$ with an overall error,

$$\Delta N_{b0} = \frac{\sqrt{\sum_{n=1}^{k} N_n}}{k} \tag{B.5}$$

B.2 $g^{(2)}(0)$ between the signal and idler photons

As seen in Fig. B.1, let N_p be the counts/sec measured in the bin recording the maximum coincidences, and we define the total background subtracted counts as $N_t = N_p - N_{b0}$. The second-order correlation at zero time delay is given by,

$$g^{(2)}_{SI}(0) = \frac{N_t}{N_{b0}} \tag{B.6}$$

From equation B.1 we get,

$$\Delta g^{(2)}_{SI}(0) = \sqrt{(\frac{1}{N_{b0}})^2 {\Delta N_t}^2 + (\frac{N_t}{{N_{b0}}^2})^2 {\Delta N_{b0}}^2} \tag{B.7}$$

where, $\Delta N_t = \sqrt{N_p + {\Delta N_{b0}}^2}$ and $\Delta N_{b0} = \frac{\sqrt{\sum_{n=1}^{k} N_n}}{k}$.

B.3 $g^{(2)}(0)$ for the signal(idler) photons

To measure the second order correlation for the signal(idler) photons, we split the original signal (idler) beams using a 50:50 fiber splitter and send each arm to SPCM's D_1 and D_2. As explained in section B.1, we yet again measure a gated response of D_1 conditioned upon the arrival of photon on D_2. From here on, we shall present the analysis for the signal photon which shall remain the same for the idler. Let N_p represent the counts in the bin recording the peak of the coincidence measurement between signal photons (e.g. see Fig. B.1, for the coincidence measurement done between signal and idler), and N_{b0} represent the background counts resulting from accidental coincidences between the two detectors. The second order correlation between the signal photons at zero time delay is given by,

$$g^{(2)}_{S}(0) = \frac{N_p}{N_{b0}} \tag{B.8}$$

From equation B.1, this leads to a measurement error of,

$$\Delta g_S^{(2)}(0) = \sqrt{\left(\frac{1}{N_{b0}}\right)^2 \Delta {N_p}^2 + \left(\frac{N_p}{{N_{b0}}^2}\right)^2 \Delta {N_{b0}}^2} \tag{B.9}$$

As explained in section B.1, $\Delta N_p = \sqrt{N_p}$ and $\Delta N_{b0} = \frac{\sqrt{\sum_{n=1}^{k} N_n}}{k}$, obtained by averaging background counts in a total of 'k' bins far away from the coincidence peak.

B.4 Cauchy Schwarz inequality

From equation 4.10, the parameter 'R' estimating the Cauchy Schwarz inequality ratio is given by,

$$R = \frac{{g_{SI}^{(2)}(\tau)}^2}{g_S^{(2)}(0) g_I^{(2)}(0)} \tag{B.10}$$

For simplicity, lets represent $\Delta g_{S/I}^{(2)}(0)$ and $\Delta g_{SI}^{(2)}(0)$ as $\Delta g_{S/I}^{(2)}$ and $\Delta g_{SI}^{(2)}$ respectively. From equation B.1, the error ΔR is given by,

$$\Delta R = \sqrt{\left(\frac{1}{g_I g_S}\right)^2 \Delta {g_{SI}}^2 + \left(\frac{g_{SI}}{{g_I}^2 g_S}\right)^2 \Delta {g_I}^2 + \left(\frac{g_{SI}}{{g_S}^2 g_I}\right)^2 \Delta {g_S}^2} \tag{B.11}$$

BIBLIOGRAPHY

[1] NKT Photonics PCF, http://assets.newport.com/webDocuments-EN/images/15128.PDF .

[2] R. F. Cregan, B. J. Mangan, J. C. Knight, T. A. Birks, P. S. J. Russell, P. J. Roberts, and D. C. Allan, "Single-Mode Photonic Band Gap Guidance of Light in Air," Science **285**, 1537–1539 (1999).

[3] S. Ghosh, A. R. Bhagwat, C. K. Renshaw, S. Goh, A. L. Gaeta, and B. J. Kirby, "Low-Light-Level Optical Interactions with Rubidium Vapor in a Photonic Band-Gap Fiber," Physical Review Letters **97** (2006).

[4] N. K. Langford, S. Ramelow, R. Prevedel, W. J. Munro, G. J. Milburn, and A. Zeilinger, "Efficient quantum computing using coherent photon conversion," Nature **478**, 360–363 (2011).

[5] P. S. Londero, J. Levy, A. Slepkov, A. Bhagwat, K. Saha, V. Venkataraman, M. Lipson, and A. L. Gaeta, "Chip-based optical interactions with Rubidium vapor," in "Quantum Electronics and Laser Science Conference," (Optical Society of America, 2010), p. QFE4.

[6] J. I. Cirac and P. Zoller, "A scalable quantum computer with ions in an array of microtraps," Nature **404**, 579–581 (2000).

[7] S. Debnath, N. M. Linke, C. Figgatt, K. A. Landsman, K. Wright, and C. Monroe, "Demonstration of a small programmable quantum computer with atomic qubits," Nature **536**, 63–66 (2016).

[8] M. H. Devoret and R. J. Schoelkopf, "Superconducting Circuits for Quantum Information: An Outlook," Science **339**, 1169–1174 (2013).

[9] J. Clarke and F. K. Wilhelm, "Superconducting quantum bits," Nature **453**, 1031–1042 (2008).

[10] A. D. Córcoles, E. Magesan, S. J. Srinivasan, A. W. Cross, M. Steffen, J. M. Gambetta, and J. M. Chow, "Demonstration of a quantum error detection code using a square lattice of four superconducting qubits," Nature Communications **6**, 6979 (2015).

[11] M. W. Johnson, M. H. S. Amin, S. Gildert, T. Lanting, F. Hamze, N. Dickson, R. Harris, A. J. Berkley, J. Johansson, P. Bunyk, E. M. Chapple, C. En-

derud, J. P. Hilton, K. Karimi, E. Ladizinsky, N. Ladizinsky, T. Oh, I. Perminov, C. Rich, M. C. Thom, E. Tolkacheva, C. J. S. Truncik, S. Uchaikin, J. Wang, B. Wilson, and G. Rose, "Quantum annealing with manufactured spins," Nature **473**, 194–198 (2011).

[12] E. Knill, R. Laflamme, and G. J. Milburn, "A scheme for efficient quantum computation with linear optics," Nature **409**, 46–52 (2001).

[13] J. L. O'Brien, A. Furusawa, and J. Vučković, "Photonic quantum technologies," Nat Photon **3**, 687–695 (2009).

[14] P. Kok, W. J. Munro, K. Nemoto, T. C. Ralph, J. P. Dowling, and G. J. Milburn, "Linear optical quantum computing with photonic qubits," Rev. Mod. Phys. **79**, 135–174 (2007).

[15] D. Loss and D. P. DiVincenzo, "Quantum computation with quantum dots," Phys. Rev. A **57**, 120–126 (1998).

[16] S. E. Thompson and S. Parthasarathy, "Moore's law: the future of Si microelectronics," Materials Today **9**, 20–25 (2006).

[17] I. Georgescu, S. Ashhab, and F. Nori, "Quantum simulation," Rev. Mod. Phys. **86**, 153–185 (2014).

[18] W. H. Zurek, "Decoherence and the transition from quantum to classical – REVISITED," arXiv:quant-ph/0306072 (2003). ArXiv: quant-ph/0306072.

[19] X.-S. Ma, T. Herbst, T. Scheidl, D. Wang, S. Kropatschek, W. Naylor, B. Wittmann, A. Mech, J. Kofler, E. Anisimova, V. Makarov, T. Jennewein, R. Ursin, and A. Zeilinger, "Quantum teleportation over 143 kilometres using active feed-forward," Nature **489**, 269–273 (2012).

[20] H. Takesue, S. D. Dyer, M. J. Stevens, V. Verma, R. P. Mirin, and S. W. Nam, "Quantum teleportation over 100 km of fiber using highly efficient superconducting nanowire single-photon detectors," Optica, OPTICA **2**, 832–835 (2015).

[21] J. Yin, J.-G. Ren, H. Lu, Y. Cao, H.-L. Yong, Y.-P. Wu, C. Liu, S.-K. Liao, F. Zhou, Y. Jiang, X.-D. Cai, P. Xu, G.-S. Pan, J.-J. Jia, Y.-M. Huang, H. Yin, J.-Y. Wang, Y.-A. Chen, C.-Z. Peng, and J.-W. Pan, "Quantum teleportation and entanglement distribution over 100-kilometre free-space channels," Nature **488**, 185–188 (2012).

[22] Z. Tang, R. Chandrasekara, Y. C. Tan, C. Cheng, L. Sha, G. C. Hiang, D. K. Oi, and A. Ling, "Generation and Analysis of Correlated Pairs of Photons aboard a Nanosatellite," Phys. Rev. Applied **5**, 054022 (2016).

[23] "Quantum optics lifts off," Nat Photon **10**, 689–689 (2016).

[24] T. Guerreiro, A. Martin, B. Sanguinetti, J. Pelc, C. Langrock, M. Fejer, N. Gisin, H. Zbinden, N. Sangouard, and R. Thew, "Nonlinear Interaction between Single Photons," Physical Review Letters **113** (2014).

[25] G. J. Milburn, "Quantum optical Fredkin gate," Phys. Rev. Lett. **62**, 2124–2127 (1989).

[26] D. Petrosyan, "Towards deterministic optical quantum computation with coherently driven atomic ensembles," J. Opt. B: Quantum Semiclass. Opt. **7**, S141 (2005).

[27] W. Chen, K. M. Beck, R. Bücker, M. Gullans, M. D. Lukin, H. Tanji-Suzuki, and V. Vuletić, "All-optical switch and transistor gated by one stored photon," Science p. 1237242 (2013).

[28] T. G. Tiecke, J. D. Thompson, N. P. de Leon, L. R. Liu, V. Vuletić, and M. D. Lukin, "Nanophotonic quantum phase switch with a single atom," Nature **508**, 241–244 (2014).

[29] A. Reiserer, N. Kalb, G. Rempe, and S. Ritter, "A quantum gate between a flying optical photon and a single trapped atom," Nature **508**, 237–240 (2014).

[30] J. Volz, M. Scheucher, C. Junge, and A. Rauschenbeutel, "Nonlinear phase shift for single fibre-guided photons interacting with a single resonator-enhanced atom," Nature Photonics **8**, 965–970 (2014).

[31] Q. A. Turchette, C. J. Hood, W. Lange, H. Mabuchi, and H. J. Kimble, "Measurement of Conditional Phase Shifts for Quantum Logic," Phys. Rev. Lett. **75**, 4710–4713 (1995).

[32] T. Peyronel, O. Firstenberg, Q.-Y. Liang, S. Hofferberth, A. V. Gorshkov, T. Pohl, M. D. Lukin, and V. Vuletić, "Quantum nonlinear optics with single photons enabled by strongly interacting atoms," Nature **488**, 57–60 (2012).

[33] C. Tresp, C. Zimmer, I. Mirgorodskiy, H. Gorniaczyk, A. Paris-Mandoki,

and S. Hofferberth, "Single-Photon Absorber Based on Strongly Interacting Rydberg Atoms," Phys. Rev. Lett. **117**, 223001 (2016).

[34] S. M. Hendrickson, M. M. Lai, T. B. Pittman, and J. D. Franson, "Observation of Two-Photon Absorption at Low Power Levels Using Tapered Optical Fibers in Rubidium Vapor," Phys. Rev. Lett. **105**, 173602 (2010).

[35] M. R. Sprague, D. G. England, A. Abdolvand, J. Nunn, X.-M. Jin, W. Steven Kolthammer, M. Barbieri, B. Rigal, P. S. Michelberger, T. F. M. Champion, P. S. J. Russell, and I. A. Walmsley, "Efficient optical pumping and high optical depth in a hollow-core photonic-crystal fibre for a broadband quantum memory," New Journal of Physics **15**, 055013 (2013).

[36] C. Perrella, P. S. Light, J. D. Anstie, F. Benabid, T. M. Stace, A. G. White, and A. N. Luiten, "High-efficiency cross-phase modulation in a gas-filled waveguide," Physical Review A **88** (2013).

[37] Q. Li, M. Davanço, and K. Srinivasan, "Efficient and low-noise single-photon-level frequency conversion interfaces using silicon nanophotonics," Nat Photon **10**, 406–414 (2016).

[38] E. Hemsley, D. Bonneau, J. Pelc, R. Beausoleil, J. L. O'Brien, and M. G. Thompson, "Photon pair generation in hydrogenated amorphous silicon microring resonators," Scientific Reports **6**, 38908 (2016).

[39] S. Ramelow, A. Farsi, S. Clemmen, D. Orquiza, K. Luke, M. Lipson, and A. L. Gaeta, "Silicon-nitride platform for narrowband entangled photon generation," arXiv preprint arXiv:1508.04358 (2015).

[40] H. Schmidt and A. Imamoglu, "Giant Kerr nonlinearities obtained by electromagnetically induced transparency," Optics letters **21**, 1936–1938 (1996).

[41] V. Venkataraman, K. Saha, and A. L. Gaeta, "Phase modulation at the few-photon level for weak-nonlinearity-based quantum computing," Nature Photonics **7**, 138–141 (2012).

[42] G. Nogues, A. Rauschenbeutel, S. Osnaghi, M. Brune, J. M. Raimond, and S. Haroche, "Seeing a single photon without destroying it," Nature **400**, 239–242 (1999).

[43] J. P. Poizat and P. Grangier, "Experimental realization of a quantum optical tap," Phys. Rev. Lett. **70**, 271–274 (1993).

[44] C. Liu, Z. Dutton, C. H. Behroozi, and L. V. Hau, "Observation of coherent optical information storage in an atomic medium using halted light pulses," Nature **409**, 490–493 (2001).

[45] D. F. Phillips, A. Fleischhauer, A. Mair, R. L. Walsworth, and M. D. Lukin, "Storage of Light in Atomic Vapor," Phys. Rev. Lett. **86**, 783–786 (2001).

[46] B. Julsgaard, J. Sherson, J. I. Cirac, J. Fiurášek, and E. S. Polzik, "Experimental demonstration of quantum memory for light," Nature **432**, 482–486 (2004).

[47] M. R. Sprague, P. S. Michelberger, T. F. M. Champion, D. G. England, J. Nunn, X.-M. Jin, W. S. Kolthammer, A. Abdolvand, P. S. J. Russell, and I. A. Walmsley, "Broadband single-photon-level memory in a hollow-core photonic crystal fibre," Nature Photonics **8**, 287–291 (2014).

[48] J. E. Sharping, K. F. Lee, M. A. Foster, A. C. Turner, B. S. Schmidt, M. Lipson, A. L. Gaeta, and P. Kumar, "Generation of correlated photons in nanoscale silicon waveguides," Opt. Express, OE **14**, 12388–12393 (2006).

[49] C. Reimer, M. Kues, L. Caspani, B. Wetzel, P. Roztocki, M. Clerici, Y. Jestin, M. Ferrera, M. Peccianti, A. Pasquazi, B. E. Little, S. T. Chu, D. J. Moss, and R. Morandotti, "Cross-polarized photon-pair generation and bi-chromatically pumped optical parametric oscillation on a chip," Nature Communications **6**, 8236 (2015).

[50] X. Zhang, Y. Zhang, C. Xiong, and B. J. Eggleton, "Correlated photon pair generation in low-loss double-stripe silicon nitride waveguides," J. Opt. **18**, 074016 (2016).

[51] S. Clemmen, A. Perret, S. K. Selvaraja, W. Bogaerts, D. v. Thourhout, R. Baets, P. Emplit, and S. Massar, "Generation of correlated photons in hydrogenated amorphous-silicon waveguides," Opt. Lett., OL **35**, 3483–3485 (2010).

[52] C. McKinstrie, J. Harvey, S. Radic, and M. Raymer, "Translation of quantum states by four-wave mixing in fibers," Optics express **13**, 9131–9142 (2005).

[53] C. J. McKinstrie, S. Radic, and M. G. Raymer, "Quantum noise properties of parametric amplifiers driven by two pump waves," Opt. Express, OE **12**, 5037–5066 (2004).

[54] S. Clemmen, A. Farsi, S. Ramelow, and A. L. Gaeta, "Ramsey Interference with Single Photons," Phys. Rev. Lett. **117**, 223601 (2016).

[55] T. Maiman, "Stimulated optical radiation in ruby," Nature **187**, 493–494 (1960).

[56] R. Boyd, Nonlinear Optics, 3rd edition. (Academic, 2008) .

[57] K. Saha, V. Venkataraman, P. Londero, and A. L. Gaeta, "Enhanced two-photon absorption in a hollow-core photonic-band-gap fiber," Physical Review A **83** (2011).

[58] D. A. Steck, "^{87}Rb and ^{85}Rb D_1 line data," https://steck.us/alkalidata/ (2013).

[59] K. B. MacAdam, A. Steinbach, and C. Wieman, "A narrow band tunable diode laser system with grating feedback, and a saturated absorption spectrometer for Cs and Rb," American Journal of Physics **60**, 1098–1111 (1992).

[60] V. Venkataraman, K. Saha, P. Londero, and A. L. Gaeta, "Few-Photon All-Optical Modulation in a Photonic Band-Gap Fiber," Physical Review Letters **107** (2011).

[61] F. Benabid, J. C. Knight, G. Antonopoulos, and P. S. J. Russell, "Stimulated Raman Scattering in Hydrogen-Filled Hollow-Core Photonic Crystal Fiber," Science **298**, 399–402 (2002).

[62] S. Ghosh, J. E. Sharping, D. G. Ouzounov, and A. L. Gaeta, "Resonant Optical Interactions with Molecules Confined in Photonic Band-Gap Fibers," Phys. Rev. Lett. **94**, 093902 (2005).

[63] F. Benabid, P. S. Light, F. Couny, and P. S. J. Russell, "Electromagnetically-induced transparency grid in acetylene-filled hollow-core PCF," Opt. Express, OE **13**, 5694–5703 (2005).

[64] F. Couny, F. Benabid, P. J. Roberts, P. S. Light, and M. G. Raymer, "Generation and Photonic Guidance of Multi-Octave Optical-Frequency Combs," Science **318**, 1118–1121 (2007).

[65] D. G. Ouzounov, F. R. Ahmad, D. Müller, N. Venkataraman, M. T. Gallagher, M. G. Thomas, J. Silcox, K. W. Koch, and A. L. Gaeta, "Generation

of Megawatt Optical Solitons in Hollow-Core Photonic Band-Gap Fibers," Science **301**, 1702–1704 (2003).

[66] U. Vogl, C. Peuntinger, N. Y. Joly, P. S. J. Russell, C. Marquardt, and G. Leuchs, "Atomic mercury vapor inside a hollow-core photonic crystal fiber," Opt. Express, OE **22**, 29375–29381 (2014).

[67] G. Epple, K. S. Kleinbach, T. G. Euser, N. Y. Joly, T. Pfau, P. S. J. Russell, and R. Löw, "Rydberg atoms in hollow-core photonic crystal fibres," Nature Communications **5** (2014).

[68] M. Bajcsy, S. Hofferberth, V. Balic, T. Peyronel, M. Hafezi, A. S. Zibrov, V. Vuletic, and M. D. Lukin, "Efficient All-Optical Switching Using Slow Light within a Hollow Fiber," Phys. Rev. Lett. **102**, 203902 (2009).

[69] F. Blatt, T. Halfmann, and T. Peters, "One-dimensional ultracold medium of extreme optical depth," Optics Letters **39**, 446 (2014).

[70] P. Yeh and A. Yariv, "Bragg reflection waveguides," Optics Communications **19**, 427–430 (1976).

[71] X. Ji, F. A. Barbosa, S. P. Roberts, A. Dutt, J. Cardenas, Y. Okawachi, A. Bryant, A. L. Gaeta, and M. Lipson, "Breaking the Loss Limitation of On-chip High-confinement Resonators," arXiv preprint arXiv:1609.08699 (2016).

[72] L. Stern, B. Desiatov, I. Goykhman, and U. Levy, "Nanoscale light–matter interactions in atomic cladding waveguides," Nature Communications **4**, 1548 (2013).

[73] R. Ritter, N. Gruhler, W. Pernice, H. Kübler, T. Pfau, and R. Löw, "Atomic vapor spectroscopy in integrated photonic structures," Applied Physics Letters **107**, 041101 (2015).

[74] L. Stern, R. Zektzer, N. Mazurski, and U. Levy, "Enhanced light-vapor interactions and all optical switching in a chip scale micro-ring resonator coupled with atomic vapor," arXiv:1605.09008 [physics] (2016). ArXiv: 1605.09008.

[75] R. Ritter, N. Gruhler, W. H. P. Pernice, H. Kübler, T. Pfau, and R. Löw, "Coupling thermal atomic vapor to an integrated ring resonator," New J. Phys. **18**, 103031 (2016).

[76] A. Bhagwat, "Low-Light-Level Nonlinear Optics With Rubidium Atoms In Hollow-Core Photonic Band-Gap Fibers," (2010).

[77] V. Venkataraman, "Few-Photon Nonlinear Optics In Photonic Bandgap Fibers," (2012).

[78] P. Kumar, "Quantum frequency conversion," Optics letters **15**, 1476–1478 (1990).

[79] F. Vewinger, J. Appel, E. Figueroa, and A. I. Lvovsky, "Adiabatic frequency conversion of optical information in atomic vapor," Optics letters **32**, 2771–2773 (2007).

[80] A. I. Lvovsky, B. C. Sanders, and W. Tittel, "Optical quantum memory," Nature Photonics **3**, 706–714 (2009).

[81] C. H. van der Wal, M. D. Eisaman, A. André, R. L. Walsworth, D. F. Phillips, A. S. Zibrov, and M. D. Lukin, "Atomic memory for correlated photon states," Science **301**, 196–200 (2003).

[82] C. V. Raman and K. S. Krishnan, "A new type of secondary radiation," Nature **121**, 501 (1928).

[83] L. Brillouin, Ann. Phys. (Paris) **17**, 88 (1922).

[84] A. H. Gnauck, R. M. Jopson, C. J. McKinstrie, J. C. Centanni, and S. Radic, "Demonstration of low-noise frequency conversion by Bragg scattering in a fiber," Optics express **14**, 8989–8994 (2006).

[85] H. J. McGuinness, M. G. Raymer, C. J. McKinstrie, and S. Radic, "Quantum Frequency Translation of Single-Photon States in a Photonic Crystal Fiber," Physical Review Letters **105** (2010).

[86] D. MÚchin, R. Provo, J. D. Harvey, and C. J. McKinstrie, "180-nm wavelength conversion based on Bragg scattering in an optical fiber," Optics express **14**, 8995–8999 (2006).

[87] H. J. McGuinness, M. G. Raymer, C. J. McKinstrie, and S. Radic, "Wavelength Translation Across 210 nm in the Visible Using Vector Bragg Scattering in a Birefringent Photonic Crystal Fiber," IEEE Photonics Technology Letters **23**, 109–111 (2011).

[88] P. Londero, V. Venkataraman, A. R. Bhagwat, A. D. Slepkov, and A. L. Gaeta, "Ultralow-Power Four-Wave Mixing with Rb in a Hollow-Core Photonic Band-Gap Fiber," Physical Review Letters **103** (2009).

[89] V. Venkataraman, P. Londero, A. R. Bhagwat, A. D. Slepkov, and A. L. Gaeta, "All-optical modulation of four-wave mixing in an Rb-filled photonic bandgap fiber," Optics letters **35**, 2287–2289 (2010).

[90] T. Meijer, J. D. White, B. Smeets, M. Jeppesen, and R. E. Scholten, "Blue five-level frequency-upconversion system in rubidium," Opt. Lett., OL **31**, 1002–1004 (2006).

[91] F. E. Becerra, R. T. Willis, S. L. Rolston, and L. A. Orozco, "Nondegenerate four-wave mixing in rubidium vapor: The diamond configuration," Phys. Rev. A **78**, 013834 (2008).

[92] B. Srivathsan, G. K. Gulati, B. Chng, G. Maslennikov, D. Matsukevich, and C. Kurtsiefer, "Narrow Band Source of Transform-Limited Photon Pairs via Four-Wave Mixing in a Cold Atomic Ensemble," Physical Review Letters **111** (2013).

[93] M. S. Malcuit, D. J. Gauthier, and R. W. Boyd, "Suppression of amplified spontaneous emission by the four-wave mixing process," Physical review letters **55**, 1086 (1985).

[94] R. W. Boyd, M. S. Malcuit, D. J. Gauthier, and K. Rzaewski, "Competition between amplified spontaneous emission and the four-wave-mixing process," Phys. Rev. A **35**, 1648–1658 (1987).

[95] A. R. Bhagwat, A. D. Slepkov, V. Venkataraman, P. Londero, and A. L. Gaeta, "On-demand all-optical generation of controlled Rb-vapor densities in photonic-band-gap fibers," Physical Review A **79** (2009).

[96] A. D. Slepkov, A. R. Bhagwat, V. Venkataraman, P. Londero, and A. L. Gaeta, "Spectroscopy of Rb atoms in hollow-core fibers," Physical Review A **81** (2010).

[97] P. S. Donvalkar, V. Venkataraman, S. Clemmen, K. Saha, and A. L. Gaeta, "Frequency translation via four-wave mixing Bragg scattering in Rb filled photonic bandgap fibers," Optics Letters **39**, 1557 (2014).

[98] W. J. Munro, K. Nemoto, and T. P. Spiller, "Weak nonlinearities: a new

route to optical quantum computation," New Journal of Physics **7**, 137–137 (2005).

[99] A. D. Slepkov, A. R. Bhagwat, V. Venkataraman, P. Londero, and A. L. Gaeta, "Generation of large alkali vapor densities inside bare hollow-core photonic band-gap fibers," Optics express **16**, 18976–18983 (2008).

[100] P. G. Kwiat, K. Mattle, H. Weinfurter, A. Zeilinger, A. V. Sergienko, and Y. Shih, "New High-Intensity Source of Polarization-Entangled Photon Pairs," Phys. Rev. Lett. **75**, 4337–4341 (1995).

[101] D. C. Burnham and D. L. Weinberg, "Observation of Simultaneity in Parametric Production of Optical Photon Pairs," Phys. Rev. Lett. **25**, 84–87 (1970).

[102] R. Ghosh and L. Mandel, "Observation of nonclassical effects in the interference of two photons," Phys. Rev. Lett. **59**, 1903–1905 (1987).

[103] A. Christ and C. Silberhorn, "Limits on the deterministic creation of pure single-photon states using parametric down-conversion," Phys. Rev. A **85**, 023829 (2012).

[104] J. E. Sharping, J. Chen, X. Li, P. Kumar, and R. S. Windeler, "Quantum-correlated twin photons from microstructure fiber," Opt. Express, OE **12**, 3086–3094 (2004).

[105] X. Li, J. Chen, P. Voss, J. Sharping, and P. Kumar, "All-fiber photon-pair source for quantum communications: Improved generation of correlated photons," Opt. Express, OE **12**, 3737–3744 (2004).

[106] J. G. Rarity, J. Fulconis, J. Duligall, W. J. Wadsworth, and P. S. J. Russell, "Photonic crystal fiber source of correlated photon pairs," Opt. Express, OE **13**, 534–544 (2005).

[107] C. Xiong, L. G. Helt, A. C. Judge, G. D. Marshall, M. J. Steel, J. E. Sipe, and B. J. Eggleton, "Quantum-correlated photon pair generation in chalcogenide As_2S_3 waveguides," Opt. Express, OE **18**, 16206–16216 (2010).

[108] E. Engin, D. Bonneau, C. M. Natarajan, A. S. Clark, M. G. Tanner, R. H. Hadfield, S. N. Dorenbos, V. Zwiller, K. Ohira, N. Suzuki, H. Yoshida, N. Iizuka, M. Ezaki, J. L. O'Brien, and M. G. Thompson, "Photon pair

generation in a silicon micro-ring resonator with reverse bias enhancement," Opt. Express, OE **21**, 27826–27834 (2013).

[109] W. C. Jiang, X. Lu, J. Zhang, O. Painter, and Q. Lin, "Silicon-chip source of bright photon pairs," Opt. Express, OE **23**, 20884–20904 (2015).

[110] R. T. Willis, F. E. Becerra, L. A. Orozco, and S. L. Rolston, "Correlated photon pairs generated from a warm atomic ensemble," Physical Review A **82** (2010).

[111] R. T. Willis, F. E. Becerra, L. A. Orozco, and S. L. Rolston, "Photon statistics and polarization correlations at telecommunications wavelengths from a warm atomic ensemble," Opt. Express, OE **19**, 14632–14641 (2011).

[112] D.-S. Ding, Z.-Y. Zhou, B.-S. Shi, X.-B. Zou, and G.-C. Guo, "Generation of non-classical correlated photon pairs via a ladder-type atomic configuration: theory and experiment," Optics express **20**, 11433–11444 (2012).

[113] W. Zhang, D.-S. Ding, J.-S. Pan, and B.-S. Shi, "Non-Classical Correlated Photon Pairs Generation via Cascade Transition of 5 $S_{1/2}$ –5 $P_{3/2}$ –5 $D_{5/2}$ in a Hot ^{85} Rb Atomic Vapor," Chinese Physics Letters **31**, 064208 (2014).

[114] Y.-S. Lee, S. M. Lee, H. Kim, and H. S. Moon, "Superradiant Emission of Ultra-Bright Photon Pairs in Doppler-Broadened Atomic Ensemble," arXiv preprint arXiv:1603.00728 (2016).

[115] Q.-F. Chen, B.-S. Shi, M. Feng, Y.-S. Zhang, and G.-C. Guo, "Non-degenerate nonclassical photon pairs in a hot atomic ensemble," Opt. Express, OE **16**, 21708–21713 (2008).

[116] M. D. Reid and D. F. Walls, "Violations of classical inequalities in quantum optics," Physical Review A **34**, 1260 (1986).

[117] J. L. O'Brien, "Optical Quantum Computing," Science **318**, 1567–1570 (2007).

[118] Y. Okawachi, K. Saha, J. S. Levy, Y. H. Wen, M. Lipson, and A. L. Gaeta, "Octave-spanning frequency comb generation in a silicon nitride chip," Optics letters **36**, 3398–3400 (2011).

[119] P. Del'Haye, T. Herr, E. Gavartin, M. L. Gorodetsky, R. Holzwarth, and

T. J. Kippenberg, "Octave Spanning Tunable Frequency Comb from a Microresonator," Physical Review Letters **107** (2011).

[120] A. Dutt, C. Joshi, X. Ji, J. Cardenas, Y. Okawachi, K. Luke, A. L. Gaeta, and M. Lipson, "On-chip dual comb source for spectroscopy," arXiv preprint arXiv:1611.07673 (2016).

[121] A. Dutt, K. Luke, S. Manipatruni, A. L. Gaeta, P. Nussenzveig, and M. Lipson, "On-Chip Optical Squeezing," Physical Review Applied **3** (2015).

[122] A. Mohanty, M. Zhang, A. Dutt, S. Ramelow, P. Nussenzveig, and M. Lipson, "Quantum Interference between Transverse Spatial Waveguide Modes," arXiv:1601.00121 [physics, physics:quant-ph] (2016). ArXiv: 1601.00121.

[123] J. T. Robinson, K. Preston, O. Painter, and M. Lipson, "First-principle derivation of gain in high-index-contrast waveguides," Opt. Express, OE **16**, 16659–16669 (2008).

[124] W. Demtroder, "Laser spectroscopy, fourth edition," Springer **2** (2008).

[125] M. Davanço, J. R. Ong, A. B. Shehata, A. Tosi, I. Agha, S. Assefa, F. Xia, W. M. J. Green, S. Mookherjea, and K. Srinivasan, "Telecommunications-band heralded single photons from a silicon nanophotonic chip," Appl. Phys. Lett. **100**, 261104 (2012).

[126] D. J. Moss, R. Morandotti, A. L. Gaeta, and M. Lipson, "New CMOS-compatible platforms based on silicon nitride and Hydex for nonlinear optics," Nat Photon **7**, 597–607 (2013).

[127] Y. Okawachi, M. R. E. Lamont, K. Luke, D. O. Carvalho, M. Yu, M. Lipson, and A. L. Gaeta, "Bandwidth shaping of microresonator-based frequency combs via dispersion engineering," Optics Letters **39**, 3535 (2014).

[128] A. A. Savchenkov, A. B. Matsko, W. Liang, V. S. Ilchenko, D. Seidel, and L. Maleki, "Kerr combs with selectable central frequency," Nature Photonics **5**, 293–296 (2011).

[129] Y. Yang, X. Jiang, S. Kasumie, G. Zhao, L. Xu, J. M. Ward, L. Yang, and S. N. Chormaic, "Four-wave mixing parametric oscillation and frequency comb generation at visible wavelengths in a silica microbubble resonator," Optics Letters **41**, 5266 (2016).

[130] S. Miller, K. Luke, Y. Okawachi, J. Cardenas, A. L. Gaeta, and M. Lipson, "On-chip frequency comb generation at visible wavelengths via simultaneous second- and third-order optical nonlinearities," Optics Express **22**, 26517 (2014).

[131] H. Jung, R. Stoll, X. Guo, D. Fischer, and H. X. Tang, "Green, red, and IR frequency comb line generation from single IR pump in AlN microring resonator," Optica **1**, 396 (2014).

[132] L. Wang, L. Chang, N. Volet, M. H. P. Pfeiffer, M. Zervas, H. Guo, T. J. Kippenberg, and J. E. Bowers, "Frequency comb generation in the green using silicon nitride microresonators: Frequency comb generation in the green using silicon nitride microresonators," Laser & Photonics Reviews **10**, 631–638 (2016).

[133] M. Soltani, A. Matsko, and L. Maleki, "Enabling arbitrary wavelength frequency combs on chip: Enabling arbitrary wavelength frequency combs on chip," Laser & Photonics Reviews **10**, 158–162 (2016).

[134] X. Xue, Y. Xuan, P.-H. Wang, Y. Liu, D. E. Leaird, M. Qi, and A. M. Weiner, "Normal-dispersion microcombs enabled by controllable mode interactions: Normal-dispersion microcombs," Laser & Photonics Reviews **9**, L23–L28 (2015).

[135] M. E. Marhic, N. Kagi, T.-K. Chiang, and L. G. Kazovsky, "Broadband fiber optical parametric amplifiers," Opt. Lett., OL **21**, 573–575 (1996).

[136] M. R. E. Lamont, B. T. Kuhlmey, and C. M. d. Sterke, "Multi-order dispersion engineering for optimal four-wave mixing," Opt. Express, OE **16**, 7551–7563 (2008).

[137] M. E. Marhic, F. S. Yang, L. G. Kazovsky, and Y. Park, "Broadband fiber-optical parametric amplifiers and wavelength converters with low-ripple Chebyshev gain spectra," Opt. Lett., OL **21**, 1354–1356 (1996).

[138] C. J. McKinstrie, S. Radic, and A. R. Chraplyvy, "Parametric amplifiers driven by two pump waves," IEEE Journal of Selected Topics in Quantum Electronics **8**, 538–547 (2002).

[139] L.-W. Luo, N. Ophir, C. P. Chen, L. H. Gabrielli, C. B. Poitras, K. Bergmen, and M. Lipson, "WDM-compatible mode-division multiplexing on a silicon chip," Nature Communications **5** (2014).

[140] K. Luke, A. Dutt, C. B. Poitras, and M. Lipson, "Overcoming Si_3N_4 film stress limitations for high quality factor ring resonators," Opt. Express, OE **21**, 22829–22833 (2013).

[141] P. Del'Haye, O. Arcizet, M. L. Gorodetsky, R. Holzwarth, and T. J. Kippenberg, "Frequency comb assisted diode laser spectroscopy for measurement of microcavity dispersion," Nat Photon **3**, 529–533 (2009).

[142] S. Ramelow, A. Farsi, S. Clemmen, J. S. Levy, A. R. Johnson, Y. Okawachi, M. R. E. Lamont, M. Lipson, and A. L. Gaeta, "Strong polarization mode coupling in microresonators," Opt. Lett., OL **39**, 5134–5137 (2014).

[143] K. Saha, Y. Okawachi, J. S. Levy, R. K. Lau, K. Luke, M. A. Foster, M. Lipson, and A. L. Gaeta, "Broadband parametric frequency comb generation with a 1-um pump source," Optics express **20**, 26935–26941 (2012).

[144] K. Luke, Y. Okawachi, M. R. E. Lamont, A. L. Gaeta, and M. Lipson, "Broadband mid-infrared frequency comb generation in a Si_3N_4 microresonator," Optics Letters **40**, 4823 (2015).

[145] M. R. E. Lamont, Y. Okawachi, and A. L. Gaeta, "Route to stabilized ultrabroadband microresonator-based frequency combs," Optics Letters **38**, 3478 (2013).

[146] T. Herr, V. Brasch, J. D. Jost, C. Y. Wang, N. M. Kondratiev, M. L. Gorodetsky, and T. J. Kippenberg, "Temporal solitons in optical microresonators," Nature Photonics **8**, 145–152 (2013).

[147] F. Marsili, V. B. Verma, J. A. Stern, S. Harrington, A. E. Lita, T. Gerrits, I. Vayshenker, B. Baek, M. D. Shaw, R. P. Mirin, and S. W. Nam, "Detecting single infrared photons with 93% system efficiency," Nat Photon **7**, 210–214 (2013).